ADVANCEMENTS IN METROLOGY FOR CRYOGENIC AND MILLIMETER-WAVE TECHNOLOGIES

Michael B. Eller

A DISSERTATION

in

Electrical Engineering

Presented to the Faculties of the University of Virginia

in

Partial Fulfillment of the Requirements for the

Degree of Doctor of Philosophy

2022

Supervisor of Dissertation

Robert M. Weikle II, Ph.D., Professor, Electrical and Computer Engineering

Committee Chairperson

Scott Barker, Ph.D., Professor, Electrical and Computer Engineering

Dissertation Committee

William R. Deal, Ph.D., Consulting Engineer, Northrop Grumman Space Systems
George Prpich, Ph.D., Assistant Professor, Chemical Engineering
Harry Powell, Ph.D., Professor, Electrical and Computer Engineering

To my family, thanks for believing in me.

ACKNOWLEDGEMENT

First and foremost I would like to thank my advisors Bobby Weikle and Art Lichtenberger for their guidance and support. They were willing to accept this computer engineer and turn him into a microwave engineer.

I would like to thank the Northrop Grumman RFMS department in Manhattan Beach, CA for allowing me to spend a few summers in southern California and to get some extremely valuable experience. I would especially like to thank Bill Deal. Bill repeatedly demonstrated that he was truly invested in my professional development, and for that I am extremely grateful.

I must thank Tannaz Farrahi, Matt Bauwens, and Mike Cyberey for all of their help throughout my time in graduate school. Their selfless care and attention towards my personal research was absolutely critical, and I owe them infinite favors.

A special thank you to Noah Sauber and all my lab-mates for the camaraderie only fellow graduate students can understand.

Finally, thank you to the University of Virginia, where I found my professional passions, three degrees, many of my lifelong friends, and my fiancée.

ABSTRACT

ADVANCEMENTS IN METROLOGY FOR CRYOGENIC AND MILLIMETER-WAVE TECHNOLOGIES

Michael B. Eller

Robert M. Weikle II, Ph.D.

The terahertz (THz) region of the electromagnetic spectrum contains a vast amount of untapped potential for many technological applications in areas such as astronomy, imaging, non-destructive evaluation, communications, and defense; however, there is a lack of high-power sources and sensitive receivers in this region. This is commonly referred to as the "THz Gap." The design, measurement, and characterization of these circuits is often complex and labor-intensive due to the unique challenges created in this band, which sits uniquely between traditional electronics and optics.

This dissertation is a collection of four distinct measurement and metrology based research efforts: a micromachined ultrathin silicon DC probe for cryogenic measurements (1), an open-source implementation of microwave noise wave analysis (2), broadband on-wafer measurements of 35nm InP HEMT Devices and MMICs (3), and the first demonstration of WR5.1 cryogenic on-wafer scattering parameter and noise figure measurements of active devices (4).

1. For cryogenic devices, such as the SIS junction widely used in radio astronomy, even simple DC characterization is a challenging task. These chips must be lapped, thinned, and mounted to a carrier for chip-by-chip screening, an approach that is time intensive, requires additional processing of the chip before evaluation, and is not practical for screening entire wafers containing thousands of devices. A new DC cryogenic on-wafer probe capable of 4K measurements has been designed, fabricated, and demonstrated. This probe technology will enable whole-wafer cryogenic screening using a silicon-on-insulator (SOI) probe platform.

2. The study of electrical noise is a very broad and challenging field, especially at higher frequencies. The work presented in this chapter is the most robust implementation of noise

analysis in open source software to date. *scikit-rf* or *skrf* (see: https://github.com/scikit-rf/scikit-rf) is an open source microwave network analysis Python package for network creation, analysis, and calibration. *skrf* is a popular free software tool and is maintained with the collaboration of international scientists and engineers. At the time of writing, the implementation of noise wave analysis is still waiting to be merged with the main branch (see: https://github.com/mbe9a/scikit-rf).

3. One of the most important technologies enabling advancement in the terahertz region of the electromagnetic spectrum is the HEMT. The high electron mobility transistor (HEMT) has emerged in the past few decades as the dominant technology for microwave, millimeter-wave, and sub-millimeter wave low-noise circuits. HEMTs are heterojunction devices with exceptional switching speeds, high gain, and fabrication techniques compatible with monolithic processing, making them excellent devices for high frequency low-noise and power amplifiers, mixers, and oscillators. In collaboration with Northrop Grumman Space Systems, new broadband (DC-220GHz) measurements and parameter extractions of the 35nm indium-phosphide (InP) HEMT and HEMT-based monolithic microwave integrated circuit (MMIC) low noise amplifiers (LNAs) were performed.

4. The first demonstration of cryogenic on-wafer scattering parameter and noise figure measurements of active circuits were performed. A new noise figure measurement system is described and single-sideband measurements are achieved through the use of sideband cancellation.

TABLE OF CONTENTS

ACKNOWLEDGEMENT iv

ABSTRACT v

LIST OF TABLES ix

LIST OF FIGURES x

CHAPTER 1 : MICROMACHINED ULTRATHIN SILICON DC PROBE FOR CRYOGENIC MEASUREMENTS 1

1.1 Design and Fabrication 1

1.2 Thermal Interface Optimization 11

1.3 Electrical and Mechanical Characterization 16

1.4 Cryogenic Measurement 23

1.5 Conclusion and Future Work 24

CHAPTER 2 : OPEN SOURCE MICROWAVE NETWORK NOISE ANALYSIS 28

2.1 Noise Waves 28

2.2 Passive Linear Multiports 30

2.3 Noise Wave Subnetwork Growth 36

2.4 De-embedding Noisy Networks 39

2.5 Implementation in Python and *scikit-rf* 44

2.6 Linear AC Noise Voltage Simulator 54

2.7 Conclusion and Future Work 59

CHAPTER 3 : BROADBAND MEASUREMENTS OF 35NM INP HEMT DEVICES AND MMICS 61

3.1 The High Electron Mobility Transistor 61

3.2 State-of-the-Art InP Process 70

3.3 Device Measurements and Parameter Extractions 72

3.4 Design and Measurement of MMIC LNAs for Atmospheric Science 83

3.5 Conclusion 90

CHAPTER 4 : ON-WAFER WR-5.1 CRYOGENIC SCATTERING PARAMETER AND NOISE MEASUREMENTS OF ACTIVE DEVICES 96

4.1 Scattering Parameter Measurements 97

4.2 Y-Factor Noise Figure Measurements 103

LIST OF TABLES

TABLE 1.1 Material Properties of Nickel and NbTi 7
TABLE 1.2 Summary of Repeatability Measurements, Coefficient of Variation 20
TABLE 1.3 Summary of Contact Resistance Measurements 23

TABLE 3.1 Summary of Extracted Values for the NGC 35nm InP HEMT 78
TABLE 3.2 Remodeled Element Values 90

TABLE 4.1 DSB IF System 108
TABLE 4.2 SSB IF System 116

LIST OF FIGURES

FIGURE 1.1 Assembly diagram showing the probing surface of the chip and the top half of the split block. All CAD was generated using AutoDesk Inventor. 2
FIGURE 1.2 CAD detail of the full split block housing. 2
FIGURE 1.3 Annotated drawing of a two-point probe chip fabricated from 50μm silicon-on-insulator. 3
FIGURE 1.4 ANSYS Mechanical simulations comparing of 50 and 15μm SOI for different tip structures. V3 was chosen for this project for its ability to compensate for planarity issues. 4
FIGURE 1.5 ANSYS Mechanical simulations comparing of 50 and 15μm SOI for different tip structures. This plot shows each probe's maximum angular offset with respect to the wafer normal. This is the maximum angle possible with each tip at a minimum of 5mN force reaction. V2 shown above. . . 6
FIGURE 1.6 Initial fabrication steps for the DC cryogenic probe. 8
FIGURE 1.7 Drawing with the double resist plating step for nickel tips. 9
FIGURE 1.8 Drawing of the NbTi liftoff process. 9
FIGURE 1.9 Outline of the final frontside fabrication steps. Features not to scale. . . 10
FIGURE 1.10 Photograph of an assembled two-point NbTi-tipped probe with 50μm pitch. 11
FIGURE 1.11 Thermal diagram of Lakeshore CPX probe station and probe arm assembly. Images gathered from [**?**]. 11
FIGURE 1.12 Sketch of the differential thermal measurement setup. Right: Image of our measurement setup using our closed cycle cryostat. Note, because the 4K stage is not gold plated, a 75 x 50 mm, 6.35 mm thick gold-plated copper stage is permanently affixed to the center of the 4K stage to make repeatable thermal connections and is what we refer to as the '4K cold stage' in our experiments 13
FIGURE 1.13 DTR between the different sensors along the braid assemblies showing the braid itself (sensors 3 to 2) is the dominant thermal resistance source. 14

FIGURE 1.14 Experimental results for DTR of thick OFHC braid (left) and picture of commercially available, first-generation UVA, and second-generation thick braids (right). This shows the DTR from only the braid (sensor 3 to 2). 15
FIGURE 1.15 Spring constant measurement of 50μm SOI probe chip. 16
FIGURE 1.16 Repeatability (Resistance vs. Contact Cycle) for a Ni-tipped (a) and NbTi-tipped (b) probe on Al. 18
FIGURE 1.17 Contact drift (Resistance vs. Time) for a Ni-tipped and NbTi-tipped probe on Al. 19
FIGURE 1.18 Experimental setup diagram for the measurement of a single probe tip contact resistance. Probe tips are drawn as the grey boxes. A picture of the probe with silver paint shorting the tips is shown on the right. 21
FIGURE 1.19 Measured results for the contact resistance of Ni and NbTi-tipped probes on Al and Au substrates. 22
FIGURE 1.20 Experimental test setup for two UVA DC Cryoprobes in Lakeshore probe station. 23
FIGURE 1.21 QVD IV vs Temperature, measured with UVA DC Cryoprobes. 24

FIGURE 2.1 Simple noise wave schematic for a two-port network. Noise waves are considered to be perfectly launched out of their corresponding ports. . . 29
FIGURE 2.2 Graph representation of a two-port noisy network. c_s represents the noise from a 50Ω load at the input of the network. 31
FIGURE 2.4 Graph representation of a two-port noisy network with noise waves referred to the input. 34
FIGURE 2.5 The connection of two ports of the same network. The resulting s-parameters can be computed using eq. 2.14. 36
FIGURE 2.6 The interconnection of two separate networks can be transformed into an intra-connection by combining the two networks' S-parameters into a composite matrix with zeros inserted for the nonexistent port parameters. See eq. 2.15. 37
FIGURE 2.7 Common example of an embedded device. The effects of the fixture must be removed in order to get the device's S-parameters. 39

FIGURE 2.8 Graph representation of the relationships between noise waves c_1, c_2 and b_n, a_n. 41
FIGURE 2.9 A two network cascade with the network of interest positioned first in the chain. 43
FIGURE 2.10 The magnitude and phase responses of the modeled couplers. 45
FIGURE 2.11 The noise figure of the two couplers plotted against ADS results. 46
FIGURE 2.12 The noise parameters of the SAV-541+ HEMT from Mini-Circuits. The noise parameters are plotted against the noise parameters calculated by ADS. 47
FIGURE 2.13 Schematic of a balanced amplifier. Two identical RF transistors are used with two quadrature hybrids. The noise properties of the individual networks are known. 48
FIGURE 2.14 Noise parameters of a balanced amplifier computed synthetically in *skrf*. The results are plotted against ADS. This was previously not possible in *skrf*. 49
FIGURE 2.15 Noise parameters of two cascades of the SAV-541+ Mini-Circuits HEMT and a quadrature hybrid. Cascade 1 has the quadrature first and cascade 2 has the quadrature second. 51
FIGURE 2.16 Noise parameters of the original SAV network, de-embedded SAV from cascade 1, and de-embedded SAV from cascade 2. 54
FIGURE 2.17 Simulation of port voltage noise for a microstrip modeled 90 degree hybrid coupler. The noise from terminations is included. Two voltage noise sources are present at ports 1 and 2, with a correlation of $\frac{1}{\sqrt{2}}(-1+j)$. The results are compared with the equivalent simulation in Keysight ADS. 56
FIGURE 2.18 Hybrid coupler with incident noise waves c_1 and c_2 and scattered waves d_1 and d_2. The $180°$ hybrid can isolate the real part of the cross-correlation, $c_1c_2^*$. The $90°$ hybrid can isolate the imaginary part of the cross-correlation. 57
FIGURE 2.19 Plots showing the simulated noise powers at the outputs of a $90°$ and a $180°$ coupler. The input noise correlation was defined to be $\frac{1}{\sqrt{2}}(-1+j)$. The results show a normalized correlation that equals the input correlation. 58

FIGURE 2.20 Plots showing the simulated noise powers at the outputs of a $90°$ and a $180°$ coupler. The input noise correlation was defined to be $\frac{1}{\sqrt{2}}(1-j)$. The results show a normalized correlation that equals the input correlation. 59
FIGURE 3.1 Photograph of a mounted InP MMIC LNA measured with the broadband probe system. The diced MMIC is mounted onto a custom gold-finished FR4 PCB. 61
FIGURE 3.2 Band diagram and free electron concentration in one dimension. 62
FIGURE 3.3 Basic HEMT cross-section with key dimensions. 64
FIGURE 3.4 Minimal small-signal intrinsic HEMT model with extrinsic electrode elements. 64
FIGURE 3.5 Cross-sectional physical diagram with small-signal model elements added. 66
FIGURE 3.6 Pucel noise model showing uncorrelated voltage noise sources and correlated drain and gate current noise sources [23]. 70
FIGURE 3.7 NGC InP epi stackup [23]. 71
FIGURE 3.8 Example of a device embedded in 50Ω grounded CPW transmission lines. 73
FIGURE 3.9 MMIC mounting stackup for these measurements as well as the measurements in Chapter 4. 73
FIGURE 3.10 Example measured S-parameters of a two finger 80 μm periphery transistor. 74
FIGURE 3.11 Measured scattering parameters for the diced InP thru. 75
FIGURE 3.12 Comparison of the modeled CPWG structure phase with the measured difference in phase between the line and thru structures. 76
FIGURE 3.13 Comparison of the modeled CPWG structure loss with the measured difference in loss between the line and thru structures. 76
FIGURE 3.14 De-embedded maximum available gain / maximum stable gain for five different device sizes. 77
FIGURE 3.15 Modeled vs. measured for the extracted model capacitances. 78
FIGURE 3.16 Modeled vs. measured for the extracted model resistances. 79
FIGURE 3.17 Modeled vs. measured for the extracted model transition frequency, and transit time. 79
FIGURE 3.18 Modeled vs. measured for the extracted model maximum stable gain for a two finger 80μm periphery device at 0.9V, 300mA/mm. 80
FIGURE 3.19 Modeled vs. measured for the two finger 80μm periphery device at 0.9V, 300mA/mm. 80

FIGURE 3.20 Modeled and measured capacitances at higher frequency. The position in frequency of the large discontinuity is tuned by extrinsic resistances and inductances. 81
FIGURE 3.21 Modeled and measured R_{gd} at high frequency. The location of the discontinuity is dominated by the value of L_g. 82
FIGURE 3.22 Modeled and measured MAG/MSG at high frequency. 82
FIGURE 3.23 High-level schematic and layout of a 140GHz 35nm three-stage InP HEMT LNA. 84
FIGURE 3.24 Cadence layout of the 140 GHz LNA. The chip dimensions are 1.28mm x 1mm. 85
FIGURE 3.25 Schematic showing source degeneration with added source inductance. . 86
FIGURE 3.26 S-Parameter measurements vs. drain current for the 94GHz LNA design. 87
FIGURE 3.27 Comparison of simulated and measured data for 0.8V, 100mA/mm bias point. 87
FIGURE 3.28 S-Parameter measurements vs. drain current for the 118GHz LNA design. 88
FIGURE 3.29 Comparison of simulated and measured data for 0.8V, 100mA/mm bias point. 88
FIGURE 3.30 S-Parameter measurements vs. drain current for the 140GHz LNA design. 89
FIGURE 3.31 Comparison of simulated and measured data for 0.8V, 100mA/mm bias point. 89
FIGURE 3.32 Remodeled 94GHz LNA dB(S21) comparison. 90

FIGURE 4.1 Microscope picture of the NGC LNA183 MMIC LNA measured with two DMPi WR5.1 cryoprobes. 96
FIGURE 4.2 Picture of the cryogenic measurment setup. Two VDI WR5.1 mini-VNAX modules were mounted to the chamber with the custom waveguide cryo-probe assemblies. 97
FIGURE 4.3 Rendering of the WR5.1 cryoprobe waveguide arm with micro-manipulators. This was designed by both Lakeshore and Swissto12. 98
FIGURE 4.4 On-wafer measurement of the LNA183 InP MMIC in the FIR lab's Lakeshore CPX probestation. 98
FIGURE 4.5 Measured power gain of the NGC LNA183 at room temperature and about 80K. 99

FIGURE 4.6 Measured power gain of a two-finger 20μm periphery device at room temperature and 80K. 100
FIGURE 4.7 Measured power gain of a four-finger 400μm periphery device at room temperature and 80K. 101
FIGURE 4.8 Calibration standards for the room-temperature TRL calibration. 102
FIGURE 4.9 Calibration standards for the cryogenic TRL calibration. 103
FIGURE 4.10 Schematic showing the RF setup for the Y-factor noise figure measurements. 105
FIGURE 4.11 Block diagram showing the components in the full noise figure cascade. 106
FIGURE 4.12 IF chain for the double sideband noise measurements. 108
FIGURE 4.13 Picture showing the custom 3D-printed mount for the large form-factor SAX unit. The IF chain is mounted to the top of the SAX. 109
FIGURE 4.14 A measurement of passives. For a perfectly matched passive network, the loss and noise figure in dB should be equal. 110
FIGURE 4.15 Comparison of gain and noise figure for the NGC LNA183 (0.9V, 300mA/mm) at room temperature and 80K. 111
FIGURE 4.16 Room temperature gain and noise figure results for the NGC LNA183 vs. drain current. 112
FIGURE 4.17 Cryogenic gain and noise figure results for the NGC LNA183 vs. drain current. 112
FIGURE 4.18 Gain and noise figure of the four-finger 400μm device vs. temperature. . 113
FIGURE 4.19 Gain and noise figure of the four-finger 400μm at room temperature. . . 114
FIGURE 4.20 Gain and noise figure of the four-finger 400μm at 80K. 114
FIGURE 4.21 Gain and noise figure measurements for the two-finger 80μm device at room temperature vs drain current. 115
FIGURE 4.22 IF chain for the double sideband noise measurements. 115
FIGURE 4.23 Picture of the assembled SSB IF system. 116
FIGURE 4.24 Measurement procedure showing the cancellation of unwanted sidebands [9]. 117
FIGURE 4.25 Measured gain and relative noise floors of the two IF chains. The normalization factor is the ratio of the integrated power under each curve. . 118
FIGURE 4.26 The isolation between the two IF bands. This plots the measured power of IF2 frequencies injected into the IF1 system and IF1 frequencies in the IF2 system relative to the power of the injected tone. 118

FIGURE 4.27 A measurement of passive networks to verifiy the accuracy of the noise figure measurement system. 119
FIGURE 4.28 Gain and noise figure results for the NGC LNA183. 120
FIGURE 4.29 Measured gain and noise figure of the NGC LNA183 vs. drain current at 80K. 121
FIGURE 4.30 Measured gain and noise figure of the NGC LNA183 vs. drain voltage at 80K. 121
FIGURE 4.31 A comparison of the cryogenically measured gain from noise figure measurement and s-parameter measurement. 122
FIGURE 4.32 Noise figure and gain of the four-finger 400μm device at room temperature and 80K. 123
FIGURE 4.33 Measured gain and noise figure of the two-finger 80μm device at 300K. Additionally the noise equivalent temperature is plotted against the unmodified NGC noise model (right y-axis). 124
FIGURE 4.34 Noise figure of temperature-dependent model. Generated using simple temperature scaling rules and drain temperature extraction from noise figure measurements. 126

CHAPTER 1

Micromachined Ultrathin Silicon DC Probe for Cryogenic Measurements

The purpose of this work is to develop a second-generation DC cryogenic probe capable of screening on-wafer Nb-based SIS devices to mitigate the challenges of the chip-by-chip screening bottleneck. Such on-wafer screening allows for the quick verification of an entire wafer, the rejection of inferior devices, and an efficient path toward populating receiver arrays with suitable mixer chips. Previous work [1] has demonstrated a DC cryogenic probe having superior thermal conductivity to that of commercially available probes. This allows the probe to be more efficiently cooled and achieve lower cryogenic temperatures.

The work presented here is focused on maintaining the improved thermal properties of the first-generation probe [1] and adding additional capabilities through an ultrathin silicon micromachined probe technology platform. Those additional capabilities and improvements include probing much smaller and custom pad dimensions, mechanical flexibility and robustness, engineered tip metals and geometries for thermal isolation, and automation with sensing feedback [2], [3].

1.1. Design and Fabrication

1.1.1. Probe Chip and Housing

The full probe assembly, shown in Figure 1.1, consists of a gold-plated split-block housing and an integrated drop-in ultra-thin silicon chip. The silicon chip is used as the physical probing mechanism, which provides an easily re-configurable platform for durable and consistent probing of very small pad dimensions. The block design, shown in Figure 1.2, consists of a tight-tolerance channel for the probe chip, a deep channel for the biasing network, and mounting holes for a probe arm and cryogenic thermal straps. The block is milled from aluminum and plated with gold.

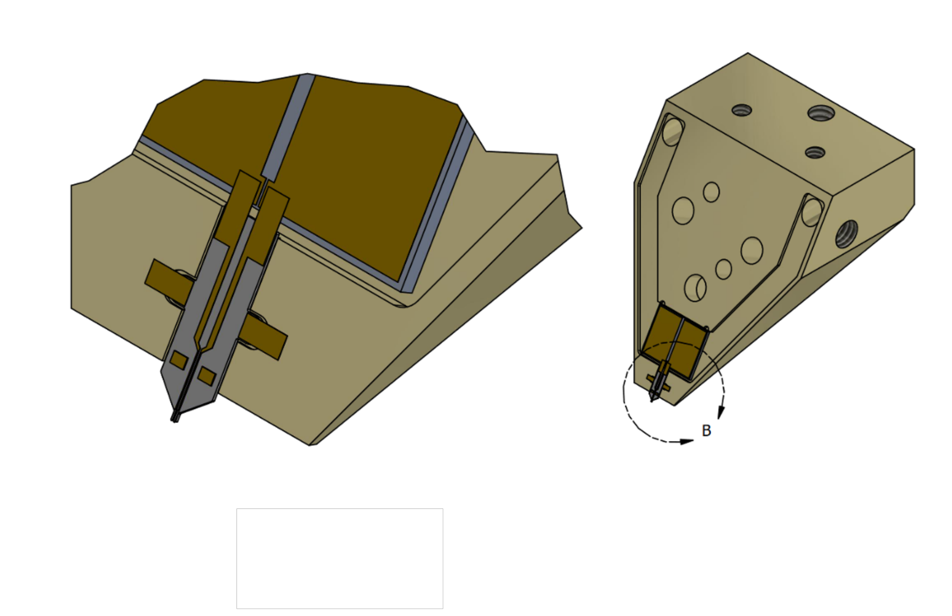

Figure 1.1: Assembly diagram showing the probing surface of the chip and the top half of the split block. All CAD was generated using AutoDesk Inventor.

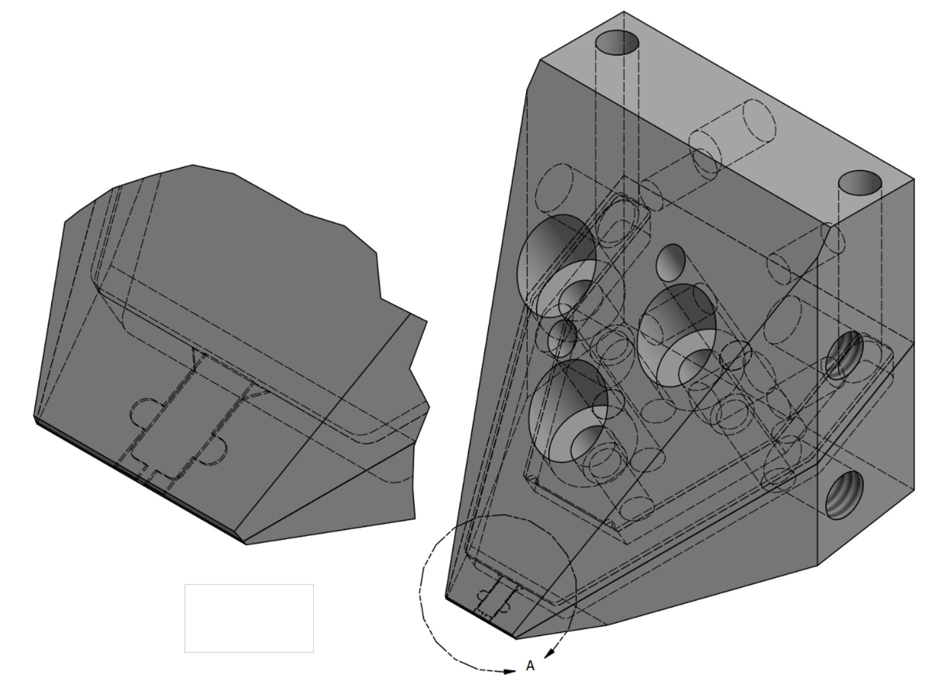

Figure 1.2: CAD detail of the full split block housing.

Aluminum is not an optimal material for cryogenic applications as its thermal conductivity at 4K is lower than that of oxygen-free high purity copper (OFHC) [4]; however, aluminum was chosen for its convenience and ease of machining. Copper is difficult to mill at the required tight tolerances (± 0.1 mil in the channel region). The gold plating provides a corrosion-proof, improved thermal connection to the heat-sinking straps [5], which also provide a chassis ground connection for the block.

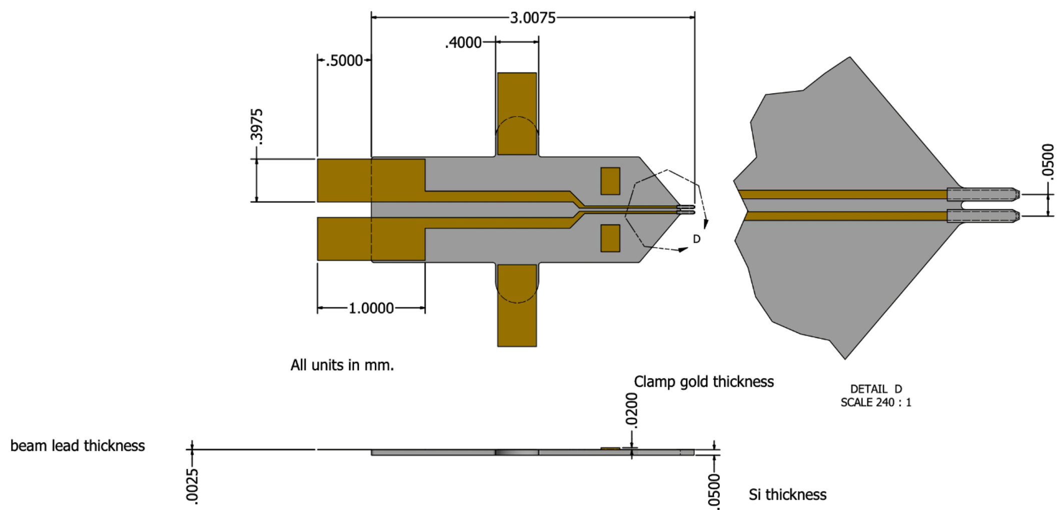

Figure 1.3: Annotated drawing of a two-point probe chip fabricated from 50μm silicon-on-insulator.

The self-aligning silicon probe chip depicted in Figures 1.1 and 1.3 sits in the housing channel (1mm wide) and is secured to the block with plated gold 'beam-leads' and thick (20μm) plated gold pads that allow the bottom housing piece to clamp the silicon firmly in place. The beam-leads are flexible plated gold structures that extend over the edge of the probe chip. The beam-leads are secured to the gold plated bias pad using an un-threaded wire bonder. A compression bond is formed with an ultrasonic pulse. The electrical connections for the probe are also made with the beam-leads. Probes with two isolated connections and four isolated connections were designed and fabricated. Figure 1.3 details a two-point probe chip. The bias pad is a small piece of quartz patterned and gold plated to 2.5μm. Cryogenic phosphor-bronze wire is then soldered to the bias chip and fed through the holes at the top of the block. Phosphor bronze wire is ideal for cryogenic applications as it has much higher thermal resistivity, thereby reducing the heat load from room temperature electrical connections. Indium solder was used since gold is soluble in tin.

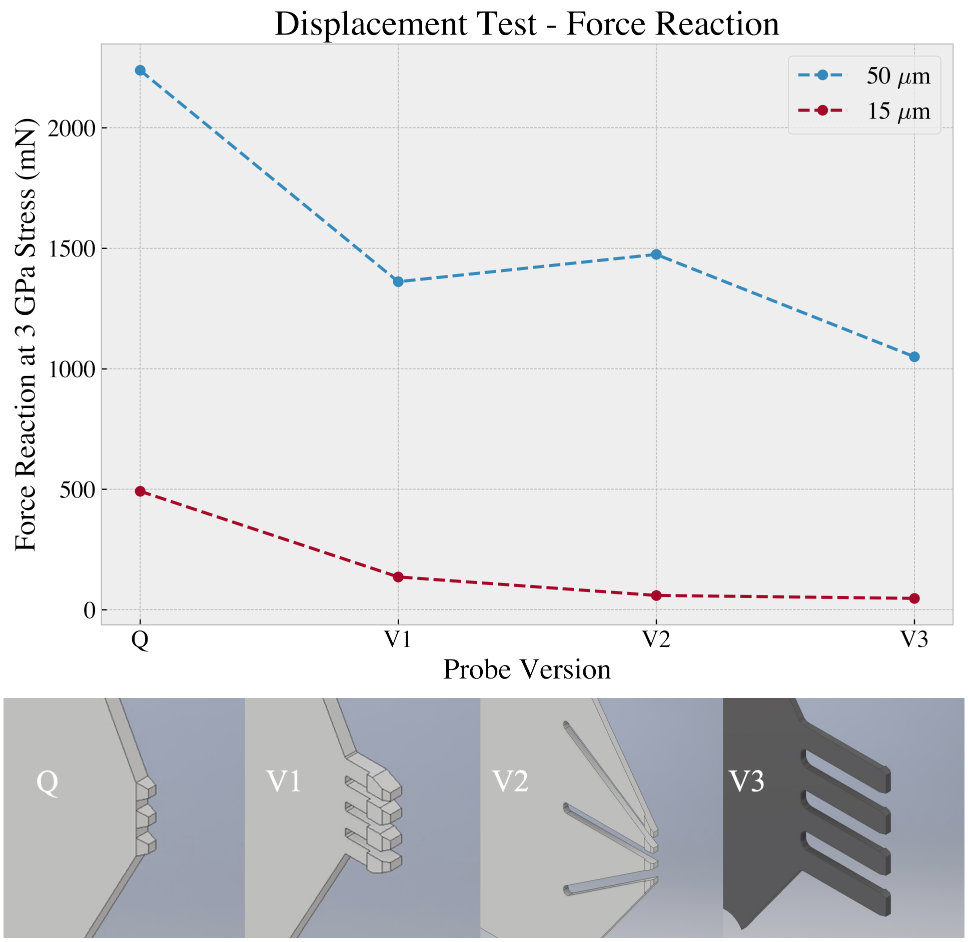

Figure 1.4: ANSYS Mechanical simulations comparing of 50 and 15μm SOI for different tip structures. V3 was chosen for this project for its ability to compensate for planarity issues.

Since this probe is intended for DC measurements, 50μm SOI was used for its improved mechanical strength as opposed to 15μm SOI demonstrated in [6; 7]. As a conservative estimate for acceptable contact resistance, the required probing force was designed and simulated in Ansys Mechanical for a minimum of 5mN [6]. From the mechanical simulations, 50μm SOI results in much higher force reaction at the substrate before reaching 3GPa of equivalent stress, which is a conservative estimate for the mechanical failure of bulk silicon. For the geometry ultimately chosen for this design (V3 in Fig. 1.4), simulation showed that the probe chip reached a contact force of over 1N before failure, while a 15μm chip of the same geometry was only able to reach a contact force of around 30mN. The tips were designed to be mechanically independent from each other and combined with the mechanical strength of 50μm SOI, the interdependent tip geometry allows the probe to compensate for large variations in wafer planarity. A two-point probe design was chosen for initial measurements to accommodate existing device pad dimensions. The overall dimensions of the chip are about 1mm width by 3mm length, making it easy to mount and replace chips without high magnification.

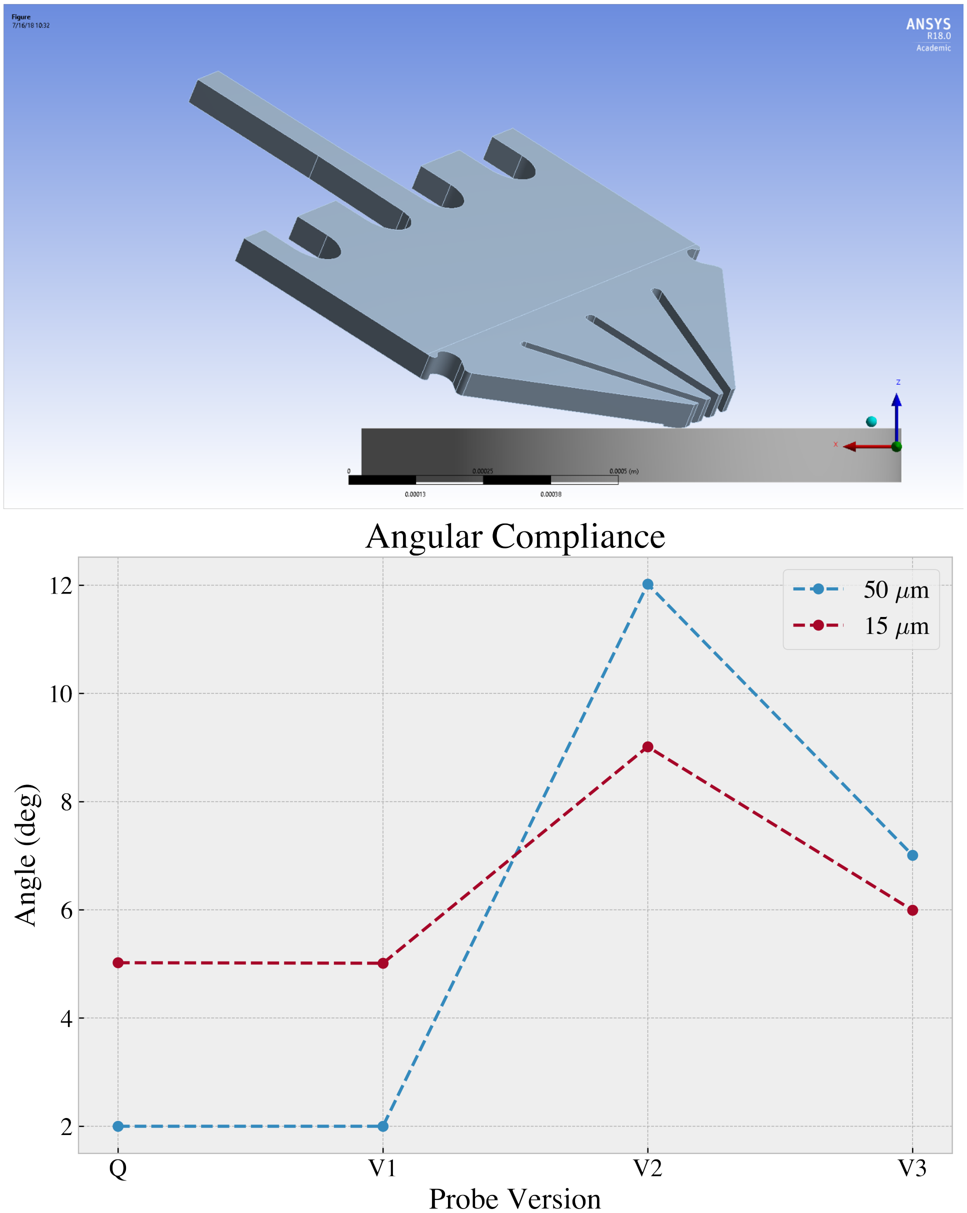

Figure 1.5: ANSYS Mechanical simulations comparing of 50 and 15μm SOI for different tip structures. This plot shows each probe's maximum angular offset with respect to the wafer normal. This is the maximum angle possible with each tip at a minimum of 5mN force reaction. V2 shown above.

1.1.2. Silicon-On-Insulator Processing and Further Considerations

The probe chip is fabricated using a silicon-on-insulator (SOI) process. SOI technology enables the fabrication of extremely thin, high-resistivity silicon device layers. Two additional variations were fabricated: one with plated nickel tips and one with sputtered niobium-titanium (NbTi) alloy tips defined by a negative resist liftoff process. NbTi was chosen as a tip material for its potential to thermally decouple the probe block (heat load) and the device-under-test (DUT). For 4 Kelvin applications, NbTi is a promising choice for tip metals as it superconducts around 9 Kelvin; therefore, if the probe tips reach temperatures well below 9K, the density of classically conducting electrons available for heat conduction will be significantly reduced. According to experimental evidence in [8; 9; 4], NbTi has a similar specific heat but much lower thermal conductivity than nickel at 4K. NbTi is also suitable for the probing of hard and oxidized surfaces such as aluminum. The hardness of 1μm thick plated nickel and sputtered NbTi films was measured using a nanoindenter. The data show that sputtered NbTi is almost three times as hard as plated nickel.

Table 1.1: Material Properties of Nickel and NbTi

	Specific Heat at 4K $\frac{mJ}{gK}$	Thermal Cond. at 4K $\frac{mW}{cmK}$	Hardness at 300K GPa (This Work)
Nickel	0.477	1700	5.8
NbTi	0.328	1.5	16.4

Another factor to consider for DC probing is the substrate leakage. The high-resistivity silicon acts as a shunt resistor to chassis ground and is typically measured to be 0.5 – 1 MΩ. At cryogenic temperatures, however, the silicon carriers “freeze-out,” meaning that the ambient temperature drop results in the density of free carriers normally existing above the Fermi level and in the conduction band recombine into the valence band and become localized. The leakage between electrical contacts is also a function of the incident light intensity on the exposed portion of the probe chip, which excites carriers on the surface of the high-resistivity silicon even at cryogenic temperatures.

1.1.3. Summary of Fabrication Steps

The fabrication process is outlined in this section. Drawings are not to scale. It follows the standard UVA IFAB Lab SOI process and has two different recipes for each tip metal: Ni and NbTi. Starting with a blank 50μm SOI wafer, the first step is to perform a Si etch [10] to define alignment vias for backside processing. This process is a dry etch that switches rapidly between etch and passivation steps for high anisotropy. Figure 1.6 outlines the initial fabrication steps. Figures 1.7 and 1.8 diagram the alternate tip metal steps.

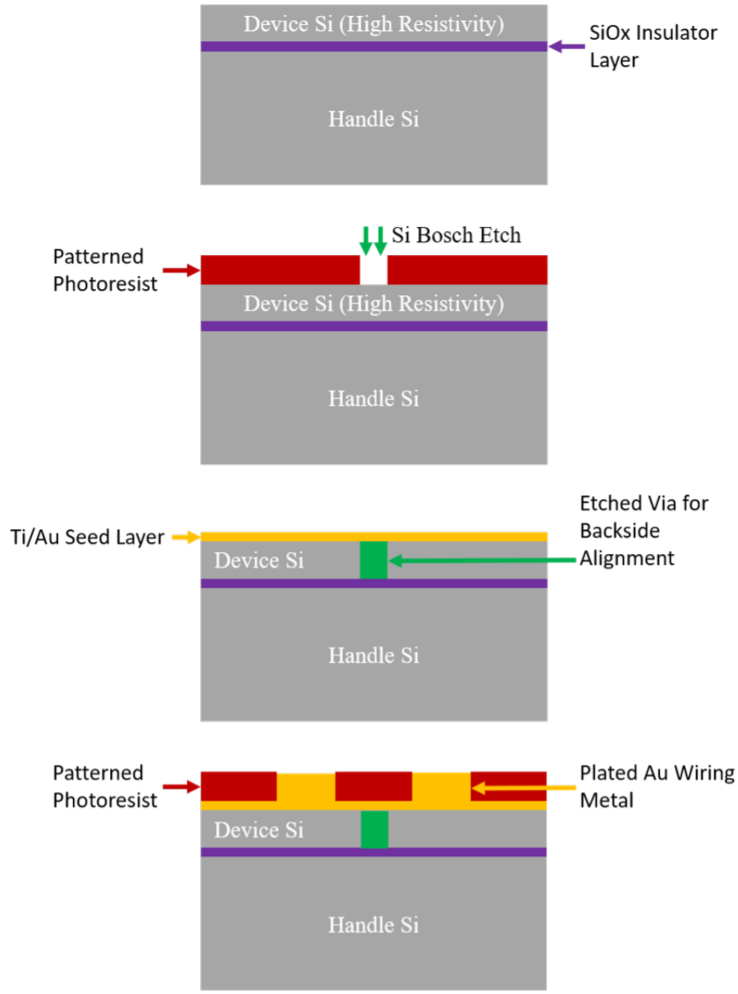

Figure 1.6: Initial fabrication steps for the DC cryogenic probe.

A titanium/gold 'seed' layer for electroplating is then deposited everywhere. The wiring metal pattern is developed and plated to 2.5μm. For the nickel-tipped probes, the wiring metal plating resist is not removed and a second resist window is formed over the tip region. The nickel is then plated on top of the exposed wiring metal. Both layers of resist are stripped after the nickel plating is completed. The nickel is plated to about 1μm. For the niobium-titanium probe tips, the initial wiring metal plating resist is stripped. Then a negative resist pattern is developed over the tips and NbTi is sputtered to 1μm. The tips are then defined by liftoff.

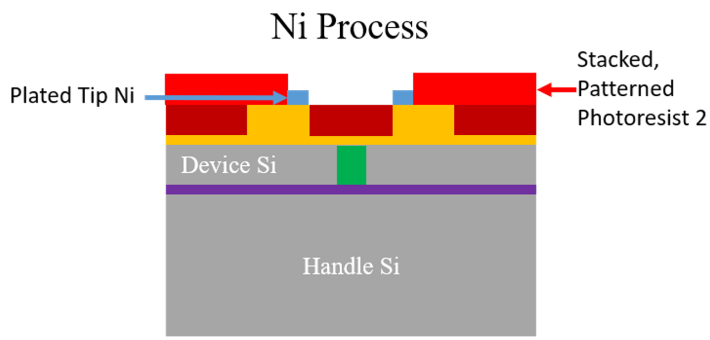

Figure 1.7: Drawing with the double resist plating step for nickel tips.

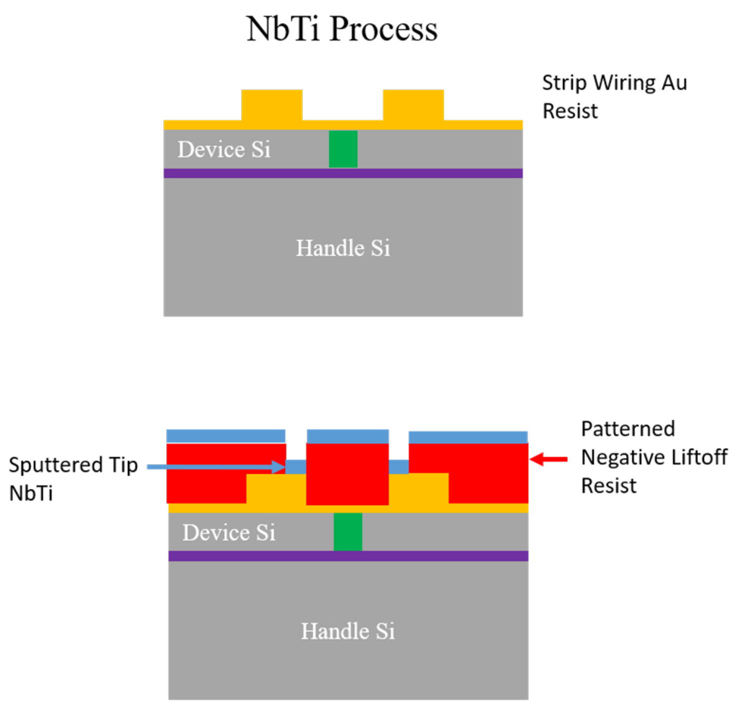

Figure 1.8: Drawing of the NbTi liftoff process.

After fabricating the tip metals, the remainder of the process is the same for all probe variants. The final frontside step is to plate the clamping gold structures and strip the seed layer. The clamp gold is the last frontside lithography step because the features are very tall (20μm +) relative to the wiring metal (2.5μm). Any lithography step after the clamp gold is plated will not achieve sufficient focus for accurate photoresist exposure. These steps are shown in Figure 1.9.

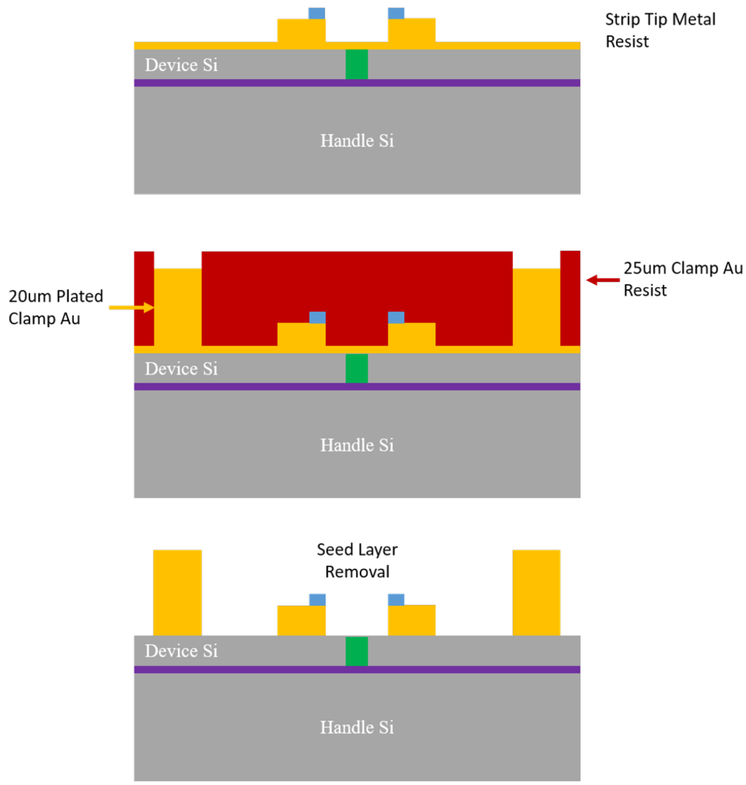

Figure 1.9: Outline of the final frontside fabrication steps. Features not to scale.

The backside process starts by spinning a thick layer of WaferBond as a protective layer for all the frontside features. The wafer is then flipped and bonded to a large carrier with EpoTek epoxy. A custom bonding apparatus [11] is used to create a very planar bond without any air bubbles. The SOI handle is then removed by a combination of a rough physical grind and a silicon reactive ion etch (RIE) etch. After the SiOx etch-stop and insulating layer is removed with a BOE wet etch, the silicon extents lithography is performed. This lithography process defines the shape of the silicon chip with the same high anisotropy silicon etch used in the via step. The final step is to develop the WaferBond and release the chips from the carrier.

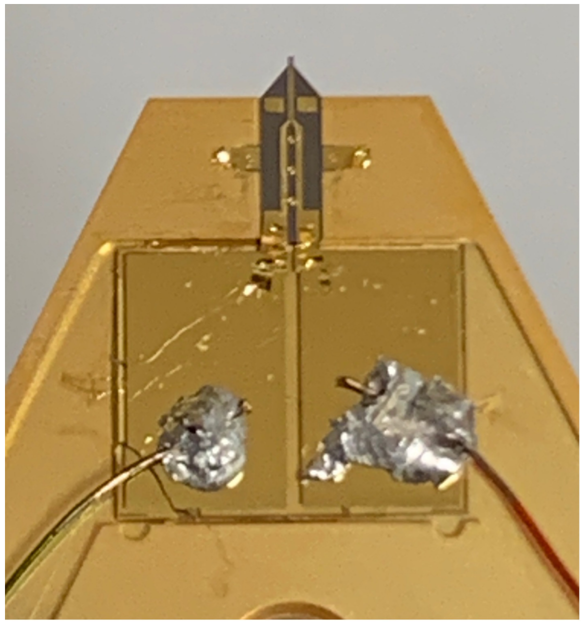

Figure 1.10: Photograph of an assembled two-point NbTi-tipped probe with 50μm pitch.

1.2. Thermal Interface Optimization

The optimization of thermal interfaces was critically important in the design of this probe. To minimize the heat load that the probe body presents to the cryogenic DUT, the heatsinking materials and configuration were specifically engineered for optimal performance at or around 4K in a CPX Lakeshore cryogenic probe station. A thermal diagram of the probe station is shown in Figure 1.11. The configuration shown is for the Lakeshore ZN50R DC probe.

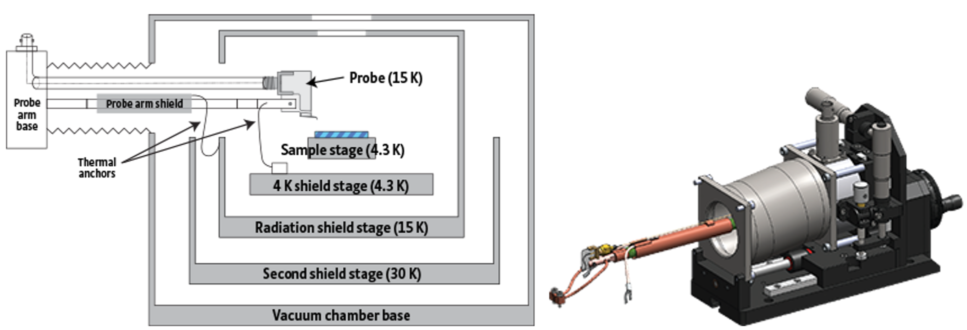

Figure 1.11: Thermal diagram of Lakeshore CPX probe station and probe arm assembly. Images gathered from [**?**].

The micro-manipulator probe arm base is separated thermally into two main sections. The main probe arm consists of a long hollow G-10 fiberglass thermally insulating tube, a transition section covered with a copper jacket and incorporates two copper braids that mount to the radiation shield stage (15K nominal). A copper end anchors to the G-10 fiberglass and provides the mounting structure for probes. The ZN50R probe has additional copper braids that mount to the 4K shield stage. Unfortunately, the minimum achievable temperature with these probes is not sufficient for IV characterization of sensitive Nb-based SIS devices [12].

1.2.1. Differential Thermal Resistance Measurements

For this design, heatsinking was performed with custom OFHC braid assemblies that affix to the probe block via the side mounting holes shown in Figure 1.2. The quantity of interest used in previous work and this work to characterize and compare the quality of different thermal interfaces was the differential thermal resistance [5; 12; 13]. The incremental thermal resistance of the heat straps (braids) and their end connections is calculated as

$$R_{P_n} = \frac{(T_2 - T_1)|_{P_n} - (T_2 - T_1)|_{P_{n-1}}}{P_n - P_{n-1}} \tag{1.1}$$

The equation above describes the incremental or differential thermal resistance. This quantity is the tangent to the temperature difference vs. power curve and is used frequently by the National Radio Astronomy Observatory in their low-temperature thermal measurements.

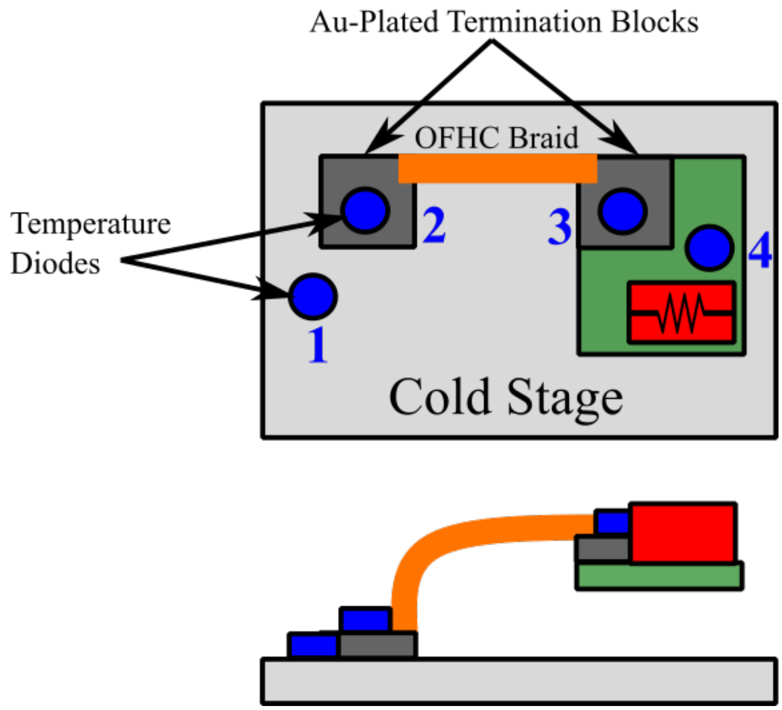

Figure 1.12: Sketch of the differential thermal measurement setup. Right: Image of our measurement setup using our closed cycle cryostat. Note, because the 4K stage is not gold plated, a 75 x 50 mm, 6.35 mm thick gold-plated copper stage is permanently affixed to the center of the 4K stage to make repeatable thermal connections and is what we refer to as the '4K cold stage' in our experiments

Figure 1.12 shows the experimental setup for the differential thermal resistance measurements. The braid assemblies were mounted into a closed-cycle cryostat. One end of the braid assembly was bolted to the cold stage, while the other end was bolted to a heater block thermally isolated from the cold stage. The differential thermal resistance was measured by incrementally increasing the power of the heater and measuring the resulting temperature change at steady state. Four points along the assembly were monitored using DT-670 temperature sensors, and the differential thermal resistance between two points was calculated with Equation 1.1 above.

While OFHC is the material of choice for heatsinking, braids are a compromise. Annealed OFHC straps have better thermal conductivity since annealing removes internal defects and stresses and therefore removes some scattering sources in the crystal lattice [4]. However, annealing makes the metal very rigid. The probes must use OFHC braids that remain flexible. The braids consisted of about 6" of either two or four braids and a custom Au-plated OFHC block at both ends. Several types of braids and termination blocks were tested. Figure 1.13 details the thermal resistance contributions from each part of the braid assembly. As expected, the braid (sensor 3 to 2) makes up much of the total thermal resistance (sensor 4 to 1). Sensor 2 to 1 represents the interface between the cold stage and the braid termination block. Sensor 4 to 3 represents the interface between the heater block and the other braid termination block. Sensor 4 to 3 and sensor 3 to 2 should was nearly identical in all cases.

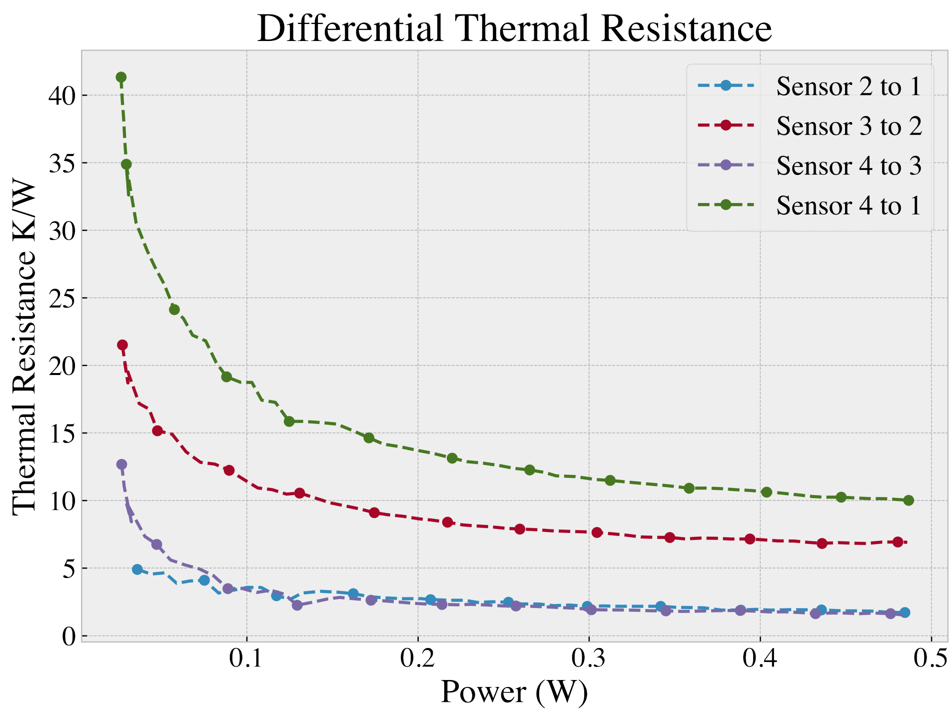

Figure 1.13: DTR between the different sensors along the braid assemblies showing the braid itself (sensors 3 to 2) is the dominant thermal resistance source.

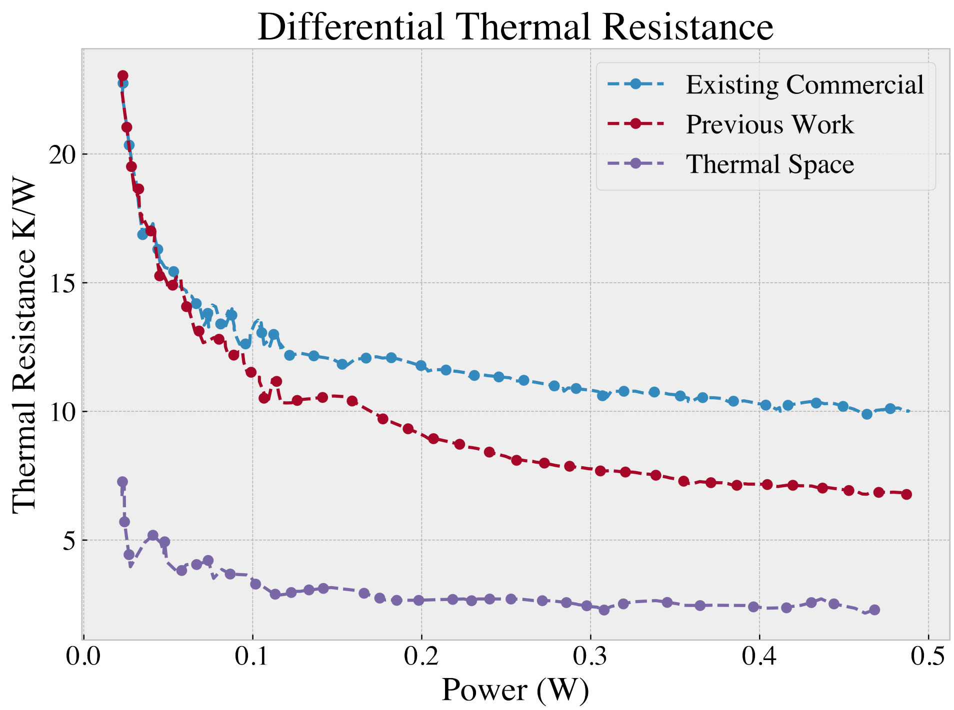

Figure 1.14: Experimental results for DTR of thick OFHC braid (left) and picture of commercially available, first-generation UVA, and second-generation thick braids (right). This shows the DTR from only the braid (sensor 3 to 2).

Figure 1.14 shows the differential thermal resistance measurements of three different braids. The first is a commercially available braid with bolted connections and no gold plating. The second is a braid from previous work on this project: four 2.5mm diameter braids soldered (silver solder) to gold plated OFHC termination blocks. The third assembly was made with compression fittings and thick (5mm diameter, fine) braided OFHC generously provided by Thermal Space. For a given resistor power, the third assembly showed significantly lower differential thermal resistance (DTR) than the other assemblies. This plot shows the DTR contribution from the braids only.

While the best overall performance (lowest DTR) is from the thick diameter soldered assemblies, the thin diameter full assemblies are comparable. The compression fit assemblies had the lowest differential thermal resistance contribution from the braids (sensors 3 to 2), which is usually the dominant source of DTR; however, the blocks were bulky and much more massive than the soldered termination blocks without providing more surface area at the thermal interface between sensors 2 to 1 and sensors 4 to 3 (block to cold stage, block to heater). As a result, the block-to-block DTR (sensor 2 to 1) for the compression fit blocks was very high compared to the other braid assemblies. There is also a noticeable difference between the gold-plated and non-plated block interfaces. The gold-plated blocks performed better for a given resistor power, which is also reported in [12].

1.3. Electrical and Mechanical Characterization

1.3.1. Mechanical Properties and Repeatability

The spring constant of the assembled probes was measured using a motion controller and a calibrated load cell. The results are shown in Figure 1.15. The spring constant was measured to be about 0.93 mN/μm. Complete failure occurred at about 400μm of total displacement, which was close to where the probe block starts to touch the plane of the DUT.

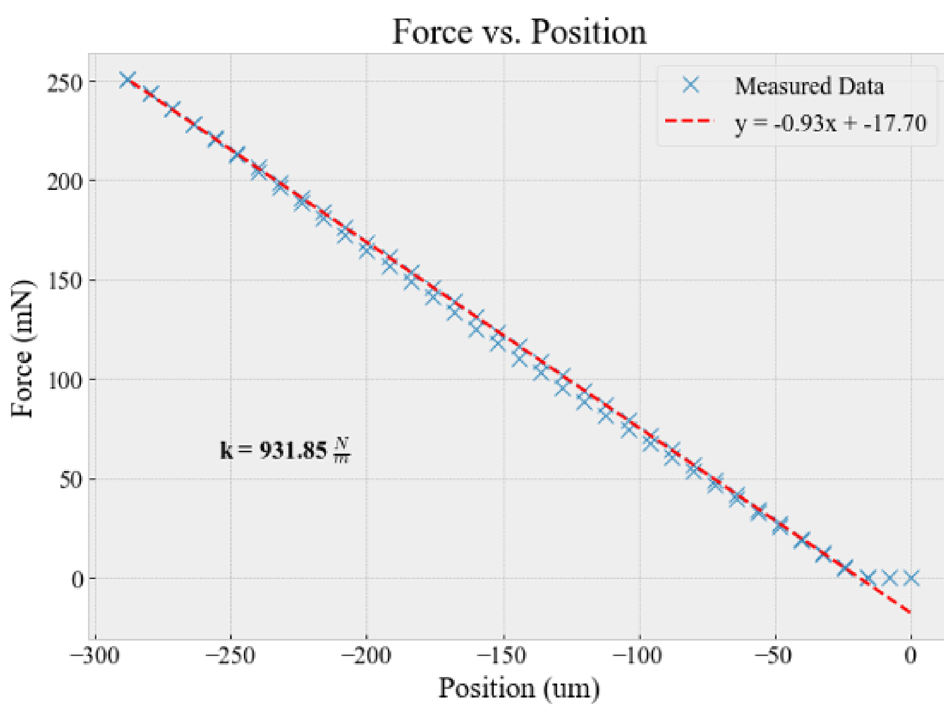

Figure 1.15: Spring constant measurement of 50μm SOI probe chip.

In addition to the spring constant, the probe contact repeatability was measured for both plated nickel and niobium-titanium tipped probes. Two different substrates were used as well: 2.5μm plated Au and 1μm plated Ni. The measurement consisted of a single two-point probe and used a digital multimeter to measure the resistance between the tips as the probe made repeated contacts on the metal substrate. Some selected results are shown in Fig. 1.16. Fig. 1.17 shows results from a similar measurement in which one contact cycle was made and held for a significant amount of time (>30 minutes). The resistance was measured periodically over this time.

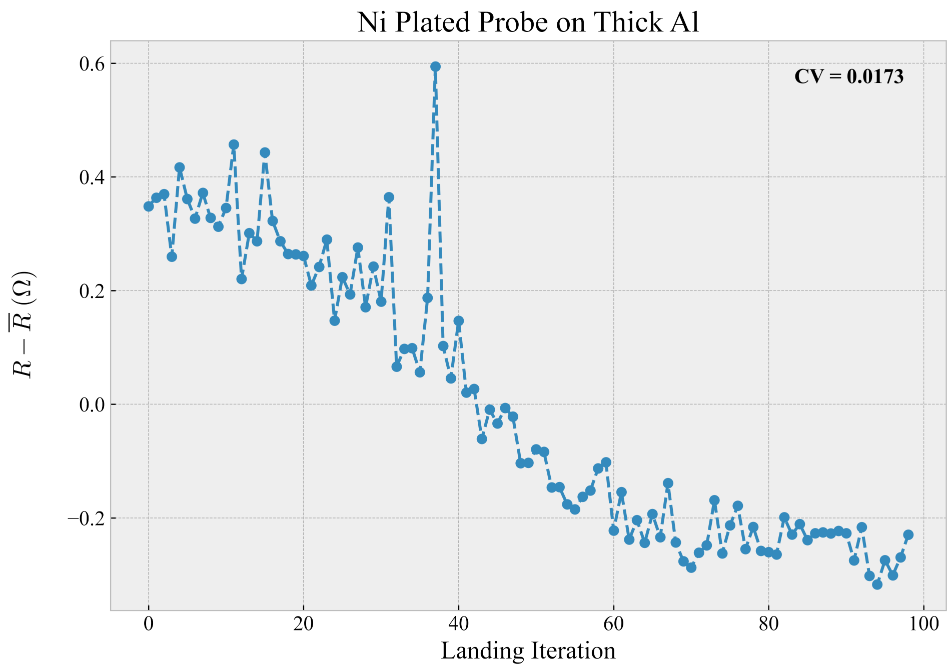

(a)

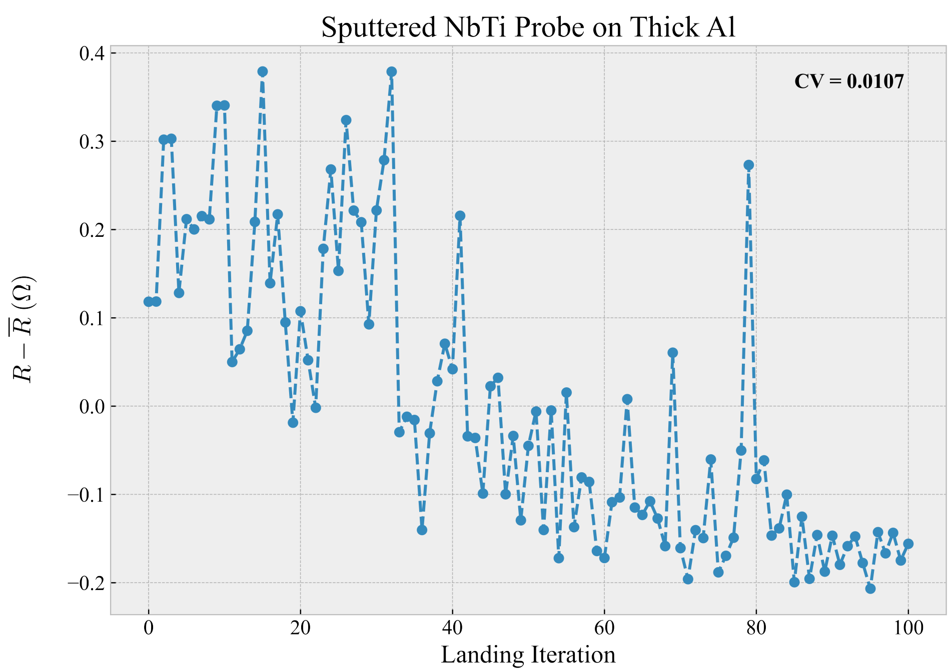

(b)

Figure 1.16: Repeatability (Resistance vs. Contact Cycle) for a Ni-tipped (a) and NbTi-tipped (b) probe on Al.

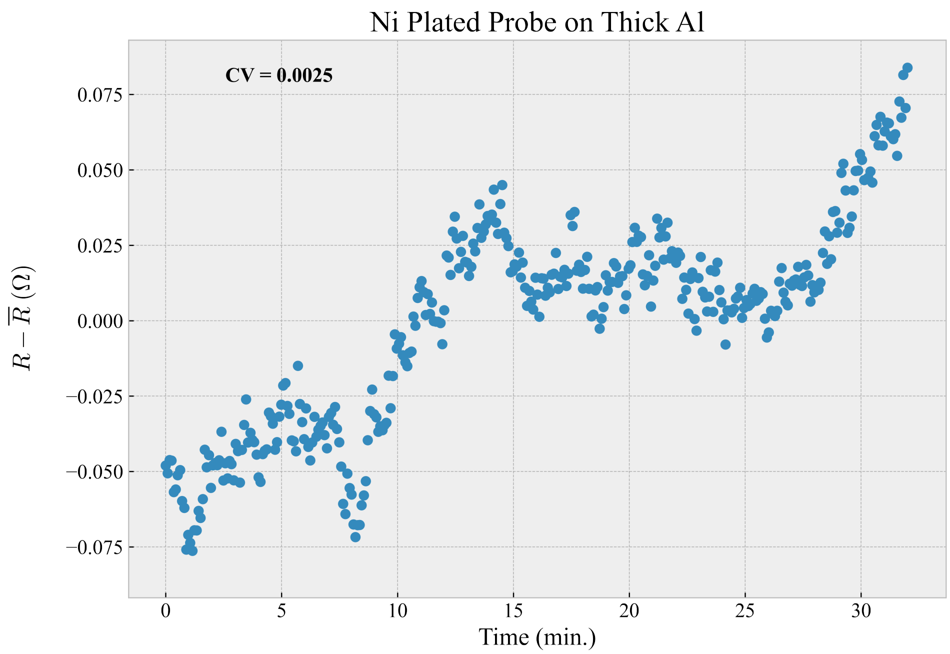

(a)

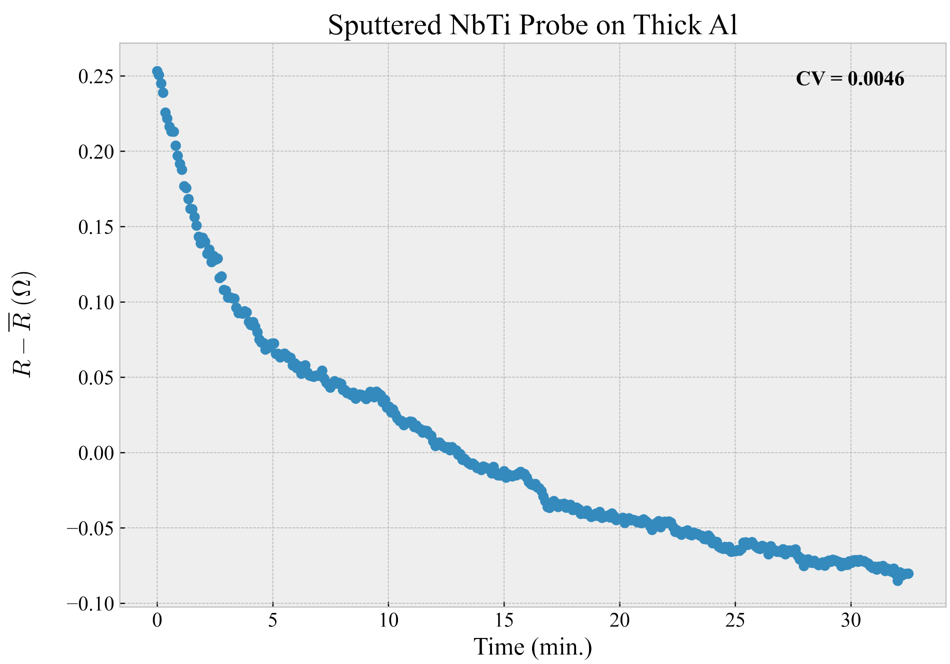

(b)

Figure 1.17: Contact drift (Resistance vs. Time) for a Ni-tipped and NbTi-tipped probe on Al.

The absolute resistance from the data above is not significant. Each probe block has a different length of cryogenic phosphor-bronze wire that contributes most of the resistance seen. For that reason, the metric used to compare results between probes is the coefficient of variation (CV), which is the standard deviation divided by the mean. A table of all the results for these measurements is included below. The table includes results from both Ni and NbTi probes on 'thin' and 'thick' substrates. The thin gold is a sputtered film much less than 1μm, and the thin aluminum is a few hundred nm thick. The thick gold is at least 2.5μm, and the thick aluminum is about 1μm thick.

Table 1.2: Summary of Repeatability Measurements, Coefficient of Variation

Substrate	Ni (R v. Contact)	NbTi	Ni (R v. Time)	NbTi
Thin Au	0.0183	0.0527	0.0592	0.0211
Thick Au	0.0015	0.0045	0.0152	0.0036
Thin Al	0.0243	0.0124	0.0569	0.0043
Thick Al	0.0173	0.0107	0.0025	0.0046

Based on the coefficient of variation, NbTi-tipped probes of this configuration were superior to the Ni tipped probes when contacting aluminum in every test except in the R vs Time measurement on thick aluminum; however, those results were quite close. Another interesting result was the comparison of Ni and NbTi repeatability on thin gold. NbTi CV was over twice the Ni CV. This suggested that NbTi was more aggressive most likely due to the hardness of NbTi.

1.3.2. Contact Resistance

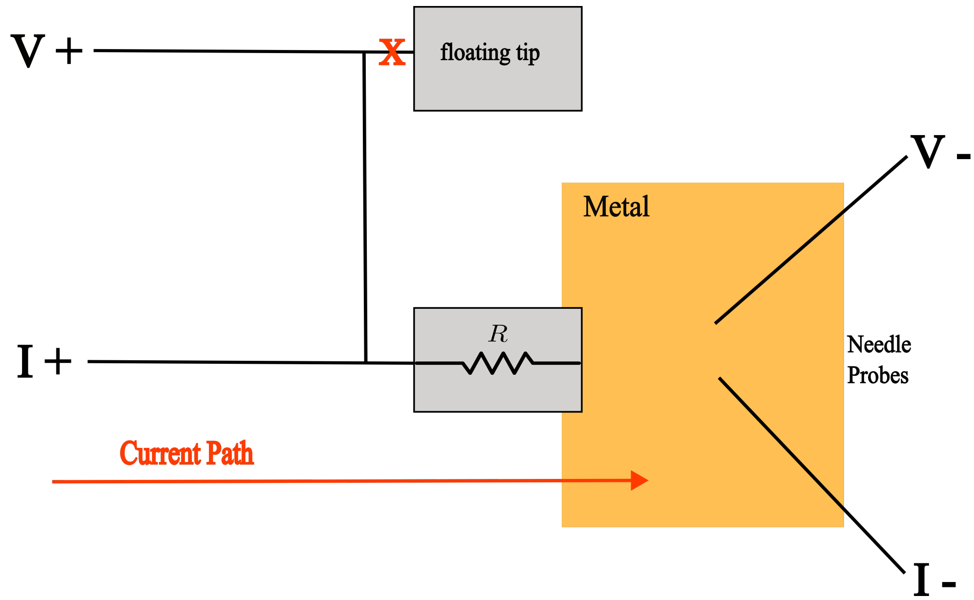

Figure 1.18: Experimental setup diagram for the measurement of a single probe tip contact resistance. Probe tips are drawn as the grey boxes. A picture of the probe with silver paint shorting the tips is shown on the right.

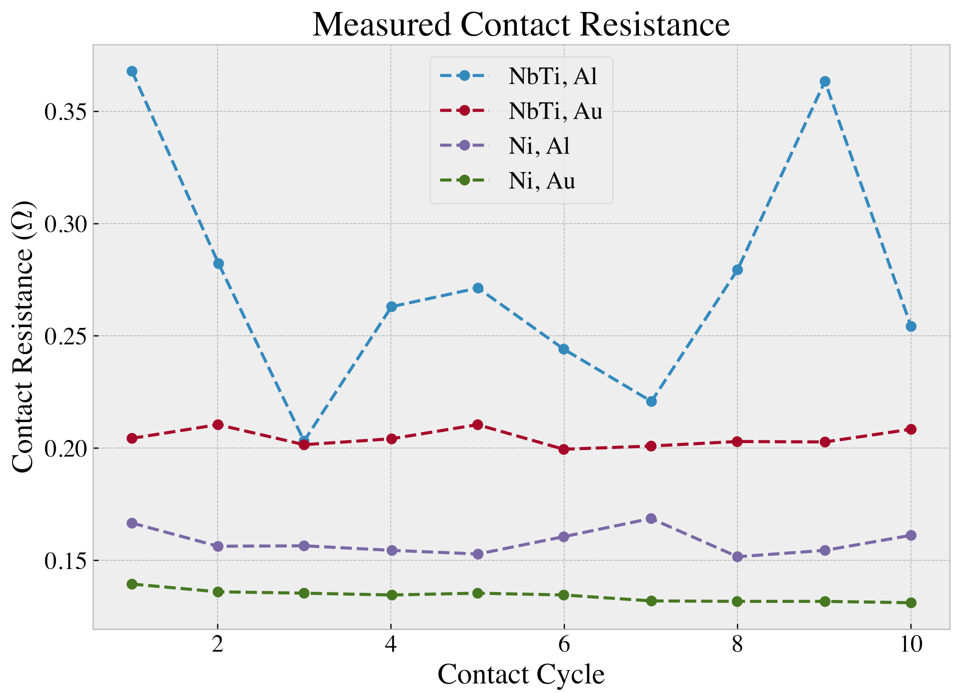

Figure 1.19: Measured results for the contact resistance of Ni and NbTi-tipped probes on Al and Au substrates.

The contact resistance was also measured for Ni and NbTi probes on gold and aluminum substrates. A diagram of the experimental setup is shown in Figure 1.18. Silver paint was used to short a single probe chip at the base of the tips. While only landing one probe tip (leaving the other tip floating), a four-point measurement was performed using two additional needle probes. In this way, the resistance measured included only a short length of wiring metal, the gold to nickel or gold to NbTi interface at the tip, and the contact resistance. The contact resistance was the dominant component of the measured resistance.

The measured results are shown in Figure 1.19 and Table 1.3. The nickel probes had lower contact resistance than the NbTi probes in both cases. The bulk resistivity of NbTi is about ten times that of nickel at about 0.734 $\mu\Omega \times m$ [14]. Additionally, NbTi can oxidize in O2 plasma, which was routinely used in the fabrication of these probes. Both of those were contributing factors to the overall increase in contact resistance. The main outlier in this measurement was obviously the NbTi on aluminum contact resistance. While, the average followed the trend of increasing contact resistance, the standard deviation was an order of magnitude larger than the other three measurements.

Table 1.3: Summary of Contact Resistance Measurements

Probe, Sub.	Mean (Ω)	St. Dev. (Ω)	CV
Ni, Au	0.134	0.0024	0.018
Ni, Al	0.158	0.0055	0.035
NbTi, Au	0.204	0.0038	0.019
NbTi, Al	0.246	0.051	0.186

1.4. Cryogenic Measurement

Figure 1.20 shows two full probe assemblies loaded into the Lakeshore CPX probe station. The blocks were attached to the standard probe arms using a custom 3D-printed PETG mount. The mount was printed with 100% infill to prevent outgassing.

Figure 1.20: Experimental test setup for two UVA DC Cryoprobes in Lakeshore probe station.

With a steady-state block temperature below 6K, these probes offer a tool for extremely low temperature on-wafer DC measurements. A demonstration of cryogenic DC probing was successfully performed by measuring the IV curve of a GaAs Quasi-vertical Schottky diode (QVD) vs. temperature. The diode technology is heterogeneously integrated GaAs onto a high-resistivity silicon substrate; therefore, the substrate acts as a very large resistor in parallel with the diode. This resistance creates a leakage current that can be measured in the IV curve of the diode before forward conduction is achieved. The results are shown below in Figure 1.21.

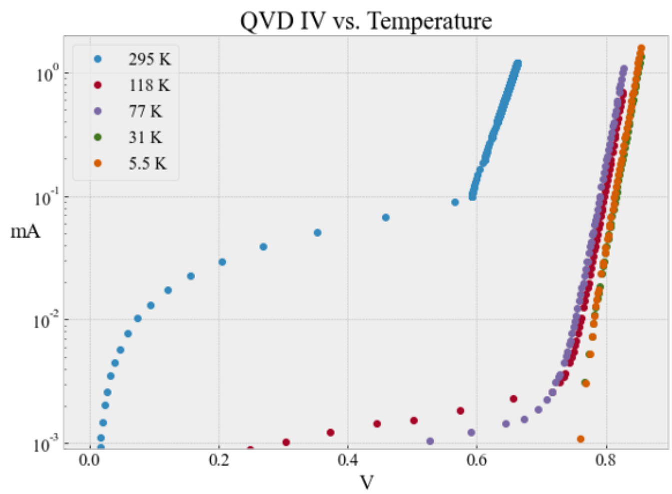

Figure 1.21: QVD IV vs Temperature, measured with UVA DC Cryoprobes.

As the substrate temperature was decreased and the probability of finding an electron in the conduction band decreased, the measured leakage current decreased as well. Eventually the silicon "freeze-out" occurred, and no leakage current was measured. The diode was mounted on a small piece of quartz with plated gold at least 2.5μm thick.

1.5. Conclusion and Future Work

Cryogenic probing has been successfully demonstrated with this second-generation cryogenic DC probe. The mechanical and repeatability properties were also characterized. NbTi was introduced as a potential new tip material for both cryogenic probing and aluminum probing for its theoretical superior thermal isolation at low temperatures and potential for alternative fabrication techniques. NbTi was shown to be superior in repeatability for probing aluminum; however, the contact resistance of NbTi was measured to be greater than that of Ni. The 50μm SOI provided greater mechanical strength and the ability to generate large contact force suitable for probing hard or oxidized surfaces. Future work will focus on measurement and DC screening of UVA's next generation of Nb-based superconductor-insulator-superconductor devices.

Bibliography

[1] Michael Cyberey and Arthur Lichtenberger, "Advanced Materials and On-wafer Chip Evaluation: 2nd Generation ALMA Superconducting Mixers," University of Virginia, NRAO, Charlottesville, VA, Study Closeout Report, Mar. 2017.

[2] Q. Yu, M. Bauwens, C. Zhang, A. W. Lichtenberger, R. M. Weikle, and N. S. Barker, "Integrated strain sensor for micromachined terahertz on-wafer probe," in 2013 IEEE MTT-S International Microwave Symposium Digest (MTT), Jun. 2013, pp. 1–4. doi: 10.1109/MWSYM.2013.6697634.

[3] Q. Yu, M. F. Bauwens, C. Zhang, A. W. Lichtenberger, R. M. Weikle, and N. S. Barker, "Improved Micromachined Terahertz On-Wafer Probe Using Integrated Strain Sensor," IEEE Trans. Microw. Theory Tech., vol. 61, no. 12, pp. 4613–4620, Dec. 2013, doi: 10.1109/TMTT.2013.2288602.

[4] F. R. Schwartzberg, "Thermal Conductivity of Some Solids," in Cryogenic Materials Data Handbook, 1970. [Online]. Available: https://www.bnl.gov/magnets/staff/gupta/cryogenic-data-handbook/section7.pdf

[5] A. R. Kerr and N. Horner, "THE LOW TEMPERATURE THERMAL RESISTANCE OF HIGH PURITY COPPER AND BOLTED COPPER JOINTS," p. 10.

[6] T. J. Reck et al., "Micromachined Probes for Submillimeter-Wave On-Wafer Measurements—Part I: Mechanical Design and Characterization," IEEE Transactions on Terahertz Science and Technology, vol. 1, no. 2, Art. no. 2, Nov. 2011, doi: 10.1109/TTHZ.2011.2165013.

[7] L. Chen et al., "Terahertz micromachined on-wafer probes: Repeatability and robustness," in 2011 IEEE MTT-S International Microwave Symposium, Jun. 2011, pp. 1–4. doi: 10.1109/MWSYM.2011.5972907.

[8] L. V. Potanina et al., "NB3SN AND NbTi MULTIFILAMENTARY WIRES WITH EN-

HANCED HEAT CAPACITY," AIP Conference Proceedings, vol. 986, no. 1, pp. 349–356, Mar. 2008, doi: 10.1063/1.2900366.

[9] I. P. Gregory and D. E. Moody, "The low temperature specific heat and magnetization of binary alloys of nickel with titanium, vanadium, chromium and manganese," Journal of Physics F: Metal Physics, vol. 5, no. 1, pp. 36–44, Jan. 1975, doi: 10.1088/0305-4608/5/1/008.

[10] F. Laermer and A. Schilp, "METHOD OF ANISOTROPICALLY ETCHING SILICON," 5501893

[11] T. W. Cecil, "New fabrication techniques for aluminum nitride-based superconductor tunnel junctions," Ph.D., University of Virginia, Ann Arbor, 2008.

[12] Michael Cyberey and Arthur Lichtenberger, "Advanced Materials and On-wafer Chip Evaluation: 2nd Generation ALMA Superconducting Mixers," University of Virginia, NRAO, Charlottesville, VA, Study Closeout Report, Mar. 2017.

[13] A. R. Kerr and R. Groves, "Measurements of Copper Heat Straps Near 4 K With and Without Apiezon-N Grease," p. 8.

[14] D. Z. Pavičić and K. D. Maglić, "Specific Heat and Electrical Resistivity of 53%Niobium-47%Titanium Alloy Measured by Subsecond Calorimetric Technique," International Journal of Thermophysics, vol. 23, no. 5, Art. no. 5, Sep. 2002, doi: 10.1023/A:1019812925066.

CHAPTER 2

Open Source Microwave Network Noise Analysis

The ultimate sensitivity of microwave circuits is often limited by the electrical noise generated from within the circuits themselves. There are many different sources of electrical noise, but the most prevalent is Johnson-Nyquist noise, or thermal noise. Thermal noise is generally independent of frequency and is an unavoidable consequence of free charge carriers interacting with the thermally-excited crystalline lattice of the conducting material. The study of electrical noise is a very broad and challenging field, especially at higher frequencies.

2.1. Noise Waves

There are a lot of different ways to think about electrical noise. Noise represented in terms of voltages and currents (with corresponding impedance and admittance network parameters) is fairly common; however, for the same reasons that microwave circuits are often represented in terms of waves (scattering parameters), thinking of noise in terms of waves is also advantageous.

The wave framework for noise is amenable to signal flow graph theory and computer aided design. They are easily represented alongside scattering parameters. Additionally, wave parameters are easier to measure at higher frequency as broadband opens and shorts (required for measuring impedance and admittance parameters) are much harder to realize than a broadband 50Ω load, which wave parameters require.

The work presented in this chapter is the most robust implementation of noise analysis in open source software to date. *scikit-rf* or *skrf* (see: https://github.com/scikit-rf/scikit-rf) is an open source microwave network analysis Python package [1] for network creation, analysis, and calibration. *skrf* is a popular free software tool and is maintained with the collaboration of international scientists and engineers. There did exist a form of noise analysis before this work; however, the implementation was flawed and incomplete. Arbitrary connections of noisy networks did not work. At the time of writing, this implementation of noise wave analysis is still waiting to be merged with the main branch (see: https://github.com/mbe9a/scikit-rf).

2.1.1. Noise Wave Definition

The noise waves for a linear multiport network are defined as outwardly directed waves that are perfectly launched out of each port. A two-port example is shown in Figure 2.1.

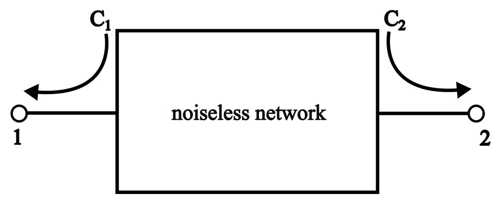

Figure 2.1: Simple noise wave schematic for a two-port network. Noise waves are considered to be perfectly launched out of their corresponding ports.

Noise waves c_1 and c_2 are perfectly launched from the noiseless network. The linear combination of incident, reflected, and noise waves is given in Equation 2.1.

$$\begin{pmatrix} b_1 \\ b_2 \end{pmatrix} = \begin{pmatrix} S_{11} & S_{12} \\ S_{21} & S_{22} \end{pmatrix} \begin{pmatrix} a_1 \\ a_2 \end{pmatrix} + \begin{pmatrix} c_1 \\ c_2 \end{pmatrix} \tag{2.1}$$

Noise waves c_1 and c_2 are analogous to the incident and scattered waves, a_i and b_i, and the wave amplitudes are still of units $\frac{V}{\sqrt{\Omega}}$; however, electrical noise is fundamentally a non-deterministic physical phenomenon. As a result, the only meaningful quantities regarding noise waves are the statistical averages of their powers. This information is represented in the noise wave correlation matrix,

$$\mathbf{C}_s = \overline{\mathbf{c}\mathbf{c}^\dagger} \tag{2.2}$$

where † denotes the hermitian transpose and the overline denotes a correlation product. The diagonal elements of the noise wave correlation matrix give the statistical expectation of the noise power from each port, while the off-diagonal terms give the cross-correlation of the the noise waves. For any N-port network, its noise wave correlation matrix will have dimensions N×N. A two-port example is given in eq. 2.3.

$$\mathbf{C}_s = \begin{pmatrix} \overline{|c_1|^2} & \overline{c_1 c_2^*} \\ \overline{c_2 c_1^*} & \overline{|c_2|^2} \end{pmatrix} \tag{2.3}$$

2.2. Passive Linear Multiports

S.W. Wedge in his 1991 paper [2] explains that for a passive linear multiport in thermodynamic equilibrium, the noise wave correlation matrix of the network is completely defined by the scattering parameters of the network, which is also known as Bosma's Theorem [3].

$$\mathbf{C}_s = k_B T(\mathbf{I} - \mathbf{S}\mathbf{S}^\dagger) \tag{2.4}$$

Again, for a passive network the noise properties are known if the scattering parameters are known. This phenomenon arises from the physical requirement that for thermodynamic equilibrium to hold, the noise power that a theoretical load supplies *to* some arbitrary network must also dissipate an equal amount of noise power *from* the network. Expression 2.4 is a powerful tool for calculating the noise wave correlation matrix of an arbitrary N-port passive network. This additionally means that the noise properties of any arbitrary connected or cascaded passive networks are known without any additional calculations apart from computing the resulting network's scattering parameters.

2.2.1. Noise Factor

Generally, the noise factor of any network with reflectionless ports at port i is given by Equation 2.5.

$$NF_i = 1 + \frac{\mathbf{C}_{sii}}{k_B T \sum_{j \neq i} |S_{ij}|^2} \tag{2.5}$$

This can easily be derived using signal flow graph theory. Figure 2.2 represents a noisy two-port network with noise waves c_1 and c_2 directly connected to the scattered wave nodes of each port, b_i.

c_s is the noise from a 50Ω load at the input of the network; therefore, it is directly connected to the incident wave node at port 1, a_1.

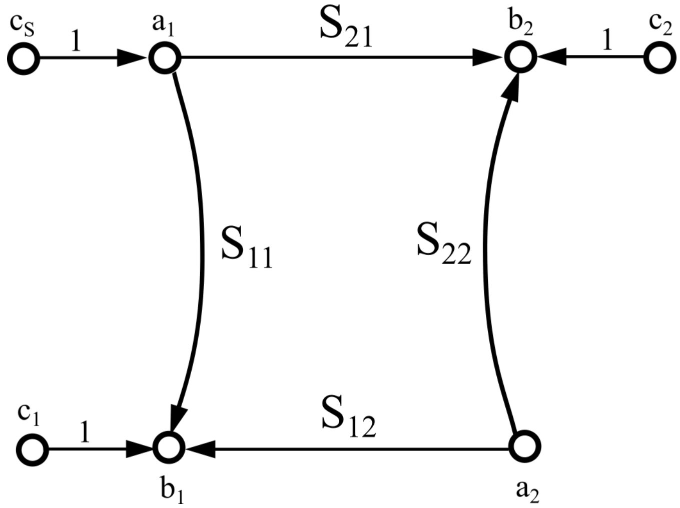

Figure 2.2: Graph representation of a two-port noisy network. c_s represents the noise from a 50Ω load at the input of the network.

The noise factor of a network is a figure-of-merit characterizing the degradation of signal-to-noise ratio from the input of the network to the output of the network. Noise factor is defined by Equation 2.6. The definition of noise factor requires that there be a noisy 50Ω load at the inputs of the network and a noiseless 50Ω load at the output.

$$NF = 1 + \frac{N_A}{N_s G_a} \tag{2.6}$$

N_A above is the noise added by the network. N_s represents the input noise, and G_a is the available gain of the network. From Figure 2.2, the noise power at the output of the network, $\overline{|b_2|^2}$, is

$$\overline{|b_2|^2} = (c_2 + S_{21}c_s)(c_2 + S_{21}c_s)^*$$

$$\overline{|b_2|^2} = \overline{|c_2|^2} + \overline{|c_s|^2}|S_{21}|^2$$

As the noise into the network is uncorrelated to the noise from the network, the cross-correlation terms average to zero. It is clear from the expressions above, that the added noise at the output of this network, N_A, is simply $\overline{|c_2|^2}$. The input noise (input-referred) is clearly $\overline{|c_s|^2}$, and as there are no loops the path power gain from a_1 to b_2 is $|S_{21}|^2$.

$$NF_2 = 1 + \frac{N_A}{N_s G_a} = 1 + \frac{\overline{|c_2|^2}}{\overline{|c_s|^2}|S_{21}|^2} = 1 + \frac{\overline{|c_2|^2}}{k_B T |S_{21}|^2} \tag{2.7}$$

While noting that the maximum noise power in a 1-Hz bandwidth from a matched load at temperature T is $k_B T$, it is clear that Equation 2.7 arrives at the same result as Equation 2.5. The derivation is easily extended to multiport networks by accounting for the incident noise at every port other than the defined output port. It is therefore very easy to calculate the noise factor or noise figure (noise factor in dB) for any port of a given multiport network if the noise wave correlation matrix is known.

Equation 2.5 can be further simplified for a passive linear network in thermodynamic equilibrium by substituting Equation 2.4 into 2.5.

$$NF_i = 1 + \frac{1 - |S_{ii}|^2}{\sum_{j \neq i} |S_{ij}|^2} \tag{2.8}$$

Equation 2.8 is a very convenient expression for calculating the noise figures of any passive multiport network. If the scattering parameters are known, the noise wave correlation matrix known but also the noise figure at any port.

2.2.2. Two-Port Noise Parameters

In the case of a two-port amplifier, the source reflection coefficient for optimal 50Ω small-signal match is most certainly not equal to the reflection coefficient required for minimum noise figure, NF_{min}. Figures 2.3a and 2.3b depict a two-port noisy network with source reflection coefficient, Γ_s. The noise factor of this network is given below.

$$NF = NF_{min} + \frac{4R_n|\Gamma_s - \Gamma_{opt}|^2}{Z_0|1+\Gamma_{opt}|^2(1-|\Gamma_s|^2)} \tag{2.9}$$

From Equation 2.9, the noise factor of a two-port network with source reflection coefficient, Γ_s, is a function of the four noise parameters: the minimum noise factor, NF_{min}, the real and imaginary parts of Γ_{opt}, and the equivalent noise resistance, R_n. Direct analytical expressions exist to calculate a network's noise parameters from its scattering parameters and its noise wave correlation matrix. The network's noise wave correlation matrix can similarly be calculated given the network's s-parameters and conventional noise parameters.

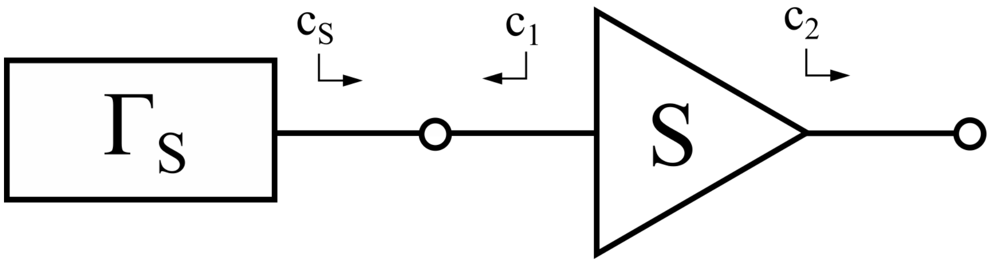

(a) Schematic of a two-port network (an amplifier for example) with source reflection coefficient Γ_s.

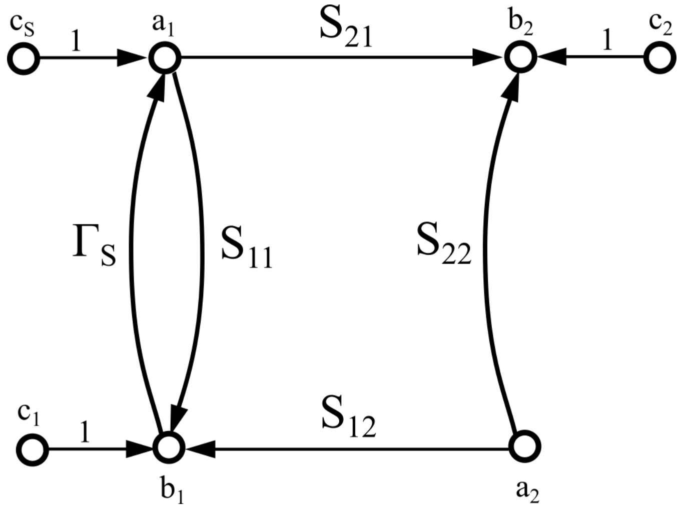

(b) Graph representation of a two-port noisy network with source reflection coefficient Γ_s.

Using the graph in Figure 2.3b, Mason's gain formula [6] gives the well-known expression for available gain and the added noise power. Substituting those into Equation 2.6 results in the following expression for noise factor:

$$NF = 1 + \frac{\overline{\left| c_1\Gamma_s + c_2\left(\frac{1-\Gamma_s S_{11}}{S_{21}}\right)\right|^2}}{k_B T_0(1-|\Gamma_s|^2)} \tag{2.10}$$

Equivalent Noise Resistance

In [4], Wedge derives all four noise parameters. The only further intuition this author can provide is in the derivation of the equivalent noise resistance. R_n is the resistance value for a theoretical thermal voltage noise source at the input of the two-port network. Figure 2.4 depicts a different configuration of noise waves for a two-port network. In this case, both noise waves originate from port 1, but are launched in opposite directions.

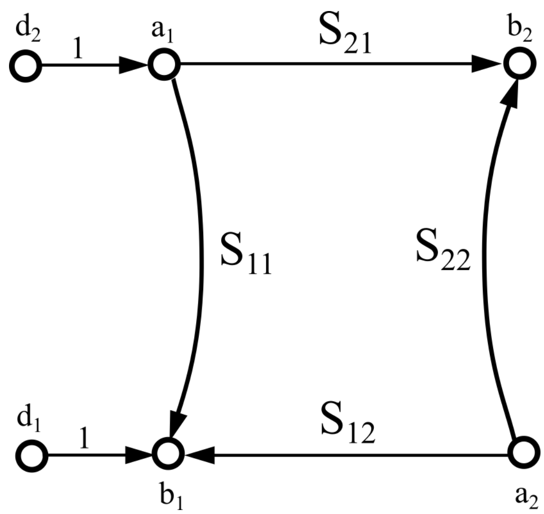

Figure 2.4: Graph representation of a two-port noisy network with noise waves referred to the input.

Equating the graphs in Figures 2.4 and 2.2 gives a simple set of equations:

$$b_1 = c_1 = d_1 + S_{11}d_2$$

$$b_2 = c_2 = S_{21}d_2$$

Therefore,

$$d_2 = \frac{c_2}{S_{21}}$$

$$d_1 = c_1 - \frac{S_{11}c_2}{S_{21}}$$

The total noise wave amplitude from this theoretical source is

$$d_n = d_1 + d_2 = c_1 - \frac{c_2(1+S_{11})}{S_{21}}.$$

The voltage noise power is calculated as

$$\overline{|d_n|^2} = \overline{\left|c_1 - c_2\left(\frac{1+S_{11}}{S_{21}}\right)\right|^2}.$$

In terms of an equivalent noise resistance, the thermal noise voltage is

$$v_n = \sqrt{4k_B T \Delta f R_n}.$$

Equating this to the noise wave expression in a 1-Hz bandwidth,

$$\overline{|v_n|^2} = 4k_B T R_n = Z_0 \overline{\left|c_1 - c_2\left(\frac{1+S_{11}}{S_{21}}\right)\right|^2}.$$

$$\boxed{R_n = \frac{Z_0}{4k_B T}\overline{\left|c_1 - c_2\left(\frac{1+S_{11}}{S_{21}}\right)\right|^2}} \tag{2.11}$$

A similar redefinition of noise waves is used to perform noise wave de-embedding, which is discussed in Section 2.4.

Minimum Noise Temperature and Optimum Source Reflection Coefficient

The expressions for calculating NF_{min} and Γ_{opt} in from scattering parameters and the elements of the noise wave correlation matrix are listed below.

$$\boxed{k_B T_{min} = k_B T_0(NF_{min} - 1) = \frac{\overline{|c_2|^2} - \overline{|c_1 S_{21} - c_2 S_{11}|^2}|\Gamma_{opt}|^2}{|S_{21}|^2(1+|\Gamma_{opt}|^2)}} \tag{2.12}$$

$$\eta = \frac{\overline{|c_2|^2} + \overline{|c_1 S_{21} - c_2 S_{11}|^2}}{\overline{|c_2|^2} S_{11} - \overline{c_1 c_2^*} S_{21}}$$

$$\boxed{\Gamma_{opt} = \frac{\eta}{2}\left(1 - \sqrt{1 - \frac{4}{\eta}}\right)} \tag{2.13}$$

Conceptually, the noise wave representation of two-port noise parameters is very straightforward. Due to the possible correlation between c_1 and c_2, the superposition of noise waves at the output created by placing a non-zero reflection coefficient at the input of the network can result in a much lower added noise power than just $\overline{|c_2|^2}$. The available gain of the network also changes with Γ_s, so the optimal noise match is a minimization of Equation 2.10. The solution to that minimization is of course, Γ_{opt}.

2.3. Noise Wave Subnetwork Growth

For the purposes of computer-aided design of linear microwave networks, computing arbitrary connections and cascades of known networks is much more efficient with wave representations rather than voltages and currents. This approach is universally applicable to all linear networks regardless of complexity. Using graph theory [6], arbitrary network connections are algorithmic and straightforward to implement in software.

The intra-connection (internal) of ports k and l of the same network is given in Equation 2.14 [4]. This function is iterated over all combinations of i and j to compute the resulting network's s-parameters.

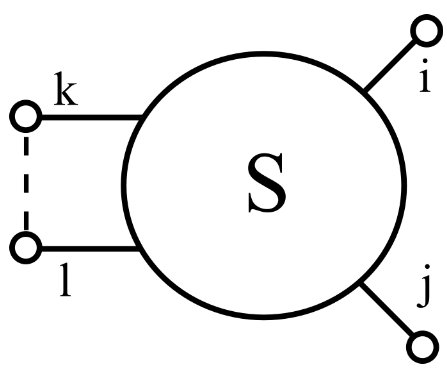

Figure 2.5: The connection of two ports of the same network. The resulting s-parameters can be computed using eq. 2.14.

$$s'_{ij} = \frac{s_{kj}s_{il}(1 - s_{lk}) + s_{lj}s_{ik}(1 - s_{kl}) + s_{kj}s_{ll}s_{ik} + s_{lj}s_{kk}s_{il}}{(1 - s_{kl})(1 - s_{lk}) - s_{kk}s_{ll}} \tag{2.14}$$

Interestingly, Equation 2.14 can also be used for inter-connections between two different networks. By creating a composite s-matrix of the two networks, the intra-connection algorithm can be applied with a subsequent dimensional reduction to arrive at the final network's s-parameters. This is the method used in the open source microwave network Python package, scikit-rf [1].

An example is shown for a network, A, with nA ports and a network, B, with nB ports resulting in a new network, C. The intended equivalent internal ports of this network are combined using Equation 2.14. The extra dimensions generated by this operation are then deleted.

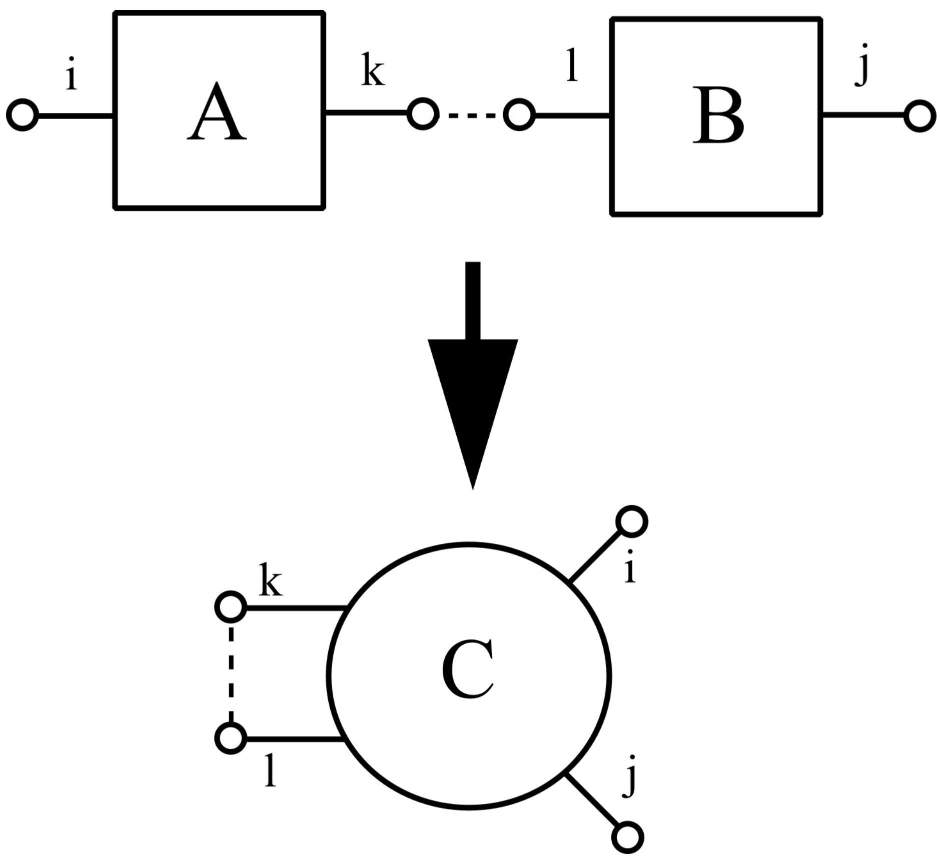

Figure 2.6: The interconnection of two separate networks can be transformed into an intra-connection by combining the two networks' S-parameters into a composite matrix with zeros inserted for the nonexistent port parameters. See eq. 2.15.

$$
\mathbf{C} = \begin{pmatrix}
A_{1,1} & \dots & A_{1,nA} & 0 & \dots & 0 \\
\vdots & \ddots & \vdots & 0 & \dots & 0 \\
A_{nA,1} & \dots & A_{nA,nA} & 0 & \dots & 0 \\
0 & \dots & 0 & B_{1,1} & \dots & B_{1,nB} \\
0 & \dots & 0 & \vdots & \ddots & \vdots \\
0 & \dots & 0 & B_{nB,1} & \dots & B_{nB,nB}
\end{pmatrix} \tag{2.15}
$$

This method is advantageous since only one connection algorithm needs to be implemented.

Many modern netlist or graph based circuit simulation tools use this philosophy to compute user-defined arbitrary networks. The same principles are applied to noise analysis through noise waves and subnetwork growth. From [4], the intra-connection algorithm for the elements of the resulting network's noise wave correlation matrix is given in Equation 2.16.

$$
\begin{aligned}
\overline{c_i' c_j'^*} = \overline{c_i c_j^*} &+ \overline{c_l c_k^*} \frac{\big(S_{ik}(1-S_{kl}) + S_{kk}S_{il}\big)\big(S_{jl}(1-S_{lk}) + S_{ll}S_{jk}\big)^*}{|(1-S_{kl})(1-S_{lk}) - S_{kk}S_{ll}|^2} \\
&+ \overline{c_k c_l^*} \frac{\big(S_{il}(1-S_{lk})S_{ll}S_{ik}\big)\big(S_{jk}(1-S_{kl}) + S_{kk}S_{jl}\big)^*}{|(1-S_{kl})(1-S_{lk}) - S_{kk}S_{ll}|^2} \\
&+ \overline{|c_l|^2} \frac{\big(S_{ik}(1-S_{kl}) + S_{kk}S_{il}\big)\big(S_{jk}(1-S_{kl}) + S_{kk}S_{jl}\big)^*}{|(1-S_{kl})(1-S_{lk}) - S_{kk}S_{ll}|^2} \\
&+ \overline{|c_k|^2} \frac{\big(S_{il}(1-S_{lk}) + S_{ll}S_{ik}\big)\big(S_{jl}(1-S_{lk}) + S_{ll}S_{jk}\big)^*}{|(1-S_{kl})(1-S_{lk}) - S_{kk}S_{ll}|^2} \\
&+ \overline{c_l c_j^*} \left(\frac{S_{ik}(1-S_{kl}) + S_{kk}S_{il}}{(1-S_{kl})(1-S_{lk}) - S_{kk}S_{ll}} \right) + \overline{c_k c_j^*} \left(\frac{S_{il}(1-S_{lk}) + S_{ll}S_{ik}}{(1-S_{kl})(1-S_{lk}) - S_{kk}S_{ll}} \right) \\
&+ \overline{c_i c_l^*} \left(\frac{S_{jk}(1-S_{kl}) + S_{kk}S_{jl}}{(1-S_{kl})(1-S_{lk}) - S_{kk}S_{ll}} \right)^* + \overline{c_i c_k^*} \left(\frac{S_{jl}(1-S_{lk}) + S_{ll}S_{jk}}{(1-S_{kl})(1-S_{lk}) - S_{kk}S_{ll}} \right)^*
\end{aligned} \tag{2.16}
$$

Though slightly more computationally complex, the exact same process for s-parameter subnetwork growth is performed to calculate the noise wave correlation matrix of any arbitrarily connected linear noisy networks. The resulting noise wave correlation matrix; however, relies on both the individual noise correlation matrices and s-parameters of the connected networks.

2.4. De-embedding Noisy Networks

De-embedding microwave networks is a very powerful tool for mathematically removing the effects of test fixtures and accurately setting measurement reference planes. Figure 2.7 shows a common example of a device "embedded" within a test fixture. In order to get an accurate measurement of the device only, the test fixture must be removed from the measurements.

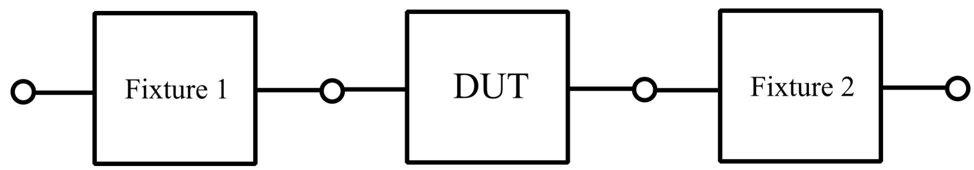

Figure 2.7: Common example of an embedded device. The effects of the fixture must be removed in order to get the device's S-parameters.

Given the S-parameters of the embedding networks, it is certainly possible to reverse the subnetwork growth equations and calculate the device S-parameters; however, these particular problems are easier to solve with Scattering Transfer Parameters (T-parameters). When the total embedded network is a cascade of networks, which is often the case, T-parameters turn a complex problem into a simple matrix multiplication problem.

T-parameters are similar to *ABCD* parameters in that they are designed to simplify the calculation of cascaded networks. They are a mathematical transformation of S-parameters and cannot be directly measured. That transformation is described in eq. 2.17 [7].

$$\begin{pmatrix} b_1 \\ a_1 \end{pmatrix} = \mathbf{T} \begin{pmatrix} a_2 \\ b_2 \end{pmatrix} \tag{2.17}$$

The conversions from S-parameters to T-parameters can be derived from eq. 2.17. The expressions to convert from S-to-T and T-to-S are given below.

$$\mathbf{T} = \frac{1}{S_{21}} \begin{pmatrix} S_{12}S_{21} - S_{11}S_{22} & S_{11} \\ -S_{22} & 1 \end{pmatrix} \tag{2.18}$$

$$\mathbf{S} = \frac{1}{T_{22}} \begin{pmatrix} T_{12} & T_{11}T_{22} - T_{12}T_{21} \\ 1 & -T_{21} \end{pmatrix} \tag{2.19}$$

In the cascade shown in Figure 2.7, the T-parameters of the total network can be computed as

$$\mathbf{T}_{tot} = \mathbf{T}_{fixture,1} \cdot \mathbf{T}_{DUT} \cdot \mathbf{T}_{fixture,2}$$

Therefore,

$$\mathbf{T}_{DUT} = \mathbf{T}_{fixture,1}^{-1} \cdot \mathbf{T}_{tot} \cdot \mathbf{T}_{fixture,2}^{-1} \tag{2.20}$$

scikit-rf (*skrf*) uses this method to quickly de-embed networks. To remove any known two-port network, **S**, from port i of an N-port network, the inverse network is computed and connected at port i. This removes the effects of **S** from the network at port i.

$$\mathbf{S}_{inv} = t2s(s2t(\mathbf{S})^{-1})$$

$s2t$ and $t2s$ are *skrf* functions that implement equations 2.18 and 2.19 respectively. The connection algorithm described in Section 2.3 is used to connect $\mathbf{S}_{inv}$ and compute the final de-embedded network.

2.4.1. T-Parameter Noise Waves

The noise wave model presented by Valk [8] describes the analogous definition of noise waves for T-Parameter two-port networks. The linear combination of waves and wave parameters is given in Equation 2.21.

$$\begin{pmatrix} b_1 \\ a_1 \end{pmatrix} = \mathbf{T} \begin{pmatrix} a_2 \\ b_2 \end{pmatrix} + \begin{pmatrix} b_n \\ -a_n \end{pmatrix} \tag{2.21}$$

The T-parameter noise wave correlation matrix is

$$\mathbf{C}_T = \begin{pmatrix} b_n \\ -a_n \end{pmatrix} \cdot \begin{pmatrix} b_n^* & -a_n^* \end{pmatrix} = \begin{pmatrix} \overline{|b_n|^2} & -b_n a_n^* \\ -b_n^* a_n & \overline{|a_n|^2} \end{pmatrix} \tag{2.22}$$

As there is no direct way to measure these noise parameters, transformations are needed to convert from the S-parameter noise wave correlation matrix to the T-parameter model. A graphical example shown in Figure 2.8 is one way to derive these relations. Dobrowolski in [7] reports his solutions for these transformations; however, there are multiple errors or misprints.

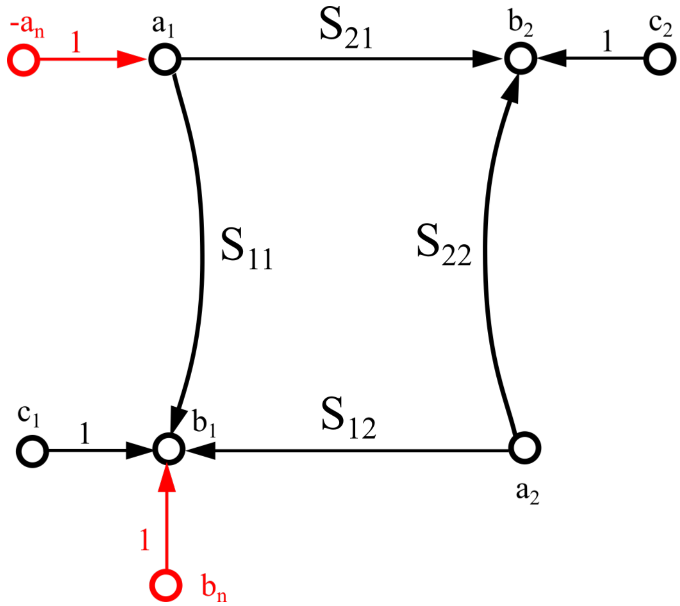

Figure 2.8: Graph representation of the relationships between noise waves c_1, c_2 and b_n, a_n.

Figure 2.8 gives the following expressions:

$$b_1 = c_1 = b_n + S_{11} a_n$$

$$b_2 = c_2 = S_{21} a_n$$

Solving for a_n and b_n,

$$\begin{pmatrix} b_n \\ -a_n \end{pmatrix} = \begin{pmatrix} 1 & -\frac{S_{11}}{S_{21}} \\ 0 & -\frac{1}{S_{21}} \end{pmatrix} \cdot \begin{pmatrix} c_1 \\ c_2 \end{pmatrix} \tag{2.23}$$

$$\mathbf{P}_S = \begin{pmatrix} 1 & -\frac{S_{11}}{S_{21}} \\ 0 & -\frac{1}{S_{21}} \end{pmatrix} \tag{2.24}$$

Substituting eq. 2.23 into eq. 2.22 gives the full transformation between $\mathbf{C}_S$ and $\mathbf{C}_T$:

$$\begin{aligned} \mathbf{C}_T &= \begin{pmatrix} b_n \\ -a_n \end{pmatrix} \cdot \begin{pmatrix} b_n^* & -a_n^* \end{pmatrix} \\ &= \begin{pmatrix} 1 & -\frac{S_{11}}{S_{21}} \\ 0 & -\frac{1}{S_{21}} \end{pmatrix} \cdot \begin{pmatrix} c_1 \\ c_2 \end{pmatrix} \cdot \begin{pmatrix} c_1^* & c_2^* \end{pmatrix} \cdot \begin{pmatrix} 1 & 0 \\ -\frac{S_{11}^*}{S_{21}^*} & -\frac{1}{S_{21}^*} \end{pmatrix} \\ &\boxed{= \mathbf{P}_S \cdot \mathbf{C}_S \cdot \mathbf{P}_S^\dagger} \end{aligned} \tag{2.25}$$

The reverse expressions can be derived by computing the inverse of $\mathbf{P}_S$.

$$\begin{pmatrix} b_n \\ -a_n \end{pmatrix} = \mathbf{P}_S \cdot \begin{pmatrix} c_1 \\ c_2 \end{pmatrix}$$

$$\begin{pmatrix} c_1 \\ c_2 \end{pmatrix} = \mathbf{P}_S^{-1} \cdot \begin{pmatrix} b_n \\ -a_n \end{pmatrix} = \begin{pmatrix} 1 & -S_{11} \\ 0 & -S_{21} \end{pmatrix} \cdot \begin{pmatrix} b_n \\ -a_n \end{pmatrix} \tag{2.26}$$

Converting the S-parameters to T-parameters gives $\mathbf{P}_T$:

$$\mathbf{P}_T = \begin{pmatrix} 1 & -\frac{T_{12}}{T_{22}} \\ 0 & -\frac{1}{T_{22}} \end{pmatrix} \tag{2.27}$$

$$\boxed{\mathbf{C}_S = \mathbf{P}_T \cdot \mathbf{C}_T \cdot \mathbf{P}_T^\dagger} \tag{2.28}$$

2.4.2. De-embedding Cascaded Noisy Networks

De-embedding the noise waves of cascaded networks is made simple with the T-parameter representation of the noise wave correlation matrix. Consider the last two networks in the cascade from Figure 2.7. This section roughly follows the

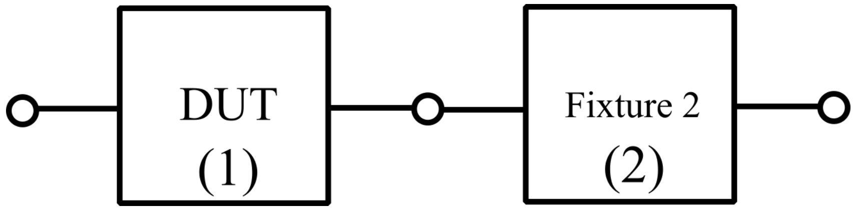

Figure 2.9: A two network cascade with the network of interest positioned first in the chain.

The two networks can be represented by the following expressions:

$$\begin{pmatrix} b_1^{(1)} \\ a_1^{(1)} \end{pmatrix} = \mathbf{T}^{(1)} \begin{pmatrix} a_2^{(1)} \\ b_2^{(1)} \end{pmatrix} + \begin{pmatrix} b_n^{(1)} \\ -a_n^{(1)} \end{pmatrix} \tag{2.29}$$

$$\begin{pmatrix} b_1^{(2)} \\ a_1^{(2)} \end{pmatrix} = \mathbf{T}^{(2)} \begin{pmatrix} a_2^{(2)} \\ b_2^{(2)} \end{pmatrix} + \begin{pmatrix} b_n^{(2)} \\ -a_n^{(2)} \end{pmatrix} \tag{2.30}$$

When cascading $\mathbf{T}^{(1)}$ and $\mathbf{T}^{(2)}$, port 2 of network 1 is connected to port 1 of network 2.

$$\begin{pmatrix} a_2^{(1)} \\ b_2^{(1)} \end{pmatrix} = \begin{pmatrix} b_1^{(2)} \\ a_1^{(2)} \end{pmatrix}$$

.

Substituting eq. 2.30 into eq. 2.29 gives

$$\begin{pmatrix} b_1^{(1)} \\ a_1^{(1)} \end{pmatrix} = \mathbf{T}^{(1)}\mathbf{T}^{(2)} \begin{pmatrix} a_2^{(2)} \\ b_2^{(2)} \end{pmatrix} + \mathbf{T}^{(1)} \begin{pmatrix} b_n^{(2)} \\ -a_n^{(2)} \end{pmatrix} + \begin{pmatrix} b_n^{(1)} \\ -a_n^{(1)} \end{pmatrix} \tag{2.31}$$

It is clear from eq. 2.31 above that the resulting noise waves of the cascade are

$$\begin{pmatrix} b_n^{(1+2)} \\ -a_n^{(1+2)} \end{pmatrix} = \mathbf{T}^{(1)} \begin{pmatrix} b_n^{(2)} \\ -a_n^{(2)} \end{pmatrix} + \begin{pmatrix} b_n^{(1)} \\ -a_n^{(1)} \end{pmatrix}$$

The T-parameter noise wave correlation matrix is clearly

$$\begin{aligned}\mathbf{C}_T^{(1+2)} &= \begin{pmatrix} b_1^{(1+2)} \\ a_1^{(1+2)} \end{pmatrix} \cdot \begin{pmatrix} b_1^{(1+2)*} & a_1^{(1+2)*} \end{pmatrix} \\ &= \boxed{\mathbf{C}_T^{(1)} + \mathbf{T}^{(1)} \cdot \mathbf{C}_T^{(2)} \cdot \mathbf{T}^{(1)\dagger}}\end{aligned} \tag{2.32}$$

With eq. 2.32, noise wave de-embedding of cascaded networks is easily performed. If the total cascade's noise correlation matrix is known as well as either of the networks in the cascade, the remaining network's noise correlation matrix is known. If solving for the first network in the cascade,

$$\mathbf{C}_T^{(1)} = \mathbf{C}_T^{(1+2)} - \mathbf{T}^{(1)} \cdot \mathbf{C}_T^{(2)} \cdot \mathbf{T}^{(1)\dagger} \tag{2.33}$$

Solving for the second network in the cascade can be performed by further rearranging eq. 2.32.

$$\mathbf{C}_T^{(2)} = \left[\mathbf{T}^{(1)}\right]^{-1} \cdot \left(\mathbf{C}_T^{(1+2)} - \mathbf{C}_T^{(1)}\right) \cdot \left[\mathbf{T}^{(1)\dagger}\right]^{-1} \tag{2.34}$$

The expressions derived in this subsection are included in [7] but are also included in here as a reference for the math implemented in open source software (this work).

2.5. Implementation in Python and *scikit-rf*

This section is a collection of example problems computed in Python and *scikit-rf*. The concepts from the previous sections are included. For a lot of the examples in this section and Section 2.6, two modeled hybrid couplers are used. The scattering parameters for those couplers, 2.4GHz 90° and 180° 3-dB hybrids, are summarized in Figure 2.10.

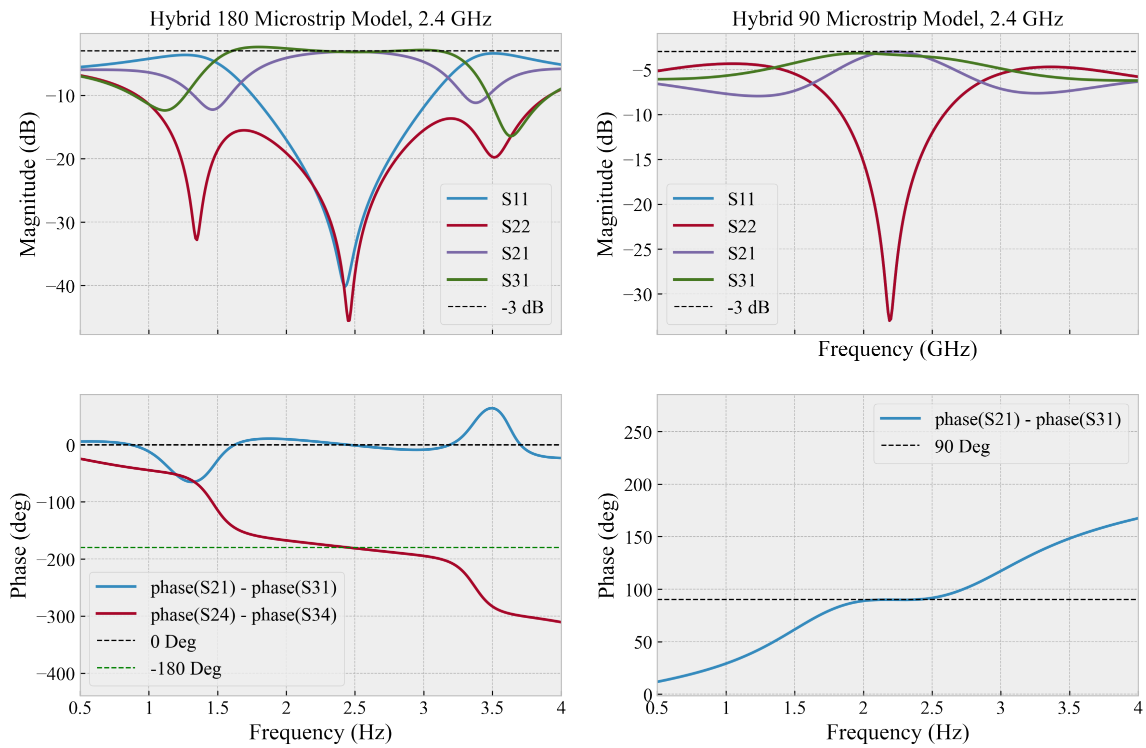

Figure 2.10: The magnitude and phase responses of the modeled couplers.

All of the simulated results using *skrf* were plotted against Keysight's Advanced Design System (ADS).

2.5.1. Example 1: Noise Figure of Passive Networks

Since a passive network's noise figure is completely defined by its scattering parameters (see eq. 2.8), the calculation is easily performed.

```
import skrf as rf

# create the network
H180 = rf.Network("data/Hybrid180_ADS_MLIN_290K.s4p")

# port 2, indexed from 0
port = 1

# list nf in dB at port 2 for every frequency
H180.nf_w(Ta=290, dB=True)[:, port]
```

The noise figure for both couplers is plotted in Figure 2.11 against the noise figure calculated in ADS. The noise figures are automatically calculated on network object creation if it passes a passivity check. The results are identical to ADS.

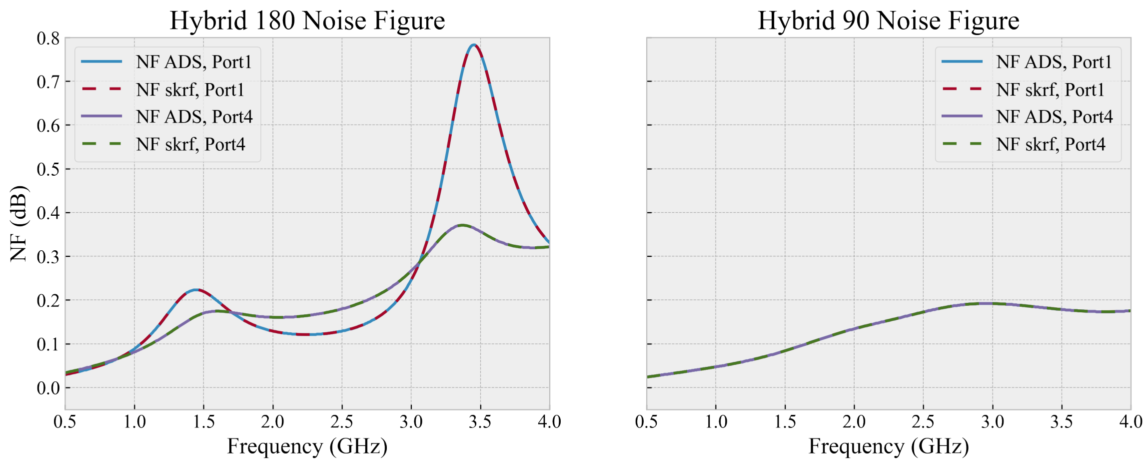

Figure 2.11: The noise figure of the two couplers plotted against ADS results.

2.5.2. Example 2: Noise Parameters of an Active Network

The calculation of an active network's noise figure is more complicated. Since the network is not in thermodynamic equilibrium, the simple expressions for noise figure and the noise wave correlation matrix break down. For this reason, the calculation of noise figure and noise parameters of active networks in *skrf* requires that the supplied scattering parameters also include the noise parameters. This is the same for all microwave analysis tools. In *skrf*, the noise parameters or the noise wave correlation matrix vs. frequency may be included.

If noise parameters are supplied on network creation, the noise wave correlation matrix is automatically calculated. Any subsequent calculations of noise parameters are calculated from the noise wave correlation matrix and the expressions listed in Section 2.2.2. It might seem redundant to convert the noise parameters to noise waves and then back to noise parameters; however, in order to compute the noise parameters of connected and cascaded networks, noise waves and the subnetwork growth algorithms must be used. Thus, noise waves are the more natural representation of noise for these networks. The following example code uses the manufacturer supplied scattering parameters and noise parameters for the Mini-Circuits SAV-541+ high electron mobility transistor (HEMT).

```python
import skrf as rf

# create the network
sav = rf.Network("data/SAV_541_S2_3V_60mA.s2p")

# list the minimum noise figure in dB
sav.nfmin_w(dB=True)

# list the equivalent noise resistance
sav.rn_w()

# list the optimum source reflection coefficient
sav.gopt_w()
```

Figure 2.12 shows the calculated noise parameters for this device up to 4GHz. The agreement with ADS is excellent.

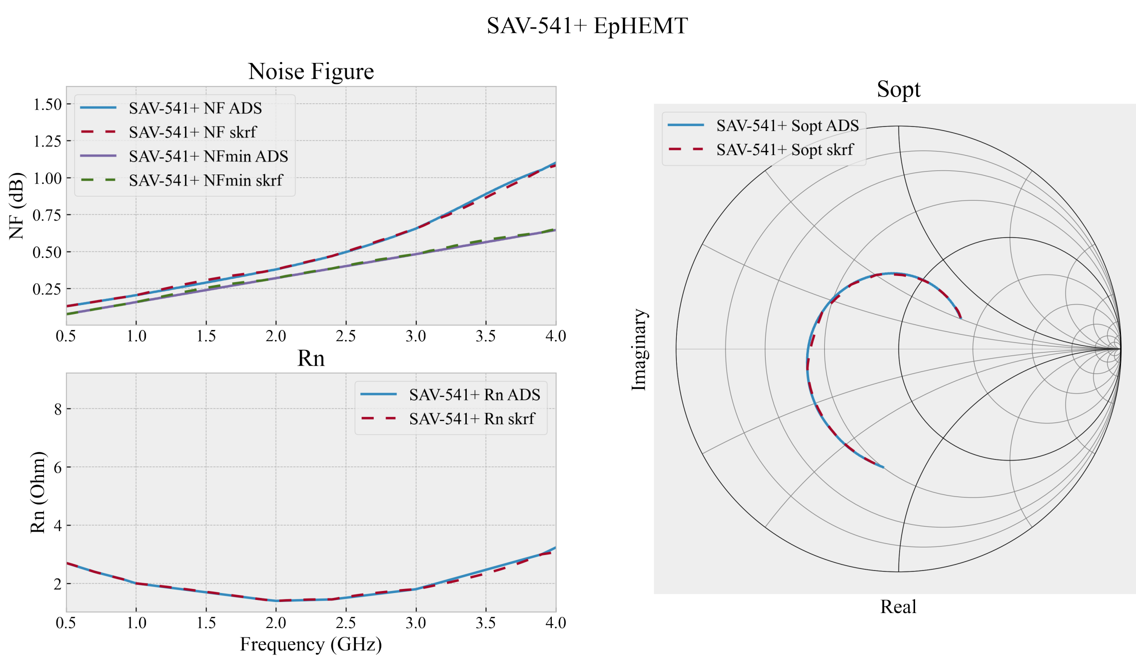

Figure 2.12: The noise parameters of the SAV-541+ HEMT from Mini-Circuits. The noise parameters are plotted against the noise parameters calculated by ADS.

2.5.3. Example 3: Noise Parameters of a Balanced Amplifier

To test the subnetwork growth algorithms for noise, a simple configuration of active and passive networks is generated. The noise properties of the individual networks are known; however, the total connected network's noise properties are unknown. A balanced amplifier uses the unique properties of a 90°-hybrid to generate destructive interference for an improved input and output match. A schematic of this is shown in Figure 2.13.

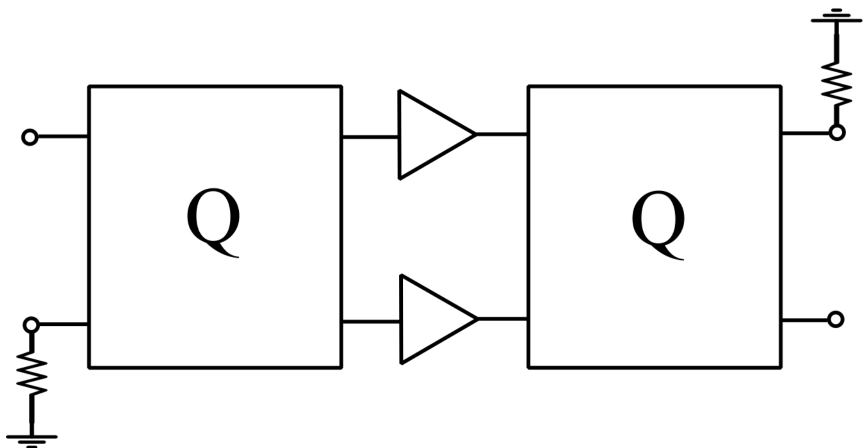

Figure 2.13: Schematic of a balanced amplifier. Two identical RF transistors are used with two quadrature hybrids. The noise properties of the individual networks are known.

The following code block creates a few network objects from file-based data and manually connects them to create a balanced amplifier.

```python
import skrf as rf

# create the networks
load = rf.Network('data/Load_50Ohm_290K.s1p')
sav = rf.Network("data/SAV_541_S2_3V_60mA.s2p")
H90 = rf.Network("data/Hybrid90_ADS_MLIN_290K.s4p")

# perform the network connections
u00 = rf.network.connect(H90, 3, load, 0)
u01 = rf.network.connect(H90, 1, load, 0)
u1 = rf.network.connect(sav, 0, u00, 1)
u1.renumber([0, 1, 2], [1, 0, 2])
u2 = rf.network.connect(sav, 0, u1, 2)
u2.renumber([0, 1, 2], [2, 0, 1])
```

```
u3 = rf.network.connect(u2, 1, u01, 0)

# balanced amplifier network
ba = rf.network.innerconnect(u3, 1, 3)
```

Every call to the connection function executes the subnetwork growth algorithms given in Section 2.3. The handling of these functions while preserving the noise properties of the resulting network was previously unimplemented in *skrf*. The computed noise parameters of the balanced amplifier network are plotted in Figure 2.14.

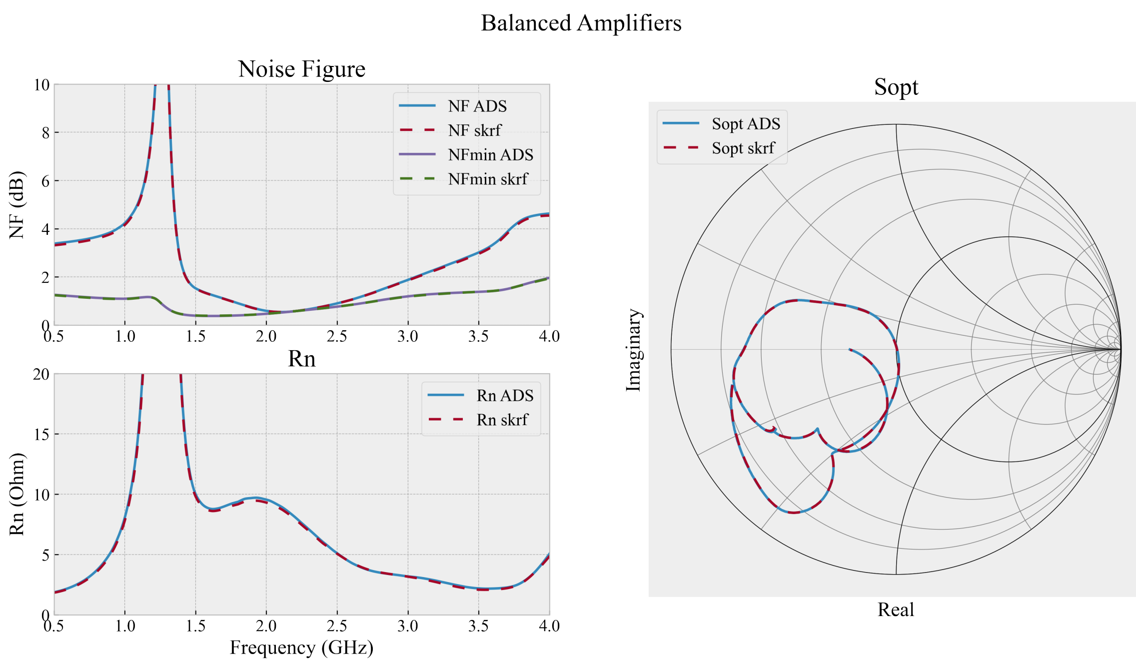

Figure 2.14: Noise parameters of a balanced amplifier computed synthetically in *skrf*. The results are plotted against ADS. This was previously not possible in *skrf*.

This is a very important result. The correct computation of interconnected noisy networks is a very powerful tool, especially for a free microwave analysis package. The author hopes this open source contribution helps lower the barrier for state-of-the-art analysis in the microwave engineering community.

2.5.4. Example 4: De-embedding Noisy Networks

The following example shows how to cascade two noisy networks and then de-embed the cascade given that one of the networks is known. This operation has not been fully implemented in *skrf*, as the 'inverse' operation (see Section 2.4) for a network does not preserve the noise wave correlation matrix of the network. This will require a change to the typical de-embedding procedure used in *skrf*. The typical procedure is shown below:

```python
import skrf as rf

# create the network
sav = rf.Network("data/SAV_541_S2_3V_60mA.s2p")

# dummy cascade operation
embedded_sav = sav ** sav ** sav

# de-embed operation (without noise)
single_sav = sav.inv ** embedded_sav ** sav.inv
```

The remaining code blocks and figures in this section outline how to perform noise wave de-embedding for the 'sav' network in two different network cascades: first network in a cascade and second network in a cascade.

```python
import skrf as rf

# turn the quadrature hybrid into a 2-port (ports 1 and 2)
# terminate ports 3 and 4 with a load
t0 = rf.network.connect(H90, 3, load, 0)
H9021 = rf.network.connect(t0, 2, load, 0)

# create two different cascades
# quadrature first
cascade1 = rf.network.connect(H9021, 1, sav, 0)

# quadrature second
cascade2 = rf.network.connect(sav, 1, H9021, 0)
```

The noise parameters of the two cascade networks are summarized in Figure 2.15.

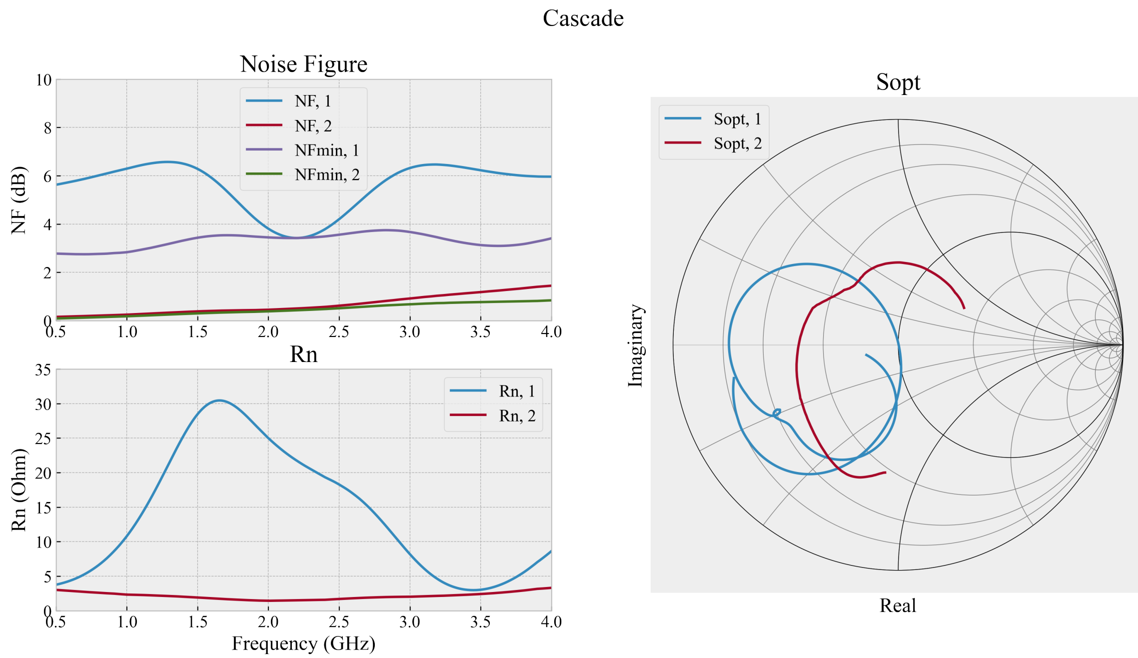

Figure 2.15: Noise parameters of two cascades of the SAV-541+ Mini-Circuits HEMT and a quadrature hybrid. Cascade 1 has the quadrature first and cascade 2 has the quadrature second.

The following code demonstrates how to de-embed 'sav' from cascade 1. Note that this code will change in the final implementation. The operations will be more object-oriented. The '@' character represents a dot product operation.

```
import numpy as np

# compute the scattering parameters of the de-embedded network
# the noise calculation will be wrong
deembed1 = H9021.inv ** cascade1

# compute the NWCM T-transform for the full network
PS12 = rf.network.ps(cascade1.s)
# compute the hermitian transpose of the above
# this is done manually due to the shape of the arrays
# dimension 0 is frequency
PS12_H = np.empty(PS12.shape, dtype=complex)
for f in range(0, PS12.shape[0]):
    PS12_H[f] = np.conjugate(PS12[f]).T
# T-parameter NWCM of cascade 1
CT12 = PS12 @ cascade1.nwcm @ PS12_H

```

```
# T-transform for H90 NWCM
PS1 = rf.network.ps(H9021.s)
# compute the hermitian transpose of above
PS1_H = np.empty(PS1.shape, dtype=complex)
for f in range(0, PS1.shape[0]):
    PS1_H[f] = np.conjugate(PS1[f]).T
# T-parameter NWCM of H90
CT1 = PS1 @ H9021.nwcm @ PS1_H

# T-parameters of H90
T1 = H9021.t
# compute the inverse and inverse hermitian transpose of above
T1_INV = np.empty(T1.shape, dtype=complex)
T1_INV_H = np.empty(T1.shape, dtype=complex)
for f in range(0, T1.shape[0]):
    T1_INV[f] = np.linalg.inv(T1[f])
    T1_INV_H[f] = np.linalg.inv(np.conjugate(T1[f]).T)

# de-embed network 2 noise (sav)
CT2 = T1_INV @ (CT12 - CT1) @ T1_INV_H
# S-transform for CT2
PT2 = rf.network.pt(sav.t)
# compute hermitian transpose
PT2_H = np.empty(PT2.shape, dtype=complex)
for f in range(0, PT2.shape[0]):
    PT2_H[f] = np.conjugate(PT2[f]).T

# calculate NWCM of sav
CS2 = PT2 @ CT2 @ PT2_H
deembed1.nwcm = CS2
```

The following code similarly demonstrates how to de-embed 'sav' from cascade 2.

```
# compute the scattering parameters of the de-embedded network
# the noise calculation will be wrong
deembed2 = cascade2 ** H9021.inv

# compute the NWCM T-transform for the full network
PS12 = rf.network.ps(cascade2.s)
PS12_H = np.empty(PS12.shape, dtype=complex)
for f in range(0, PS12.shape[0]):
    PS12_H[f] = np.conjugate(PS12[f]).T
CT12 = PS12 @ cascade2.nwcm @ PS12_H

# T-parameters for the sav network
```

```
T1 = sav.t
T1_H = np.empty(T1.shape, dtype=complex)
for f in range(0, T1.shape[0]):
    T1_H[f] = np.conjugate(T1[f]).T

# T-transform for H90 nwcm
PS2 = rf.network.ps(H9021.s)
PS2_H = np.empty(PS2.shape, dtype=complex)
for f in range(0, PS2.shape[0]):
    PS2_H[f] = np.conjugate(PS2[f]).T
# T-parameter NWCM of CT2
CT2 = PS2 @ H9021.nwcm @ PS2_H

# compute de-embedded T-parameter nwcm
CT1 = CT12 - T1 @ CT2 @ T1_H
# S-transform for de-embedded nwcm
PT1 = rf.network.pt(sav.t)
PT1_H = np.empty(PT1.shape, dtype=complex)
for f in range(0, PT1.shape[0]):
    PT1_H[f] = np.conjugate(PT1[f]).T

# compute final sav NWCM
CS1 = PT1 @ CT1 @ PT1_H
deembed2.nwcm = CS1
```

The de-embedded noise parameters are plotted against the original network's noise parameters in Figure 2.16.

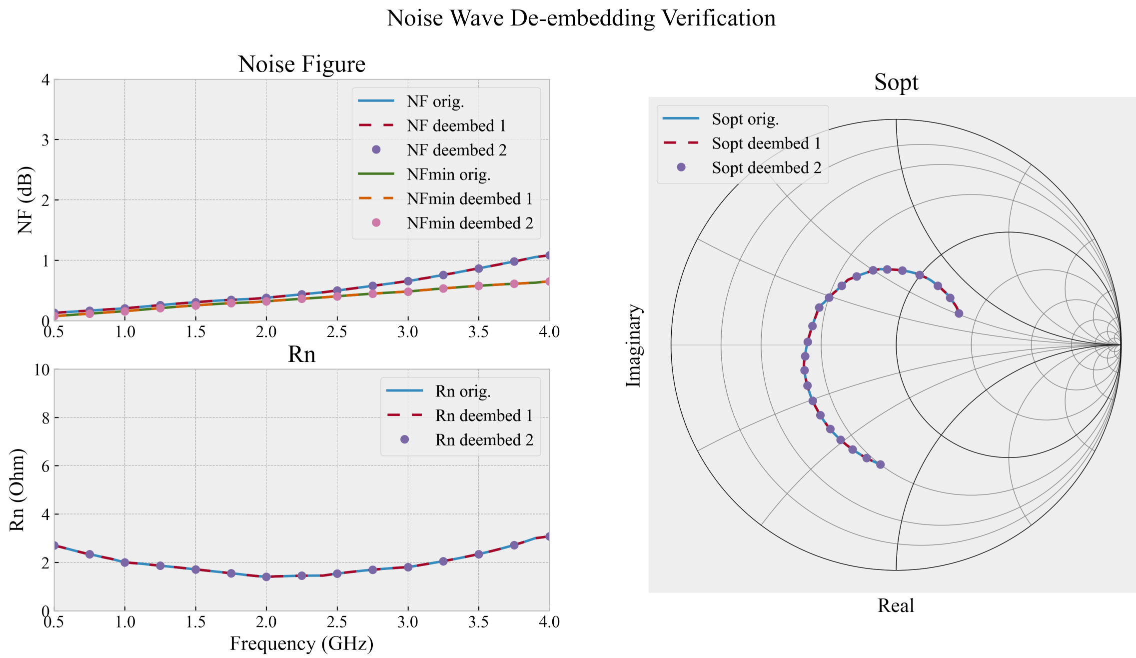

Figure 2.16: Noise parameters of the original SAV network, de-embedded SAV from cascade 1, and de-embedded SAV from cascade 2.

Clearly the noise parameters of the de-embedded networks are recovered correctly. The ability to remove the noise contributions from test fixtures and other elements within a cascade is another very powerful tool for this software toolkit.

2.6. Linear AC Noise Voltage Simulator

The following section describes a simple linear noise power simulator. Given any N-port network with scattering parameter matrix S and noise wave correlation matrix C_s, the noise power at any port is calculated. This noise power is calculated as simply $\frac{\overline{|v_{tot_i}|^2}}{R_i}$, where v_{tot_i} is the noise voltage at port i from the network itself, port terminations, and any user-defined voltage noise sources with user-defined correlation.

In terms of voltage noise, the noise factor for any network at port i is

$$NF_i = \frac{\frac{\overline{|v_{n_i}|^2}}{R_i} + \sum_{j \neq i}^{N} kT_a B |S_{ij}|^2}{\sum_{j \neq i}^{N} kT_a B |S_{ij}|^2} = 1 + \frac{\overline{|v_{n_i}|^2}}{R_i \sum_{j \neq i}^{N} kT_a B |S_{ij}|^2}. \tag{2.35}$$

Therefore,

$$\frac{\overline{|v_{n_i}|^2}}{R_i} = \big(NF_i - 1\big)\sum_{j\neq i}^{N} kT_aB|S_{ij}|^2 \tag{2.36}$$

To include noise from terminations, the expression can be modified as follows:

$$\frac{\overline{|v_{n_i}|^2}}{R_i} = \big(NF_i - 1\big)\sum_{j\neq i}^{N} kT_aB|S_{ij}|^2 + \sum_{j\neq i}^{N} kT_jB|S_{ij}|^2 + kT_iB\big|(1+S_{ii})\big|^2 \tag{2.37}$$

T_j and T_i are the noise temperatures of the terminations. Equation 2.38 allows for the addition of voltage noise sources at any port. User-defined cross-correlation between the voltage sources is handled as well.

$$\begin{aligned}\frac{v_{tot_i}^2}{R_i} = {} & \big(NF(i) - 1\big)\sum_{j\neq i}^{N} kT_aB|S_{ij}|^2 + \sum_{j\neq i}^{N} kT_jB|S_{ij}|^2 + kT_iB\big|(1+S_{ii})\big|^2 \\ & + \sum_{j\neq i}^{N}\left|\frac{v_{n_j}}{\sqrt{R_j}}S_{ij}\right|^2 + \left|\frac{v_{n_i}}{\sqrt{R_i}}(1+S_{ii})\right|^2 \\ & + \sum_{j\neq i}^{N}\sum_{k\neq j}^{N}\sqrt{\left|\frac{v_j}{\sqrt{R_j}}\right|^2\left|\frac{v_k}{\sqrt{R_k}}\right|^2}\big(C_{jk}S_{ij}S_{ik}^*\big) \\ & + \sum_{k=1,k\neq i,j=i}^{k=N}\sqrt{\left|\frac{v_j}{\sqrt{R_j}}\right|^2\left|\frac{v_k}{\sqrt{R_k}}\right|^2}\big(C_{jk}(1+S_{ij})S_{ik}^*\big) \\ & + \sum_{j=1,j\neq i,k=i}^{j=N}\sqrt{\left|\frac{v_j}{\sqrt{R_j}}\right|^2\left|\frac{v_k}{\sqrt{R_k}}\right|^2}\big(C_{jk}S_{ij}(1+S_{ik})^*\big)\end{aligned} \tag{2.38}$$

Figure 2.17 shows the simulated results of the port noise powers for a modeled microstrip 2.4 GHz 90° hybrid coupler, which was generated by the lossy coupler, the thermal noise from the terminations, and two voltage noise sources of 2.4 uVrms at ports 1 and 2. The cross-correlation between the sources is set to $\frac{1}{\sqrt{2}}(-1+j)$ The noise bandwidth is 1 MHz. The data is compared to the results from an equivalent AC linear noise simulation in Keysight's Advanced Design System (ADS).

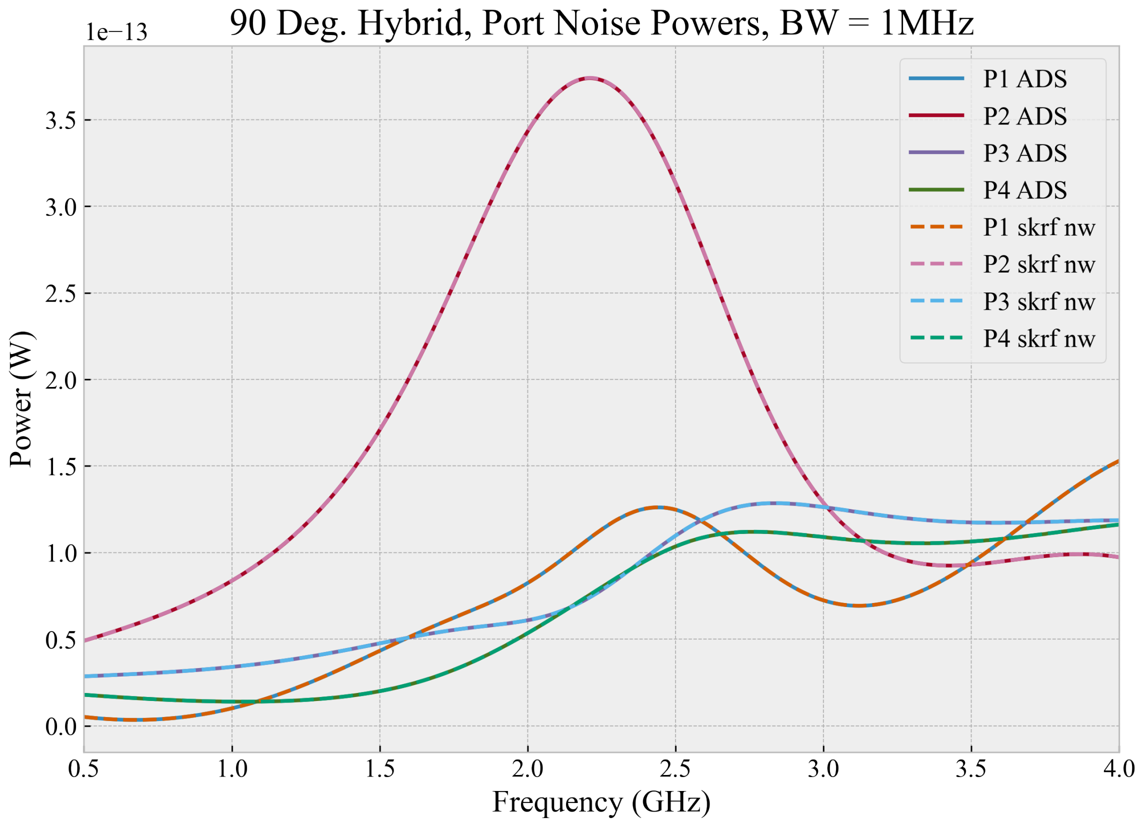

Figure 2.17: Simulation of port voltage noise for a microstrip modeled 90 degree hybrid coupler. The noise from terminations is included. Two voltage noise sources are present at ports 1 and 2, with a correlation of $\frac{1}{\sqrt{2}}(-1+j)$. The results are compared with the equivalent simulation in Keysight ADS.

The results are clearly identical. To further demonstrate the utility of this function, a few more examples are provided. In [2], Wedge explains how the cross-correlation of two noise waves can be measured with the use of a 90° and a 180° hybrid coupler. This is explained below.

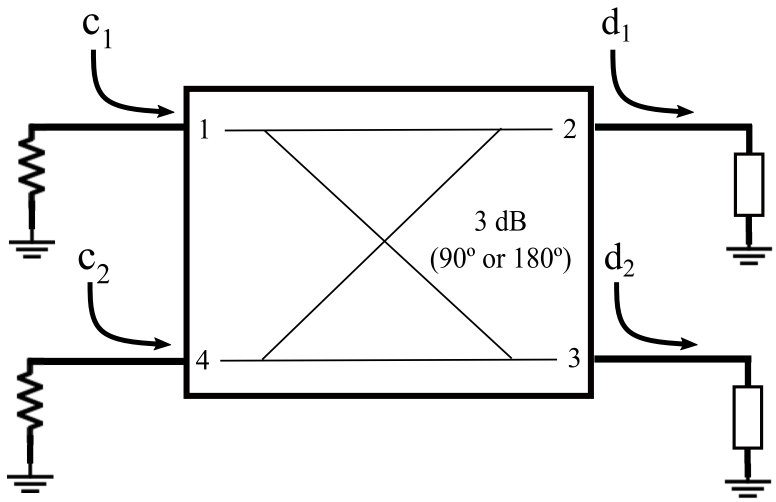

Figure 2.18: Hybrid coupler with incident noise waves c_1 and c_2 and scattered waves d_1 and d_2. The 180° hybrid can isolate the real part of the cross-correlation, $c_1c_2^*$. The 90° hybrid can isolate the imaginary part of the cross-correlation.

Considering the network in Figure 2.18, the output noise waves d_1 and d_2 in the case of the 180° hybrid are

$$d_1 = \frac{1}{\sqrt{2}}(c_1 - c_2)$$

$$d_2 = \frac{1}{\sqrt{2}}(c_1 + c_2)$$

.

Calculating the powers gives

$$\overline{|d_1|^2} = \frac{1}{2}(\overline{|c_1|^2} + \overline{|c_2|^2}) - \Re\{c_1c_2^*\}$$

$$\overline{|d_2|^2} = \frac{1}{2}(\overline{|c_1|^2} + \overline{|c_2|^2}) + \Re\{c_1c_2^*\}$$

$$\boxed{2\Re\{c_1c_2^*\} = \overline{|d_2|^2} - \overline{|d_1|^2}}$$

Now consider a 90° hybrid.

$$d_1 = \frac{1}{\sqrt{2}}(c_1 - jc_2)$$

$$d_2 = \frac{1}{\sqrt{2}}(c_2 - jc_1)$$

$$\overline{|d_1|^2} = \frac{1}{2}(\overline{|c_1|^2} + \overline{|c_2|^2}) - \Im\{c_1 c_2^*\}$$

$$\overline{|d_2|^2} = \frac{1}{2}(\overline{|c_1|^2} + \overline{|c_2|^2}) + \Im\{c_1 c_2^*\}$$

$$\boxed{2\Im\{c_1 c_2^*\} = \overline{|d_2|^2} - \overline{|d_1|^2}}$$

Using modeled S-parameters for 2.4GHz hybrid couplers and the expressions above, the cross-correlation of two user-defined correlated voltage noise sources was computed. These couplers are narrow-band microstrip models, so the error increases significantly as the frequency deviates from the design frequency.

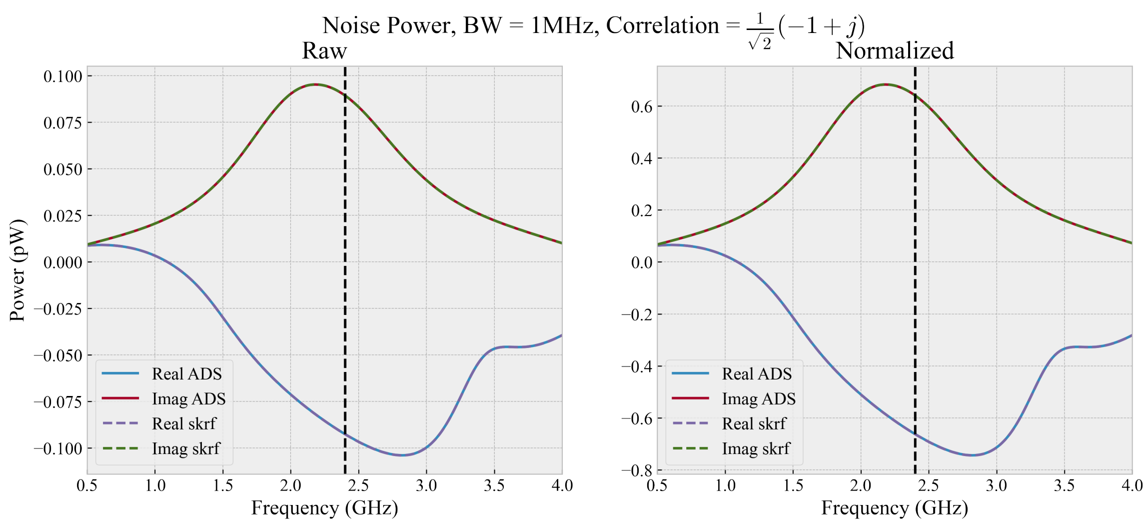

Figure 2.19: Plots showing the simulated noise powers at the outputs of a 90° and a 180° coupler. The input noise correlation was defined to be $\frac{1}{\sqrt{2}}(-1+j)$. The results show a normalized correlation that equals the input correlation.

Figure 2.19 shows that at the design frequency, Wedge's method of measuring the cross-correlation of two noise waves works as intended. Again, the results using this software and the results from ADS are identical.

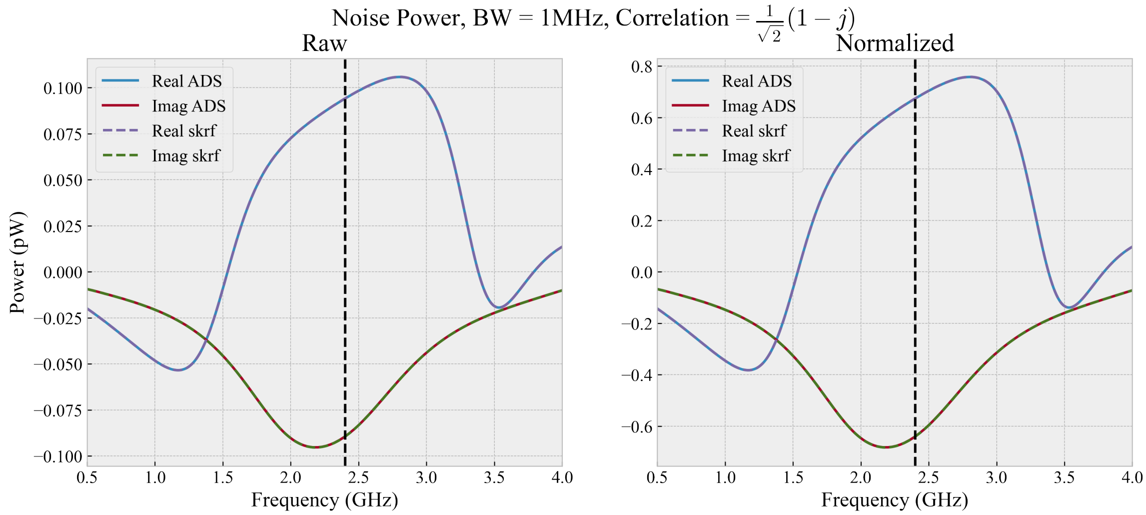

Figure 2.20: Plots showing the simulated noise powers at the outputs of a 90° and a 180° coupler. The input noise correlation was defined to be $\frac{1}{\sqrt{2}}(1-j)$. The results show a normalized correlation that equals the input correlation.

Figure 2.20 is the final example showing the same simulation as in Figure 2.19 but with a cross-correlation of $\frac{1}{\sqrt{2}}(1-j)$. In both cases, the 180° hybrid outputs give $\Re\{c_1 c_2^*\}$, and the 90° hybrid outputs give $\Im\{c_1 c_2^*\}$. This work is slightly different from the noise wave analysis presented in previous sections of this chapter; however, it is a useful tool for computing simple noise voltages present at a network's ports.

2.7. Conclusion and Future Work

This work represents a major contribution to a popular open source microwave analysis software tool. The noise wave framework allows for a set of universal linear network operations that preserve all noise properties. While the physical mechanisms of electrical noise can be very broad and conceptually complex especially in high frequency circuits, the noise wave abstraction provides an unique, holistic approach to noisy network analysis.

Further development is ongoing for a more robust implementation in *skrf*. The merge will come.

Bibliography

[1] A. Arsenovic et al., "scikit-rf: An Open Source Python Package for Microwave Network Creation, Analysis, and Calibration [Speaker's Corner]," in IEEE Microwave Magazine, vol. 23, no. 1, pp. 98-105, Jan. 2022, doi: 10.1109/MMM.2021.3117139.

[2] S. W. Wedge and D. B. Rutledge, "Noise waves and passive linear multiports," IEEE Microwave and Guided Wave Letters, vol. 1, no. 5, pp. 117–119, May 1991, doi: 10.1109/75.89082.

[3] H. Bosma, "On the theory of linear noisy systems," Phd Thesis 1, Technische Hogeschool Eindhoven, Eindhoven, 1967. doi: 10.6100/IR109175.

[4] S. W. Wedge, "Computer-Aided Design of Low Noise Microwave Circuits," California Institute of Technology, 1991.

[5] R. Q. Twiss, "Nyquist's and Thevenin's Theorems Generalized for Nonreciprocal Linear Networks", Journal of Applied Physics 26, 599-602 (1955)

[6] S. J. Mason, "Feedback Theory-Further Properties of Signal Flow Graphs," in Proceedings of the IRE, vol. 44, no. 7, pp. 920-926, July 1956, doi: 10.1109/JRPROC.1956.275147.

[7] J. A. Dobrowolski, RF and Microwave Circuit Analysis and Design. Artech House, Inc., 2016.

[8] E. C. Valk, D. Routledge, J. F. Vaneldik and T. L. Landecker, "De-embedding two-port noise parameters using a noise wave model," in IEEE Transactions on Instrumentation and Measurement, vol. 37, no. 2, pp. 195-200, June 1988, doi: 10.1109/19.6051.

CHAPTER 3

Broadband Measurements of 35nm InP HEMT Devices and MMICs

Through a major collaboration with Dominion Microprobes, Virginia Diodes, Keysight Technologies, and Form Factor, the first continuous DC-220GHz on-wafer measurement system is currently under development. This author was lucky enough to be able to use this system to perform measurements of Northrop Grumman Space System's (NGC) 35nm InP HEMTs and MMICs. This chapter outlines those measurements, which include several low-noise amplifiers and parameter extractions of single devices embedded in 50Ω grounded coplanar waveguide transmission lines.

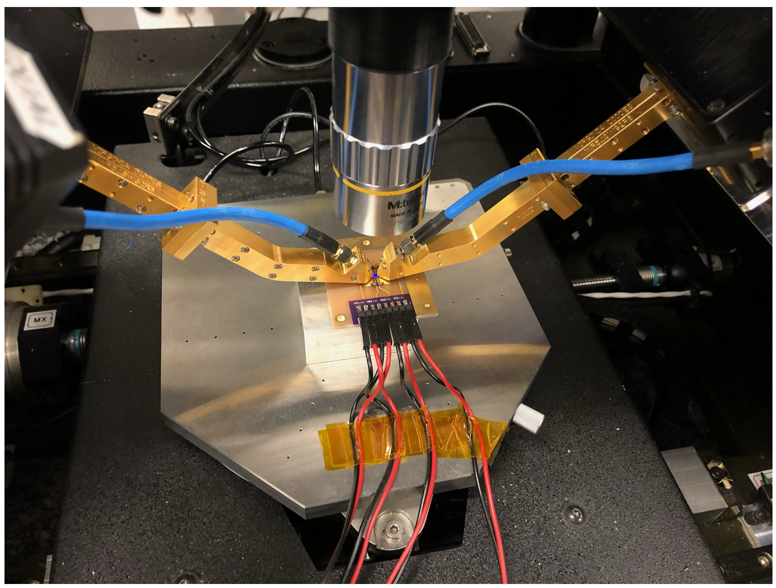

Figure 3.1: Photograph of a mounted InP MMIC LNA measured with the broadband probe system. The diced MMIC is mounted onto a custom gold-finished FR4 PCB.

3.1. The High Electron Mobility Transistor

One of the most important technologies enabling advancement in the terahertz region of the electromagnetic spectrum is the HEMT. The high electron mobility transistor (HEMT) has emerged in the past few decades as the dominant technology for microwave, millimeter-wave, and sub-millimeter wave low-noise circuits. HEMTs are heterojunction devices with exceptional switching speeds, high gain, and fabrication techniques compatible with monolithic processing, making them excellent devices for high frequency low-noise and power amplifiers, mixers, and oscillators.

The structure of the high electron mobility transistor is specifically designed for superior majority carrier transport. The band diagram of a typical HEMT device is shown in Figure 3.2. A heterojunction is a semiconductor contact made between two materials with dissimilar bandgap energies. As with any heterojunction device such as semiconductor lasers, LEDs, and heterostructure bipolar transistors (HBTs), large bandgap discontinuities exist in both the conduction and valence bands. The wide bandgap material is doped n-type while energetically devoid of carriers by the metal-semiconductor gate electrode junction, or zero-bias Schottky contact. The narrow bandgap material is doped lightly p-type or un-doped, which results in a narrow portion of the conduction band to dip below the Fermi level at the heterojunction interface. This is the core mechanism of conduction in the HEMT and results in a high free carrier concentration in that region energetically below the Fermi level.

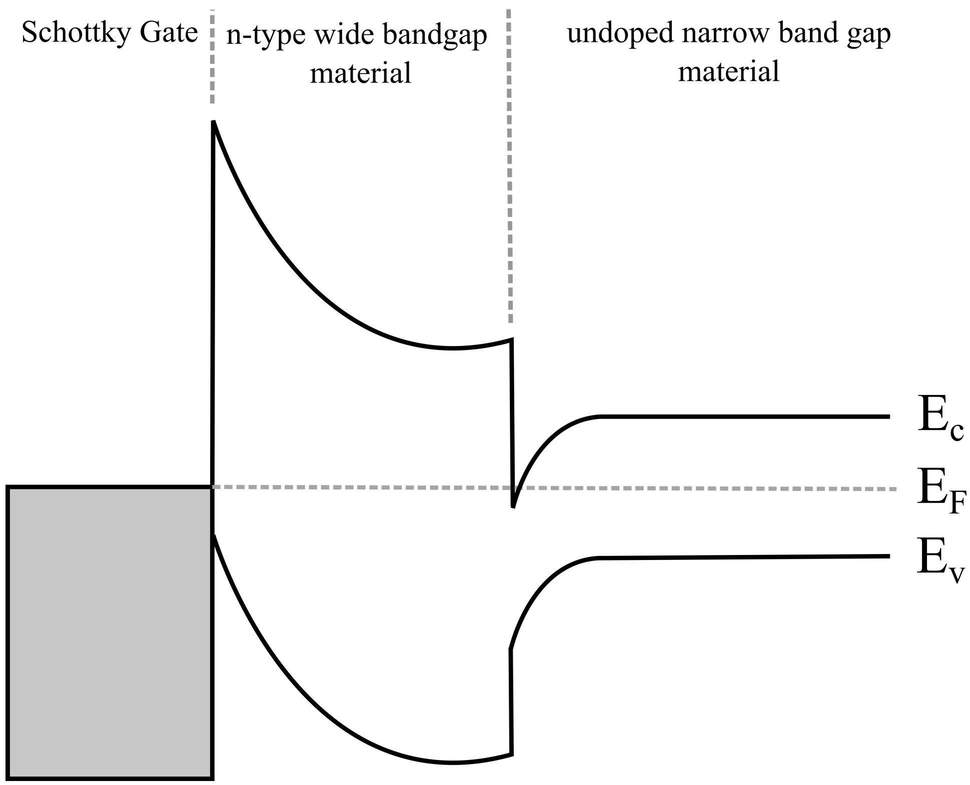

Figure 3.2: Band diagram and free electron concentration in one dimension.

This high carrier concentration exists within such a thin region that it is referred to as a two-dimensional electron gas (2DEG). Electrons in the 2DEG do not scatter due to donor ions since the narrow bandgap material is undoped or very lightly doped. The high carrier concentration and superior transport properties result in high values of transconductance, fast switching speeds, and improved noise figure.

While the HEMT offers improvements over the MESFET for microwave applications, there are practical drawbacks to the HEMT. Heterojunctions and HEMTs present unique challenges to both microwave and semiconductor device engineers in that they are very difficult to design, fabricate, and model. To form the 2DEG, very precise control of the material growth, doping levels, and layer thickness is required. Successful fabrication of these devices also relies heavily on the control and matching of lattice constants, thermal expansion coefficients, and interface states [1]. The materials are often grown by state-of-the-art tools like metal organic chemical vapor deposition (MOCVD), atomic layer deposition (ALD), or molecular beam epitaxial growth (MBE). The device complexity results in added design and fabrication costs as well as lower yields. Additionally, the structure is inherently difficult to describe physically, making it challenging to create accurate physical models.

A drawing of a typical HEMT device layout is presented in Figure 3.3. In general, the most important physical dimension is the gate length, L. The gate length strongly affects the value of the gate-source capacitance, C_{gs}, which is of critical importance for microwave devices. For a high C_{gs}, the input impedance for the FET looks like a short-circuit and therefore is hard to match and produces no useful gain. A low value of C_{gs} is required for high frequency operation; thus, short gate lengths are desirable. Modern gate lengths of 25 nm (InP) [2], [3], [4], [5], 15 nm (GaAs) [6], and 30 nm (GaN) [7] have been reported in the literature. The gate width, Z, is also directly related to the device drain current handling. With more device width, more cross-sectional area is available for drain current. For high power applications, a large gate width is required. Conversely, for low-noise, low-current applications, small gate widths are beneficial. Bias points for devices are often given in terms of current per unit gate width or total device periphery in the case of devices with multiple gate fingers.

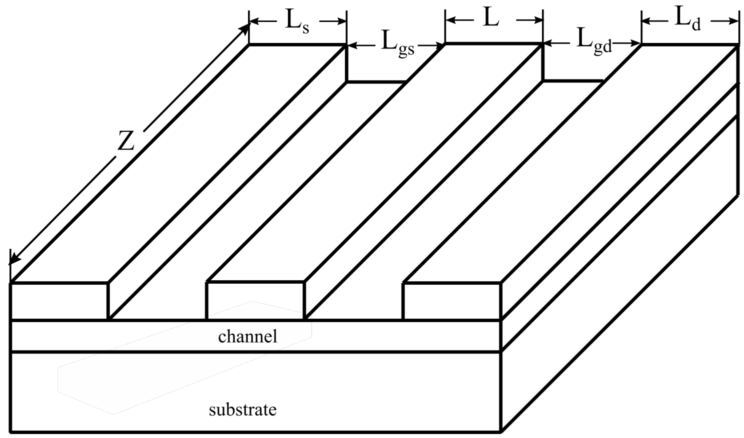

Figure 3.3: Basic HEMT cross-section with key dimensions.

3.1.1. HEMT Small-Signal Model

A small-signal model is essentially a linear RF equivalent circuit for a non-linear device. It is a limited but very useful abstraction for modeling and circuit design. While only valid for one bias point, a small-signal model obeys the principles of superposition and can be mathematically represented by simple linear expressions.

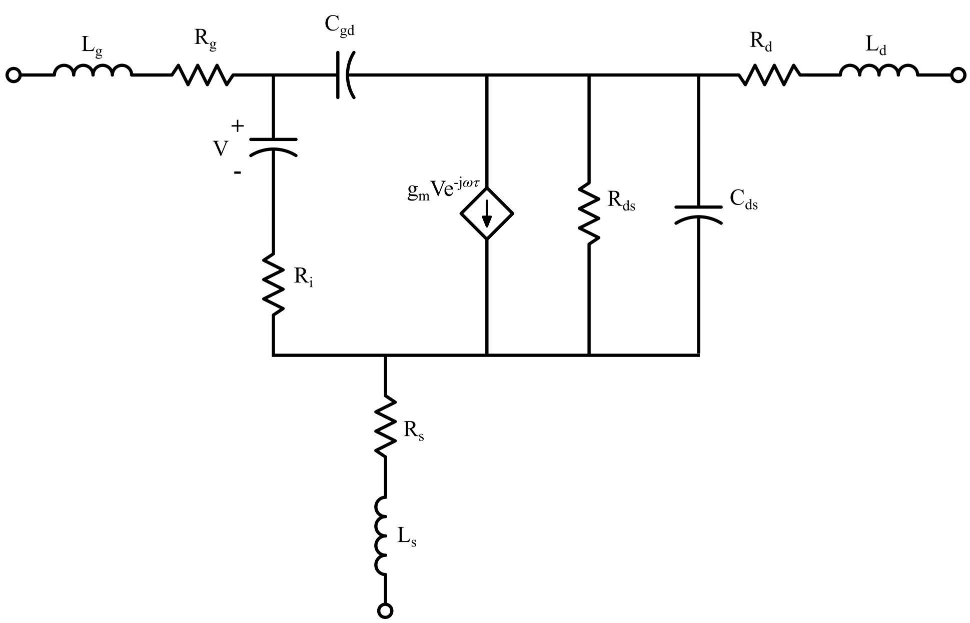

Figure 3.4: Minimal small-signal intrinsic HEMT model with extrinsic electrode elements.

A very simple schematic of a typical field effect transistor is given in Figure 3.4. In a common-source amplifier for example, the core element for amplification is the dependent current source. The current is related to the voltage across C_{gs} by the transistor's transconductance ($g_m = I_{ds}/V_{gs}$). There is a delay, τ, associated with the transconductance as well. This is also called the transit time and is one of the limiting factors for the maximum frequency of operation.

The physical origin of resistive elements and inductive elements are conceptually straightforward. The capacitive elements are slightly more complex. The gate is engineered to be capacitively coupled to the channel region of the device. When forward conduction begins and channel inversion occurs, the area covered by the gate metal over channel region form a capacitor approximated as a simple parallel plate capacitor. This capacitively couples the gate to both the drain and source regions. This is the physical origin for C_{gs} and C_{gd}. C_{ds} is a capacitance formed from the source and drain electrodes across the channel region. Unlike C_{gs} and C_{gd}, C_{ds} is not considered to be bias-dependent. The capacitances of C_{gs} and C_{gd} do depend on the DC bias point and the device's current-voltage relaionship. The physical significance of R_i is questionable and is mainly used to match S_{11}. The small-signal model of fig. 3.4 is superimposed upon a physical layout in fig. 3.5.

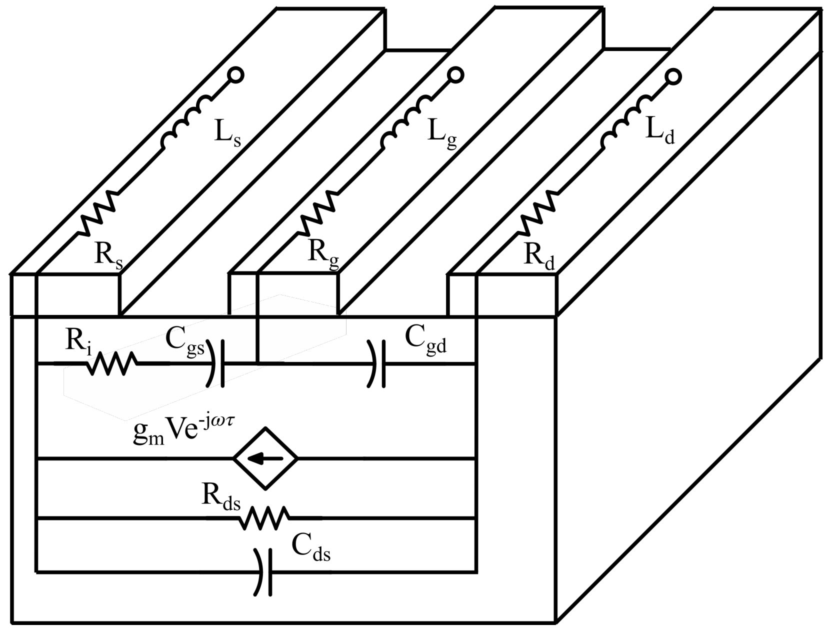

Figure 3.5: Cross-sectional physical diagram with small-signal model elements added.

Expressions for the Extraction of Intrinsic Model Elements

In order to develop a small-signal model for a particular device technology, measurements of those devices along with parameter extractions must be performed. This section reports the standard parameter extraction expressions reported by Hughes and Tasker for HEMTs [8]. Golio in his book, [1], succinctly summarizes these extractions. Scattering parameters, which are often the actual measured quantities, can be converted to impedance parameters with the following equations:

$$Z_{11} = \frac{(1 + S_{11})(1 - S_{22}) + S_{12}S_{21}}{\Delta} \tag{3.1}$$

$$Z_{12} = \frac{2S_{12}}{\Delta} \tag{3.2}$$

$$Z_{21} = \frac{2S_{21}}{\Delta} \tag{3.3}$$

$$Z_{22} = \frac{(1 - S_{11})(1 + S_{22}) + S_{12}S_{21}}{\Delta} \tag{3.4}$$

$$\Delta = (1 - S_{11})(1 - S_{22}) - S_{12}S_{21} \tag{3.5}$$

The parasitic resistances can be removed from these extrinsic z-parameters using these expressions:

$$z_{11} = Z_{11} - (R_g + R_s) \tag{3.6}$$

$$z_{12} = Z_{12} - R_s \tag{3.7}$$

$$z_{21} = Z_{21} - R_s \tag{3.8}$$

$$z_{22} = Z_{22} - (R_d + R_s) \tag{3.9}$$

The parasitic inductances L_g, L_s, and L_d can be extracted by examining the expressions for R_g, R_s, and R_d over frequency. At sufficiently high frequency, the resistance extraction will have a positive slope. That slope is proportional to the inductance values. Admittance parameters are used to extract the other elements.

$$y_{11} = \frac{z_{22}}{|z|Z_0} \tag{3.10}$$

$$y_{12} = -\frac{z_{12}}{|z|Z_0} \tag{3.11}$$

$$y_{21} = -\frac{z_{21}}{|z|Z_0} \tag{3.12}$$

$$y_{22} = \frac{z_{11}}{|z|Z_0} \tag{3.13}$$

$$|z| = z_{11}z_{22} - z_{12}z_{21} \tag{3.14}$$

From [1], the analytical form of the y-parameters are

$$y_{11} = \frac{R_i C_{gs}^2 \omega^2}{D} \tag{3.15}$$

$$y_{12} = -j\omega C_{gd} \tag{3.16}$$

$$y_{21} = \frac{g_m e^{-j\omega\tau}}{1 + jR_i C_{gs}\omega} - j\omega C_{gd} \tag{3.17}$$

$$y_{22} = g_{ds} + j\omega(C_{ds} + C_{gd}) \tag{3.18}$$

$$D = 1 + \omega^2 C_{gs}^2 R_i^2 \tag{3.19}$$

Low-Frequency Extraction Expressions

If the measurement frequency is sufficiently low, $(\omega C_{gs} R_i)^2 << 1$ and D is therefore $\approxeq 1$. The expressions above can be simplified. The extraction expressions valid at low frequency are summarized below:

$$C_{gd} = -\frac{\Im\{y_{12}\}}{\omega} \tag{3.20}$$

$$C_{ds} = \frac{\Im\{y_{22}\}}{\omega} - C_{gd} \tag{3.21}$$

$$C_{gs} = \frac{\Im\{y_{11}\}}{\omega} - C_{gd} \tag{3.22}$$

$$g_{ds} = \Re\{y_{22}\} \tag{3.23}$$

$$g_m = \Re\{y_{21}\} \tag{3.24}$$

High-Frequency Extraction of R_i, τ, and g_m

The extractions at higher frequency are more complicated. The distributed effects and parasitics of the small-signal circuit elements start to appear. The expressions for R_i and τ as well as the high-frequency expressions for g_m (from [1]) are given below:

$$R_i = \frac{1 - \sqrt{\frac{4\Re\{y_{11}\}^2}{\omega^2 C_{gs}^2}}}{2\Re\{y_{11}\}} \tag{3.25}$$

$$\tau = -\frac{1}{\omega}\tan^{-1}\left(\frac{g_{mi}}{g_{mr}}\right) \tag{3.26}$$

$$g_m e^{-j\omega\tau} = g_{mr} + j g_{mi} \tag{3.27}$$

where

$$g_{mr} = \Re\{y_{21}\} - \Im\{y_{21}\} R_i C_{gs}\omega - \omega^2 C_{gd} C_{gs} R_i \tag{3.28}$$

$$g_{mi} = \Re\{y_{21}\} R_i C_{gs}\omega + \Im\{y_{21}\} + \omega C_{gd} \tag{3.29}$$

3.1.2. Noise Models

While the sources and statistical behavior of electrical noise can vary, noise is present in all circuits and systems. Electrical noise manifests as random fluctuations in signal phase, amplitude, and spectral content which all degrade system performance. Often in microwave and terahertz electronics in particular, noise is a major limiting factor in system operation. The noise level in part determines the minimum detectable signal power, so it is advantageous to optimize for low noise. In applications such as radio astronomy and atmospheric sensing, the signal power levels are so weak that receivers need to be cryogenically cooled in order to lower the overall system noise temperature and increase sensitivity [9].

Accurately modeling the noise properties of microwave HEMTs is difficult and has been a major subject of research for several decades. Different empirical or semi-empirical models [10]–[14] and physical models [15], [16] have been reported and used to characterize and predict microwave HEMT noise properties. The goal of all these models is to extract the noise parameters for a particular device to design and optimize for low-noise circuits.

The most comprehensive HEMT noise model was introduced by Pucel [15]. The Pucel model, shown in Figure 3.6, is a physical model that consists of a noiseless FET with equivalent noise voltage and current generators. This representation is particularly valuable as it is derived from the physical noise generation processes within the FET. There are two main sources of noise: thermal fluctuations (voltage sources) and carriers traveling in the drain at their saturated velocities (diffusion noise). The thermal and diffusion noise processes are uncorrelated; however, the gate and drain current fluctuations are interdependent. Fluctuations at the gate are capacitively coupled to the channel region and appear at the device output. A correlation coefficient, C, relates the current sources i_g and i_d. The device noise parameters are computed from a set of closed form expressions and the extracted small-signal equivalent model. While this model is significantly more complex than other empirical models, it has been shown to comprehensively predict the dependence of noise parameters on device geometry, material properties, and bias conditions.

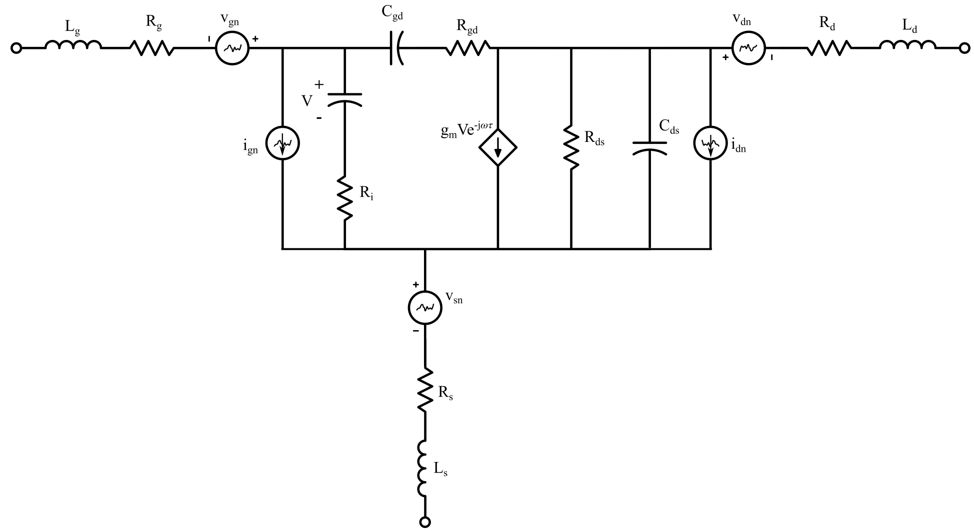

Figure 3.6: Pucel noise model showing uncorrelated voltage noise sources and correlated drain and gate current noise sources [23].

Pospieszalski published an elegant physical method in 1989 [16] for modeling the noise behavior of HEMTs. In contrast to the Pucel method, the Pospieszalski method develops closed-form expressions for the noise parameters of a FET using only the elements of a small-signal equivalent model and two frequency independent parameters: the equivalent gate and drain temperatures. Pospieszalski provides experimental evidence to suggest that the device noise can be captured by assigning two noise-equivalent temperatures to the gate and drain resistances, T_g and T_d. In measuring the devices at different temperatures and extracting the values of T_g and T_d, it was shown that unlike T_d, T_g scales with ambient temperature. This suggests that the noise generated by the gate is entirely thermal in origin. The drain temperature does not scale proportionally with the ambient temperature, which suggests this noise is primarily dominated by a shot noise current source in the drain. This method has been widely adopted by the HEMT community and provides a convenient and effective means of modeling a device's noise parameters over a large frequency range with a frequency-limited noise parameter measurement.

3.2. State-of-the-Art InP Process

The first HEMT ever made [18] was a GaAs-based device, and over four decades later it is still the most mature and dominant material choice for microwave HEMTs. More recently researchers have been developing HEMT processes for GaN and InP. GaN is typically the material of choice for high-frequency high-power amplifiers due to its excellent mobility, thermal properties, and high breakdown voltage. InP, however, has become the leading technology for THz applications. Like GaAs, InP has excellent electron mobility; however, the large conduction band discontinuity between the AlAs and InGaAs channel promotes higher 2DEG concentrations and leads to reduced parasitics, improved gain and lower noise figure when compared to AlGaAs/GaAs based devices [19], [20].

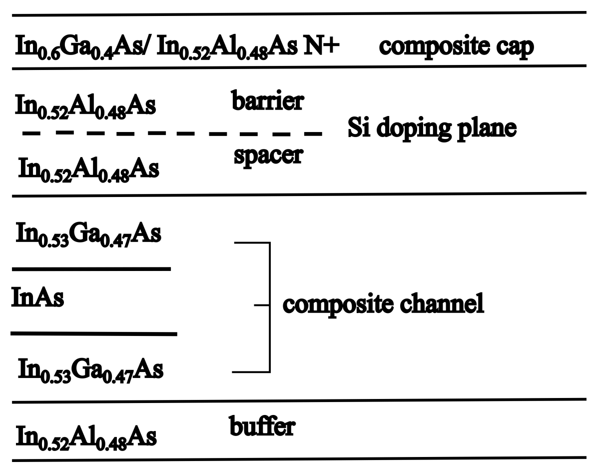

Figure 3.7: NGC InP epi stackup [23].

Northrop Grumman Space Systems has been at the forefront of InP HEMT development for many years, demonstrating amplification past the sub-millimeter wave threshold in 2007 [21], 670 GHz in 2011 [22], 850 GHz in 2014 [2], and the first successful demonstration of amplification past 1 THz [3], which was recognized by Guinness World Records in 2014 as the world's fastest integrated circuit amplifier. The epi stack-up [23] for these transistors is included in Figure 3.7. The transistor stack-up is grown via MBE on semi-insulating InP (100).

For amplification at 1 THz and above, reducing the device transit time, τ, and the gate-source capacitance is critical. Scaling the gate length down is the most important mechanism for this as well as scaling the overall device size to reduce parasitics and create a device with exceptionally high f_{MAX}. The maximum frequency of operation, f_{MAX}, is a useful figure of merit that describes the frequency at which the maximum available gain of the transistor is unity. With a gate length of 25nm, Deal et al. [2] report the Northrop Grumman InP HEMT technology to have an f_{MAX}, of around 1.4 THz. Deal et al. also demonstrated a 670 GHz LNA with less than 10 dB of fully packaged noise figure [4] with the same 25nm technology.

While the scaling of HEMTs has benefits in high-frequency operation, there is a limit to the improvements in noise figure. As reported in [24], the noise generated in the drain can be thought of as a suppressed shot noise source. The shot noise suppression factor in these devices is primarily a function of the gate and channel length. The small region near the source where carriers travel by diffusion is the primary shot noise generator. The superior transport properties in the rest of the channel, create the shot noise suppressive effects; therefore, as gate lengths scale smaller the shot noise suppression factor rapidly approaches unity since that small diffusion region of the channel starts to become a larger portion of the total channel.

3.3. Device Measurements and Parameter Extractions

Measurements above W-band for device modeling are very uncommon. These measurements usually require additional banded equipment that extends the operating frequencies of signal sources and receivers. This adds measurement complexity and acquisition time. The broadband measurement system used in this work removes this issue. High-frequency parameter extractions are difficult as many of the simple expressions reported in section 3.1.1 break down. The small-signal model is ultimately an approximation, and at high frequencies the distributive effects of the device's physical geometry and other parasitics start to take effect and even dominate the performance of the device. However, the effects of some of the extrinsic elements (R_g, R_s, R_d, L_g, L_s, and L_d) are shown in this section to be more evident at high frequency. As the Northrop Grumman InP HEMT technology is used for THz applications, the models are extracted at low frequency and extrapolated multiple decades. High-frequency parameter extractions can aid in the ultimate accuracy of these models.

3.3.1. MMIC Mounting

The devices and LNA's measured in this work were diced chips from a larger wafer. In order to measure them, a mounting process had to be developed to mechanically secure them and provide DC bias to the amplifiers. The bias for the single devices was applied through an integrated bias-tee in the on-wafer probes. The full stack-up is shown in fig. 3.9.

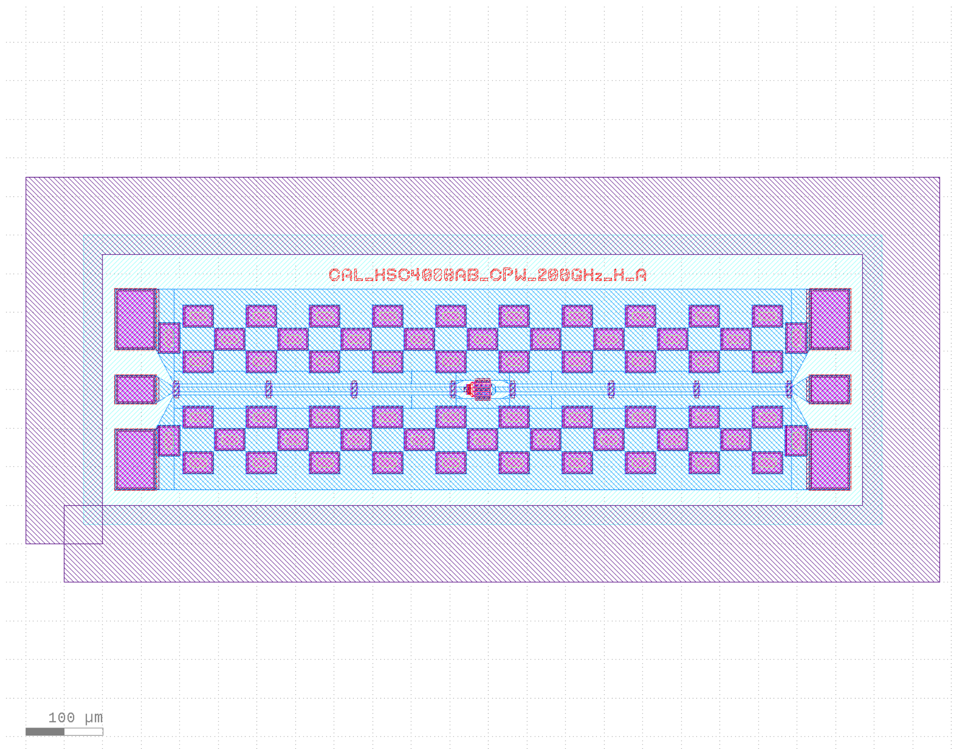

Figure 3.8: Example of a device embedded in 50Ω grounded CPW transmission lines.

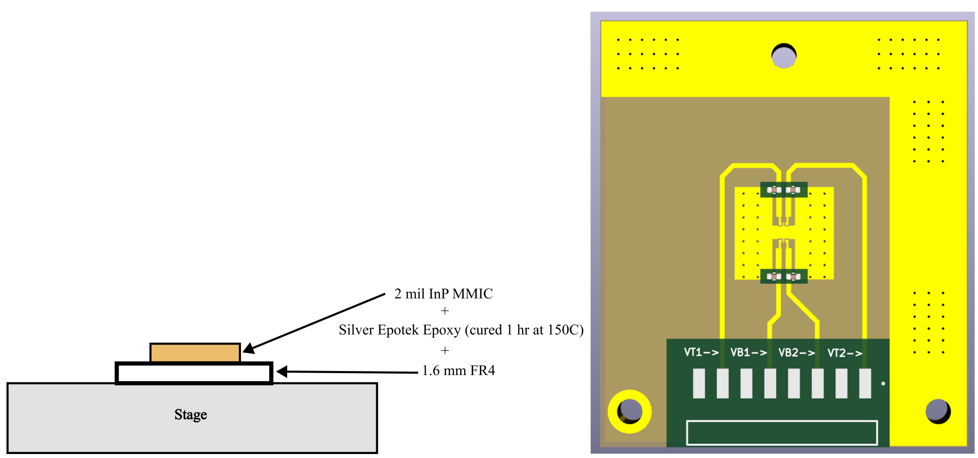

Figure 3.9: MMIC mounting stackup for these measurements as well as the measurements in Chapter 4.

A simple gold-finished FR-4 PCB was designed for the rough dimensions of the MMICs. Epotek H20E silver conductive epoxy was used to fix the chips to the exposed gold pad on the PCB. This also served the ground connection for the chips. 100fF 0402 bypass capacitors were soldered on each bias line. Custom free-standing gold beams (beamleads) were patterned and plated to connect the DC bias pads on the chips to the PCB pads. An unthreaded wire-bonder was used to contact weld the gold beamlead connections.

3.3.2. Device De-embedding

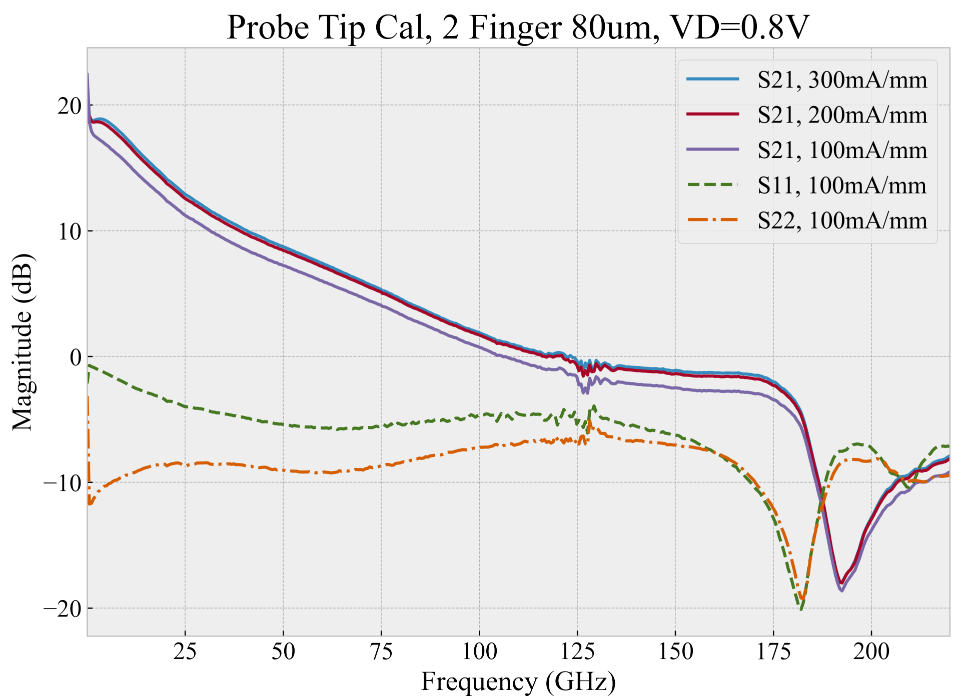

Figure 3.10: Example measured S-parameters of a two finger 80 μm periphery transistor.

An example of measured s-parameters for the two-finger 80μm are shown in Figure 3.10. A standard TRL calibration was performed, which set the reference plane at the probe tips. The measurement noise in the region around 130 GHz is a result of the cross-over effects in the diplexer-based broadband probes. An unforeseen issue in the measurements of these devices is evident in the measurement of the InP calibration thru structure (fig. 3.11). In order to de-embed the device measurements correctly, diced calibration structures from the same wafer were mounted and measured. Due to the electrically small dimensions of the diced chips, a strong resonance was measured at around 180 GHz. The effects of this resonance was seen in all of the measurements; however, since the positioning of the transmission lines on each chip were slightly different, the behavior was not exactly the same for every device. This significantly complicated performing the second-tier calibration.

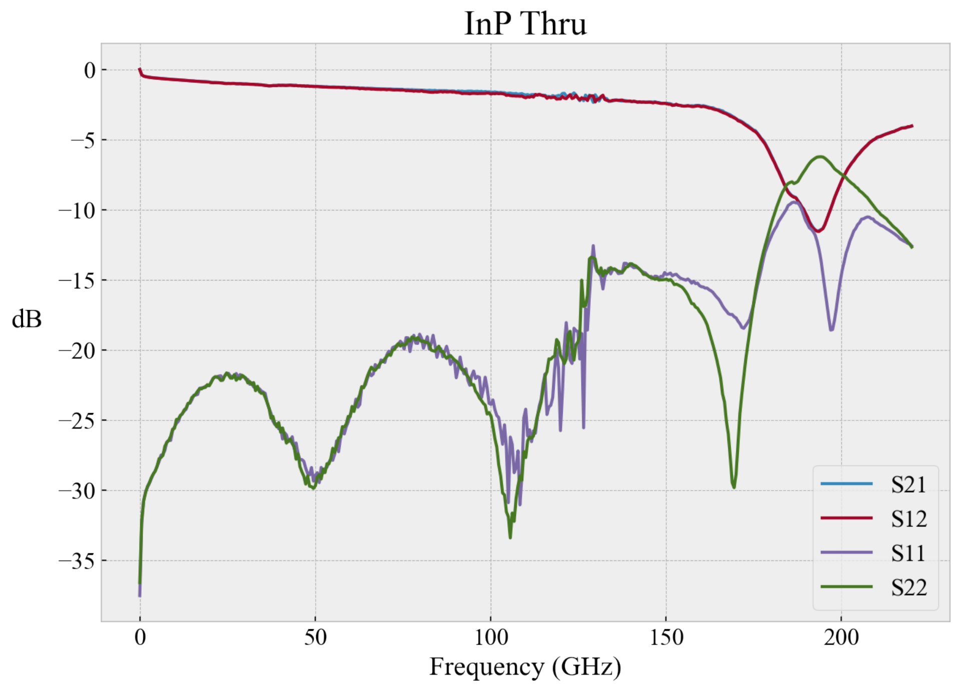

Figure 3.11: Measured scattering parameters for the diced InP thru.

A full InP calibration kit was measured. Several calibration procedures were attempted; however, the simplest and highest quality results using these standards was 2X-Thru de-embedding method [25]. Unfortunately, even this method showed unphysical characteristics above 180 GHz. For this reason, the following method was used to de-embed the measurements to the device reference plane.

Figures 3.12 and 3.13 show the measured phase and loss difference between the measured thru structure and line structure. The line is 224μm longer than the thru. Using these measurements, a CPWG equivalent model was used in ADS to de-embed the device measurements. The effects of the high-frequency resonance can be seen in the measured results above 180 GHz.

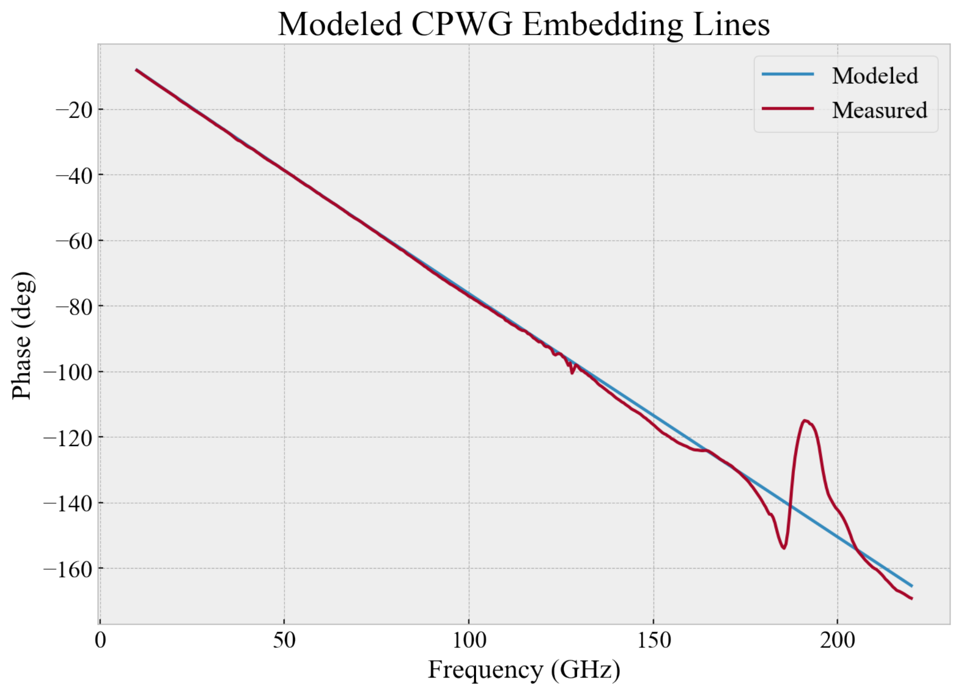

Figure 3.12: Comparison of the modeled CPWG structure phase with the measured difference in phase between the line and thru structures.

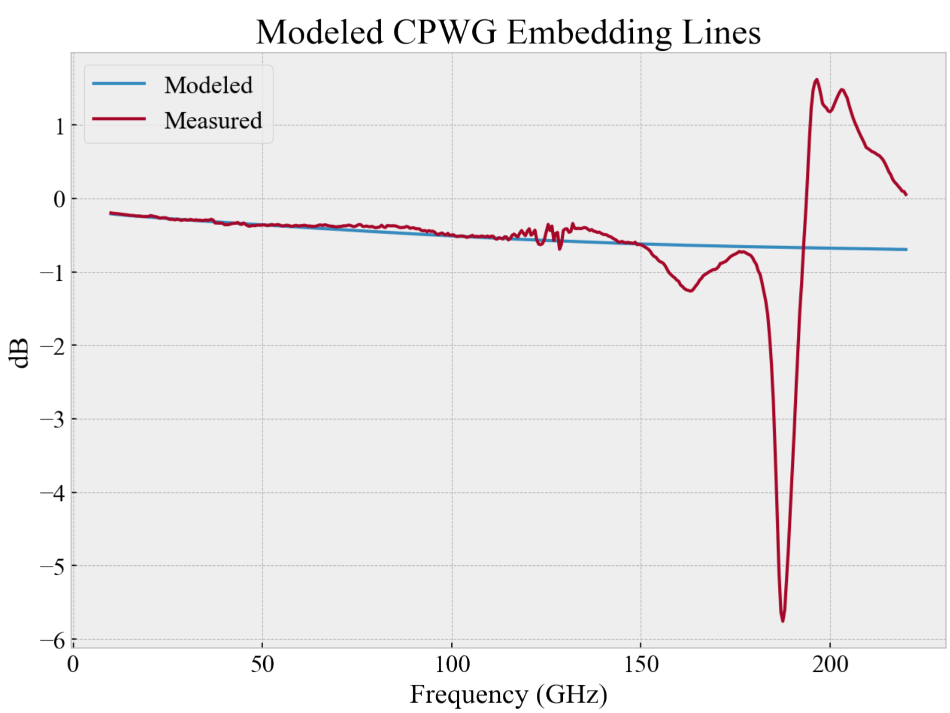

Figure 3.13: Comparison of the modeled CPWG structure loss with the measured difference in loss between the line and thru structures.

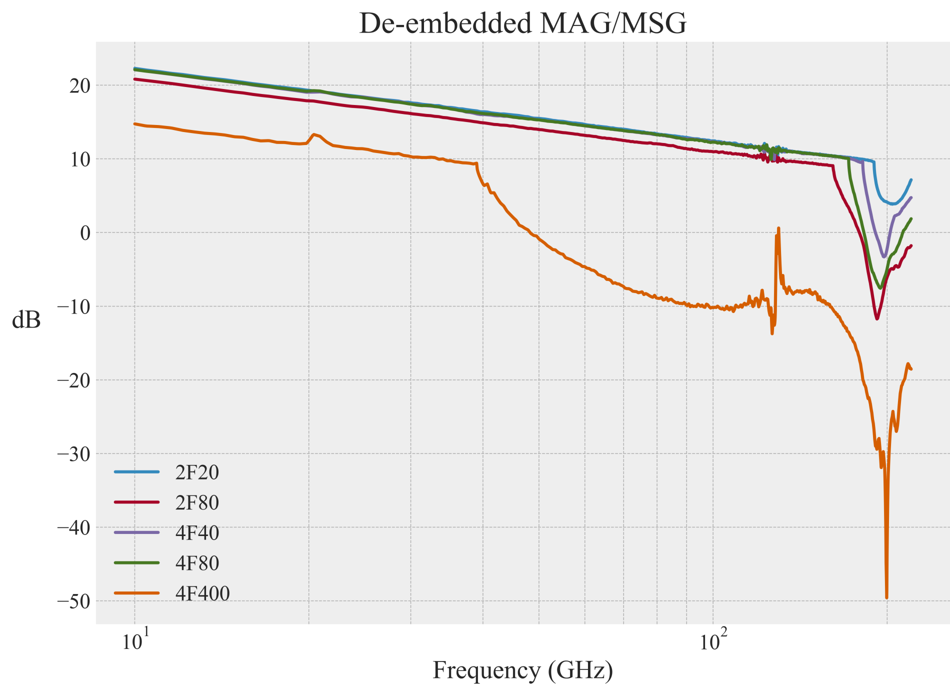

Figure 3.14: De-embedded maximum available gain / maximum stable gain for five different device sizes.

The de-embedded maximum available gain and maximum stable gain is shown in Figure 3.14. This is calculated as

$$G_{MAX} = \left|\frac{S_{21}}{S_{12}}\right|(K - \sqrt{K^2 - 1}) \tag{3.30}$$

where K is the stability factor. If the device is unstable ($K < 1$), G_{MAX} is calculated as the maximum stable gain:

$$G_{MAX} = \left|\frac{S_{21}}{S_{12}}\right| \tag{3.31}$$

Clearly the large device size of the four-finger 400μm makes it unsuitable for high frequency operation.

3.3.3. Y-Parameter Extractions and Modeling of Results

Using the expressions outlined in section 3.1.1, a small-signal model was developed using the broadband data. Data was taken for 9 total bias points; however, a bias point of 0.9V drain voltage and 300 mA/mm drain current density was chosen for the parameter extractions.

Table 3.1: Summary of Extracted Values for the NGC 35nm InP HEMT

Element	Value
C_{gs} (fF/mm)	525
C_{gd} (fF/mm)	249
C_{ds} (fF/mm)	380
g_m (mS/mm)	2100
f_T (GHz)	400
R_{gs} (mΩ·mm)	0.08
R_{ds} (mΩ·mm)	7.2
R_g (mΩ·mm)	0.072
L_g (pH/mm)	169

The parameter extractions are plotted against the developed model in Figures 3.15 - 3.19. Close agreement was achieved up to 80 GHz in most cases.

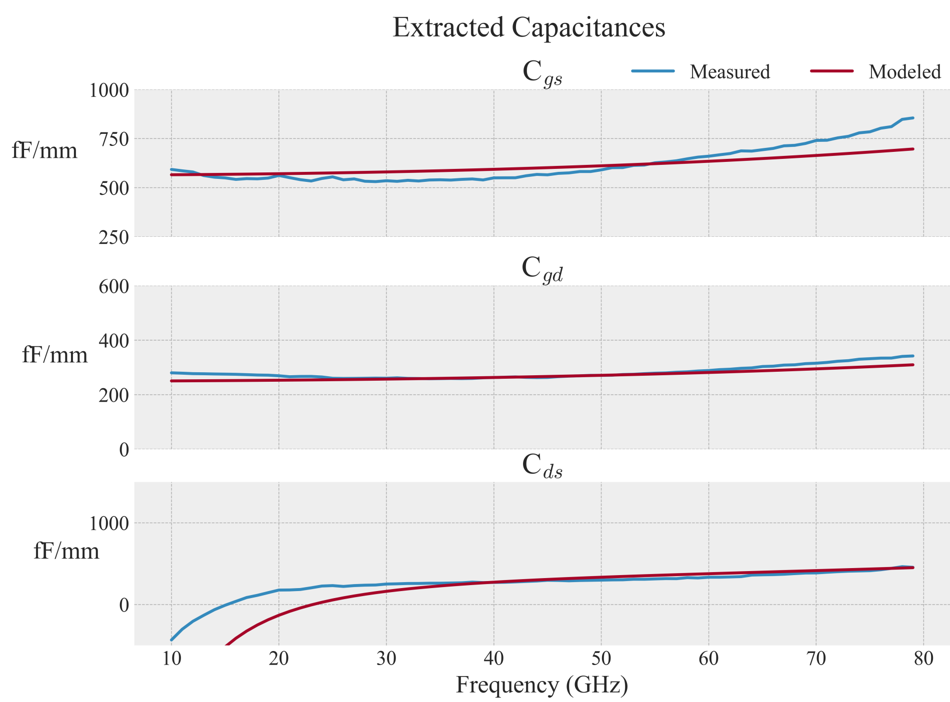

Figure 3.15: Modeled vs. measured for the extracted model capacitances.

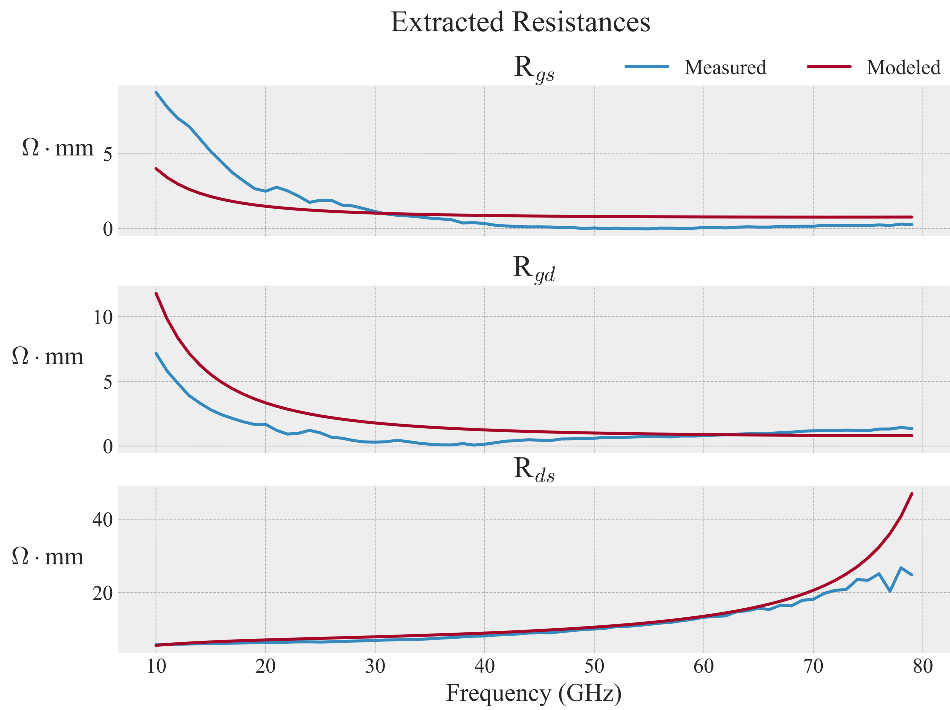

Figure 3.16: Modeled vs. measured for the extracted model resistances.

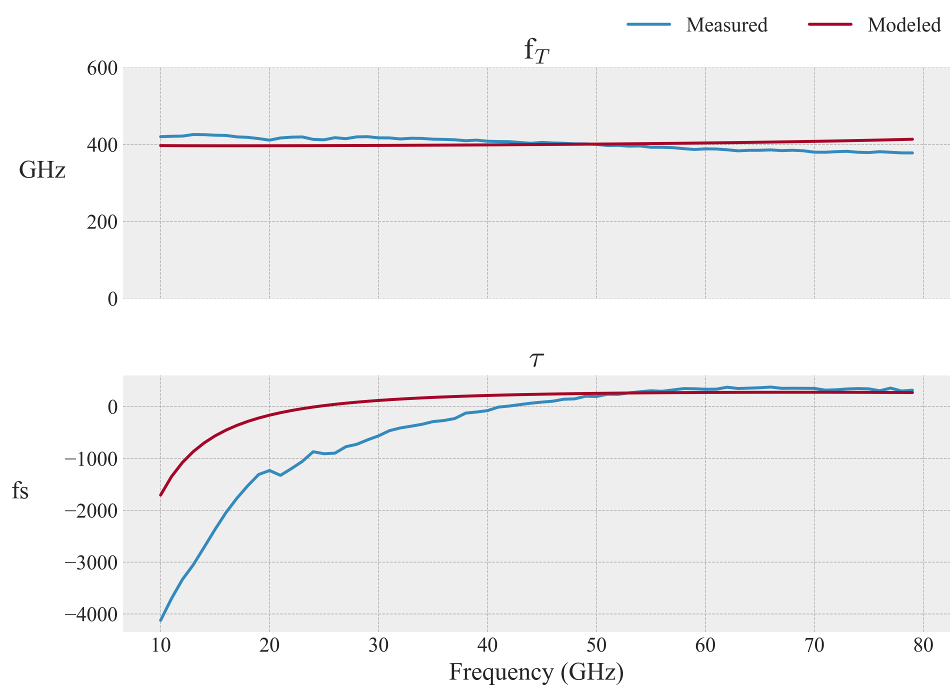

Figure 3.17: Modeled vs. measured for the extracted model transition frequency, and transit time.

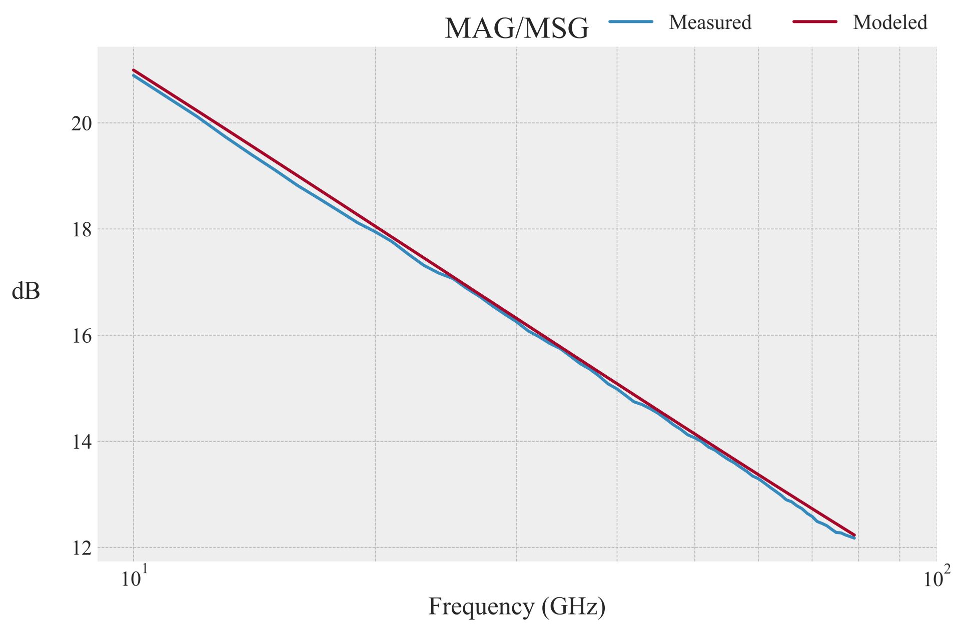

Figure 3.18: Modeled vs. measured for the extracted model maximum stable gain for a two finger 80μm periphery device at 0.9V, 300mA/mm.

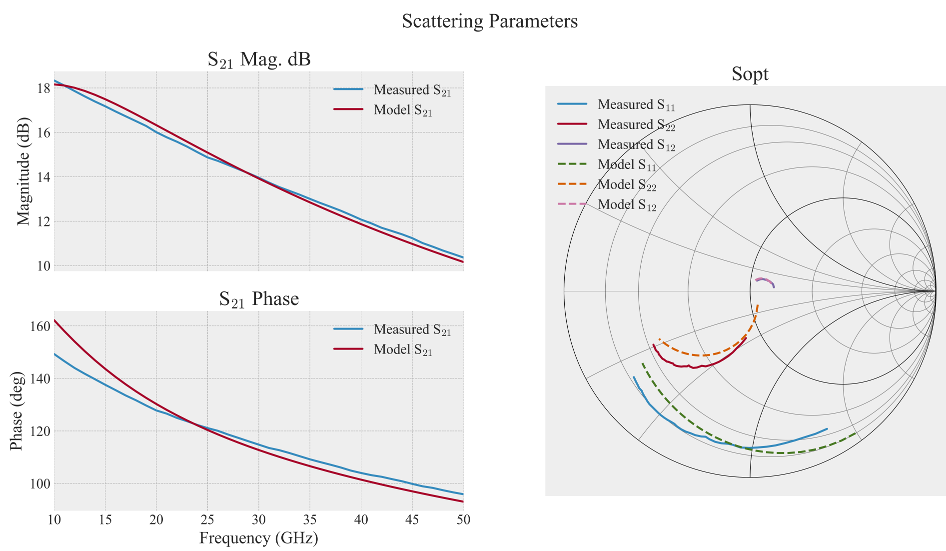

Figure 3.19: Modeled vs. measured for the two finger 80μm periphery device at 0.9V, 300mA/mm.

3.3.4. High-Frequency Extraction Information

The following section highlights some of the extraction results at high frequency. This data is useful for more closely modeling the effects of the extrinsic elements R_g, R_d, R_s, L_g, L_d, and L_s. The effects of these elements often do not appear at low frequency, especially for devices with short gate lengths.

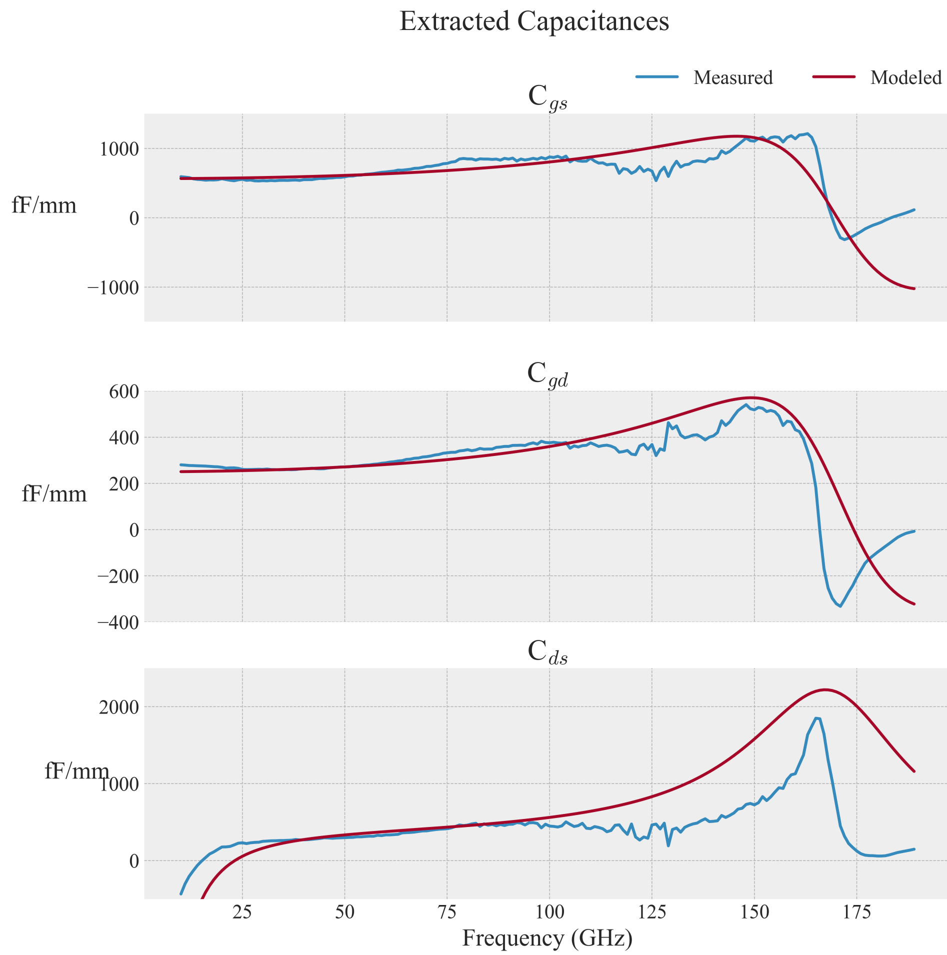

Figure 3.20: Modeled and measured capacitances at higher frequency. The position in frequency of the large discontinuity is tuned by extrinsic resistances and inductances.

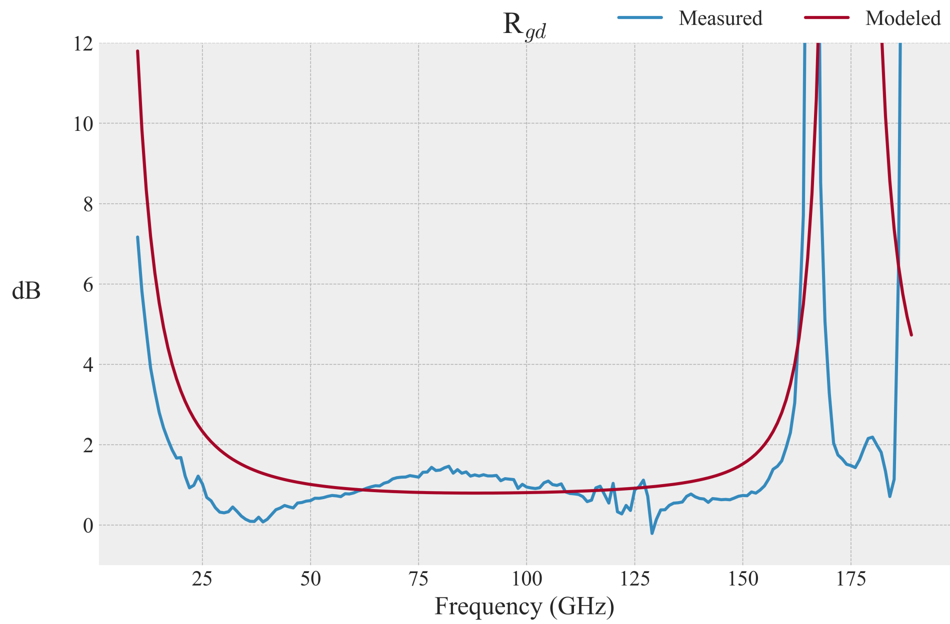

Figure 3.21: Modeled and measured R_{gd} at high frequency. The location of the discontinuity is dominated by the value of L_g.

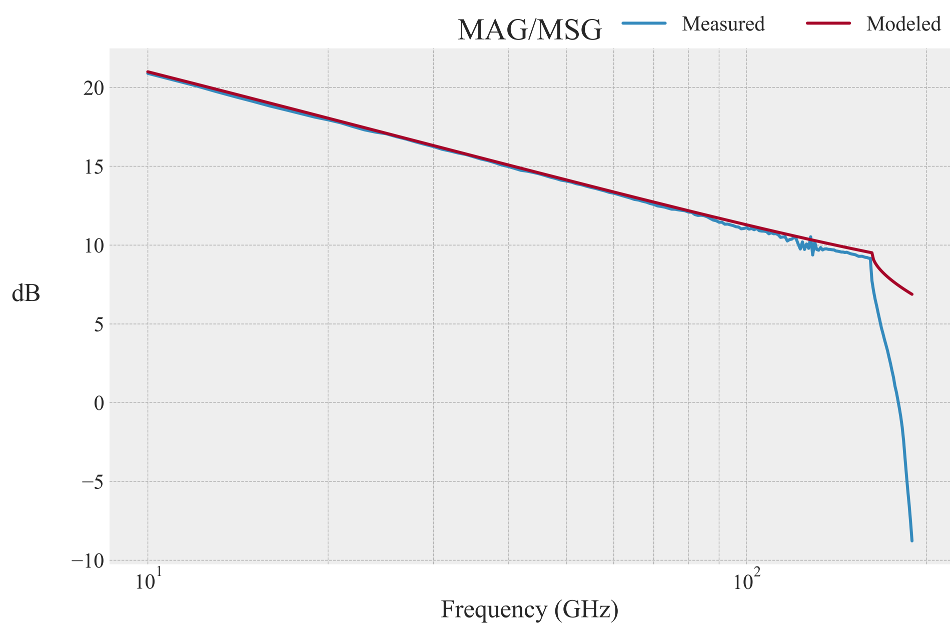

Figure 3.22: Modeled and measured MAG/MSG at high frequency.

In general, a modest increase in the parasitic resistances was required; however, a significant increase in gate inductance was required to match the capacitive transitions and the extracted gate-drain resistance at high frequency. The notch in MAG/MSG was heavily impacted by the parasitic resistances. In the lower frequency extractions, all of these elements had very little consequence in the extracted values.

3.4. Design and Measurement of MMIC LNAs for Atmospheric Science

The role of the low noise amplifier (LNA) is very important in receiver designs of any kind. When evaluating the total noise figure of a chain of cascaded components, the overall noise characteristics are described by the Friis equation [27]:

$$F_{tot} = F_1 + \frac{F_2 - 1}{G_1} + \frac{F_3 - 1}{G_1 G_2} + \cdots + \frac{F_i - 1}{G_1 G_2 \cdots G_{i-1}} \tag{3.32}$$

The LNA is usually the first component in the receiver chain because eq. 3.32 shows that the noise figure of each successive component in the chain is divided by the gain of the prior components. In other words, the total noise figure is dominated by the first component in the chain. An amplifier optimized for noise performance (LNA) with high gain is the best choice for the first stage of a receiver chain; however, the noise figure alone is not the best metric to use when choosing or designing and LNA. The noise measure, M, is a better figure of merit because it normalizes an amplifier's noise figure with the amplifier's gain. The noise measure is given below:

$$M = \frac{F - 1}{1 - \frac{1}{G}} \tag{3.33}$$

From the Friis equation, it is evident that a first stage amplifier with low noise factor, F_1, and low gain, G_1, may yield an higher overall impact to the system noise figure than an amplifier with higher F_1 and higher G_1. Therefore, taking the amplifier's gain into consideration is critical for minimizing the total system noise figure.

3.4.1. MMIC LNA Architecture and Design

The design of an LNA can be relatively straightforward, but the trade-offs often lead to complicated design decisions. For the best noise performance, the amplifier must be presented with the optimal source reflection coefficient, Γ_{opt}. This usually does not coincide with the optimal small-signal power match. Designing for the best simultaneous noise and power match is important for a well-designed LNA. The output impedance should be designed for the best power match; however, changing the impedance at the load of the amplifier will change Γ_{opt} at the source and vice-versa. For this reason, LNA design is often an iterative process.

Using the Northrop Grumman 35 nm and 25 nm processes, several LNAs have been designed for frequencies from W-band to WR-4. The designs target atmospheric windows at 94 GHz, 140 GHz, and 239 GHz (25nm design) as well as the O_2 spectral line at 118 GHz. Each LNA is a three-stage common source microstrip MMIC design with matching and decoupling networks as shown in Figure 3.23. The matching networks are a simple single-stub tuners. MIM capacitors (600 pF/mm^2) are included for bias network decoupling, and 100 Ω/sq thin-film resistors are used for setting the drain currents. A single 20 Ω/sq resistor is placed at the output for stability and improved output power matching. The gate terminal for the first stage is isolated from the other terminals for separate tuning since it has the largest effect on the overall amplifier noise performance. This architecture is described in detail in [26].

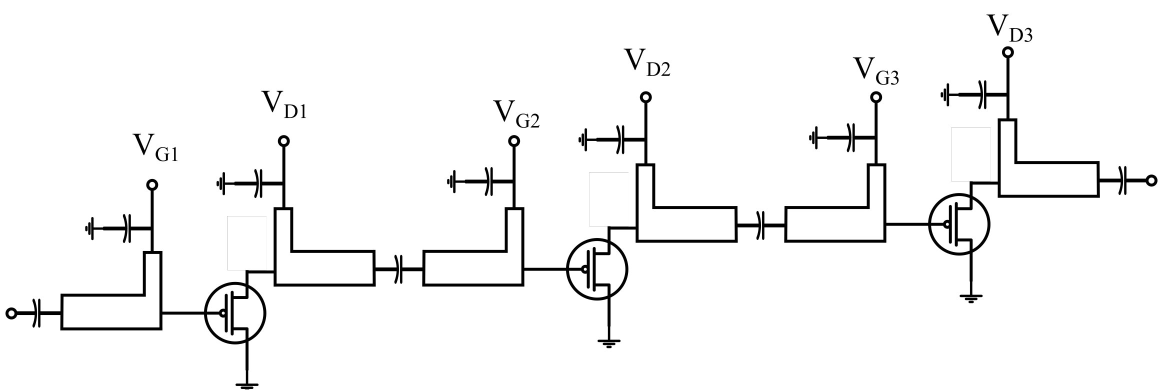

Figure 3.23: High-level schematic and layout of a 140GHz 35nm three-stage InP HEMT LNA.

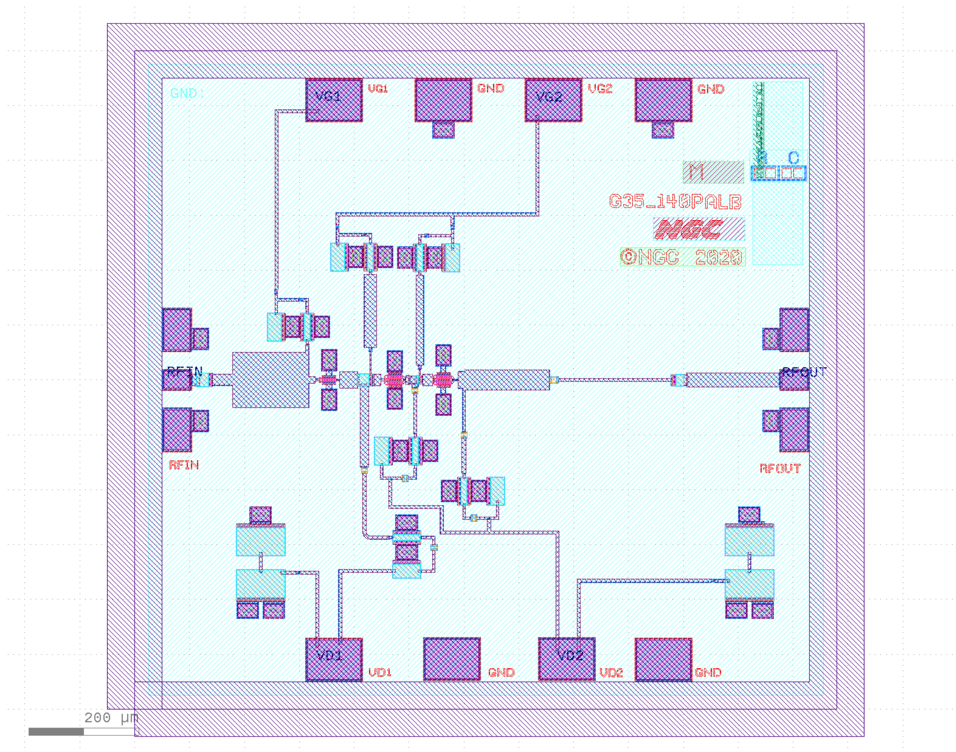

Figure 3.24: Cadence layout of the 140 GHz LNA. The chip dimensions are 1.28mm x 1mm.

The design process was the same for each amplifier. An appropriate device periphery was chosen as the first step in each design. The overall size of the device has a large effect on the gain and minimum noise figure. The small-signal device models were implemented in Keysight's Advanced Design System (ADS). The models were created using s-parameter measurements and the parameter extraction methods described in Section 3.3.3. Noise measurements below 100 GHz were used together with the Pospieszalski modeling technique to extrapolate the noise parameters of the device to higher frequencies. A rough circuit level simulation was developed and optimized for at least 20 GHz of bandwidth, 15 dB of return loss, 15-20 dB gain, and 2-3 dB noise figure in band. From there, electromagnetic (EM) models of all the matching networks, vias, and capacitors were created and parameterized in ADS Momentum. The EM models were then optimized for performance and gain flatness from source to load and iterated.

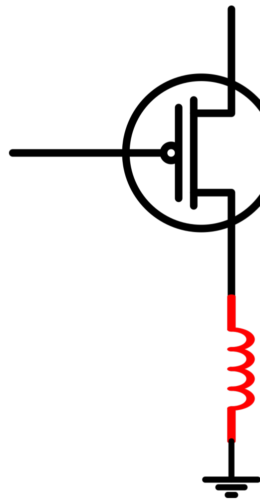

Figure 3.25: Schematic showing source degeneration with added source inductance.

Source degeneration was used to improve the simultaneous noise and power match. By adding a small amount of inductance at the source of each device, the input reflection coefficient needed for minimum noise figure can be shifted towards the optimal reflection coefficient needed for a small-signal power match.

Broadband Scattering Parameter Measurements

Selected measurement results for the 35nm LNA designs are presented below. The modeled bias point of 0.8V, 100mA/mm was plotted against the simulated data as well. All three amplifiers show close agreement with the simulated data; however, the gain responses were more narrowband.

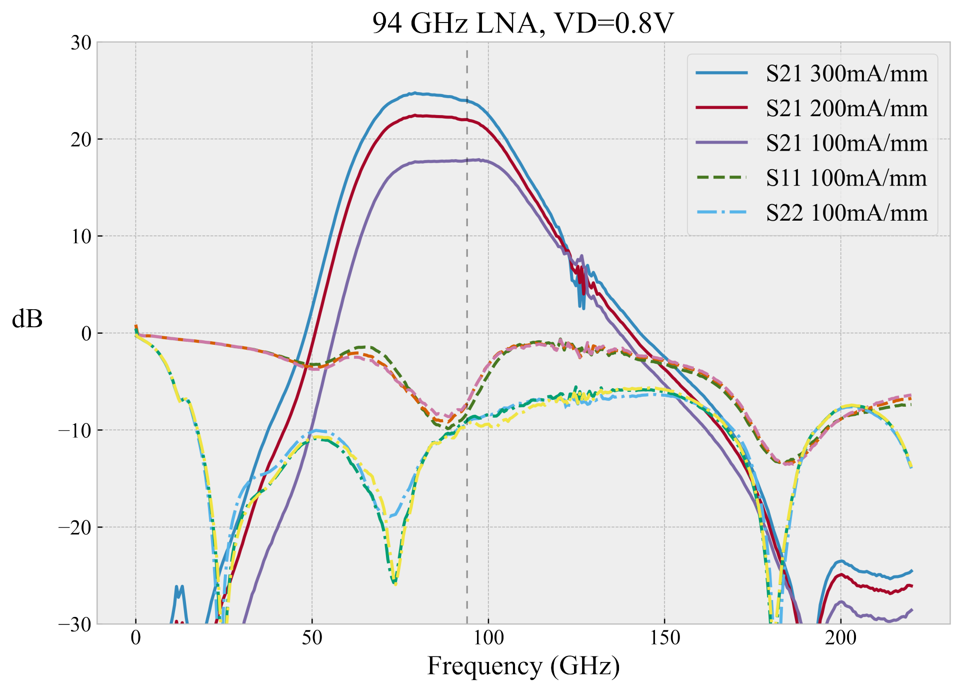

Figure 3.26: S-Parameter measurements vs. drain current for the 94GHz LNA design.

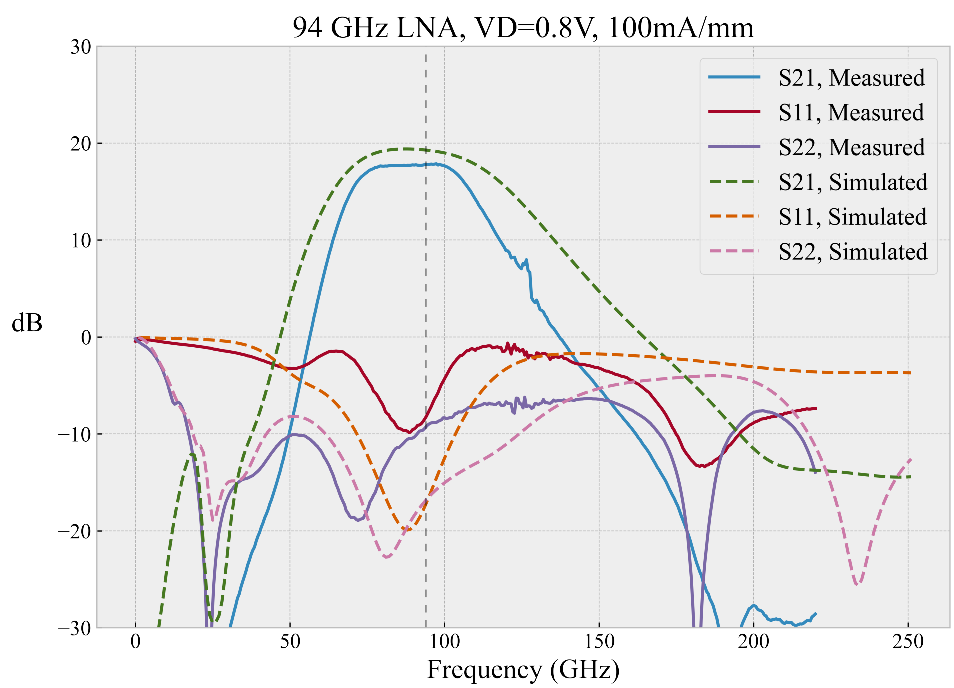

Figure 3.27: Comparison of simulated and measured data for 0.8V, 100mA/mm bias point.

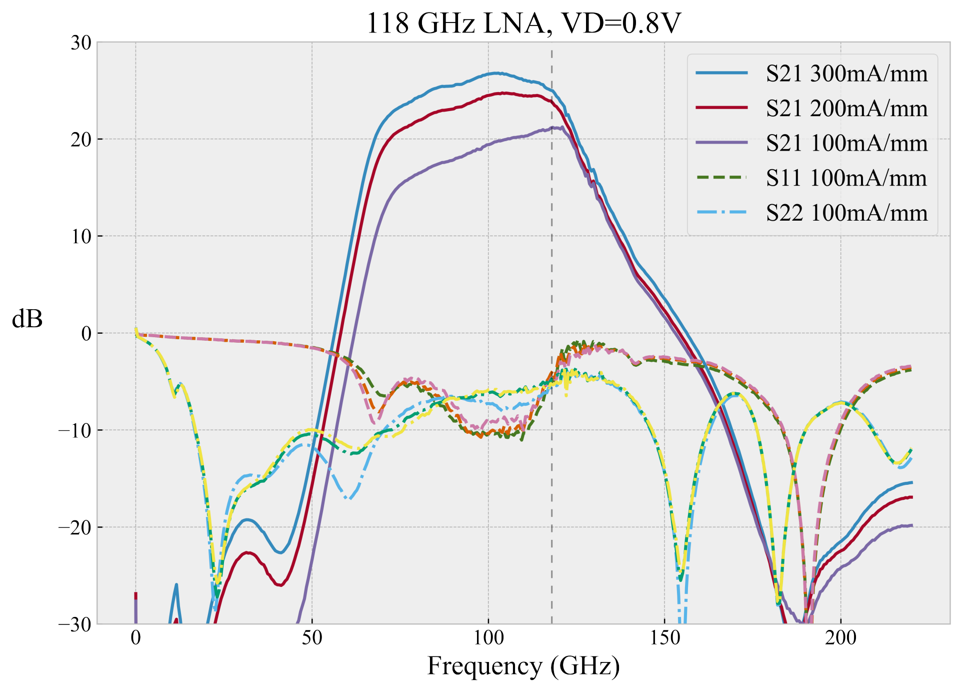

Figure 3.28: S-Parameter measurements vs. drain current for the 118GHz LNA design.

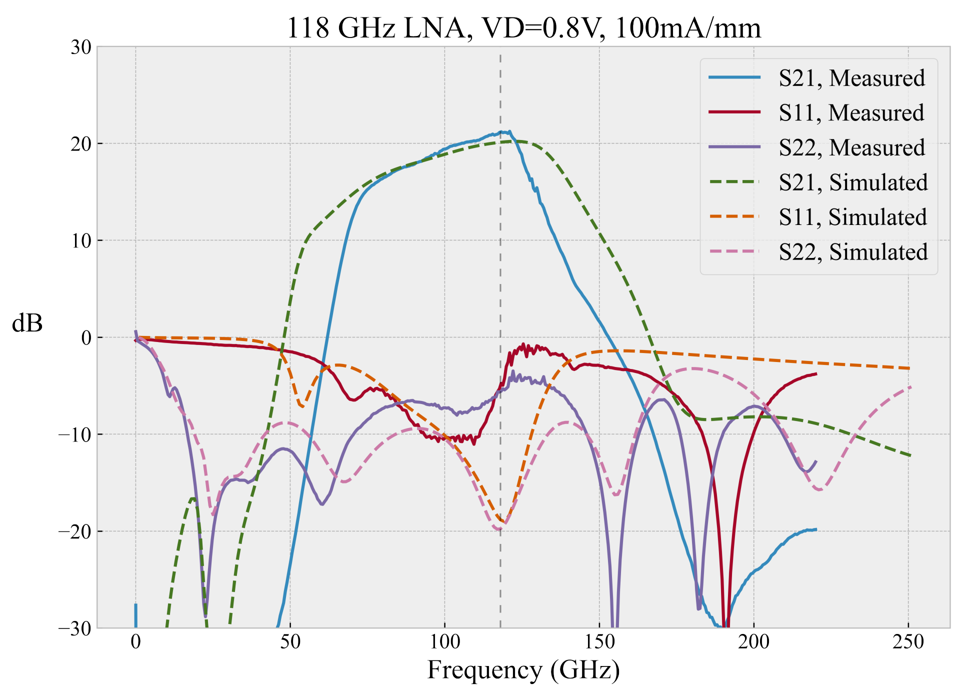

Figure 3.29: Comparison of simulated and measured data for 0.8V, 100mA/mm bias point.

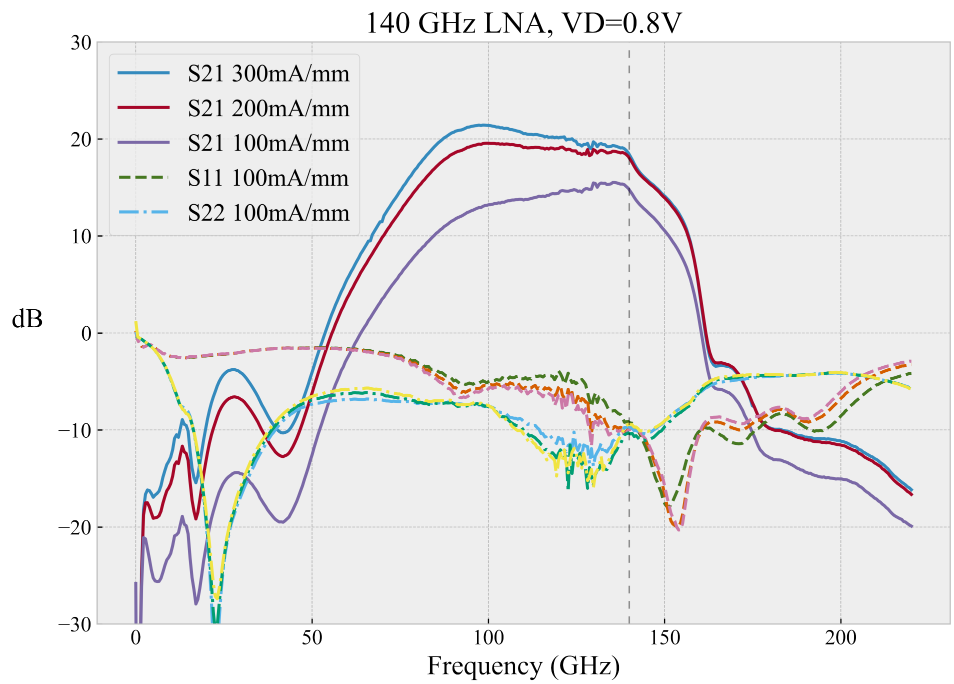

Figure 3.30: S-Parameter measurements vs. drain current for the 140GHz LNA design.

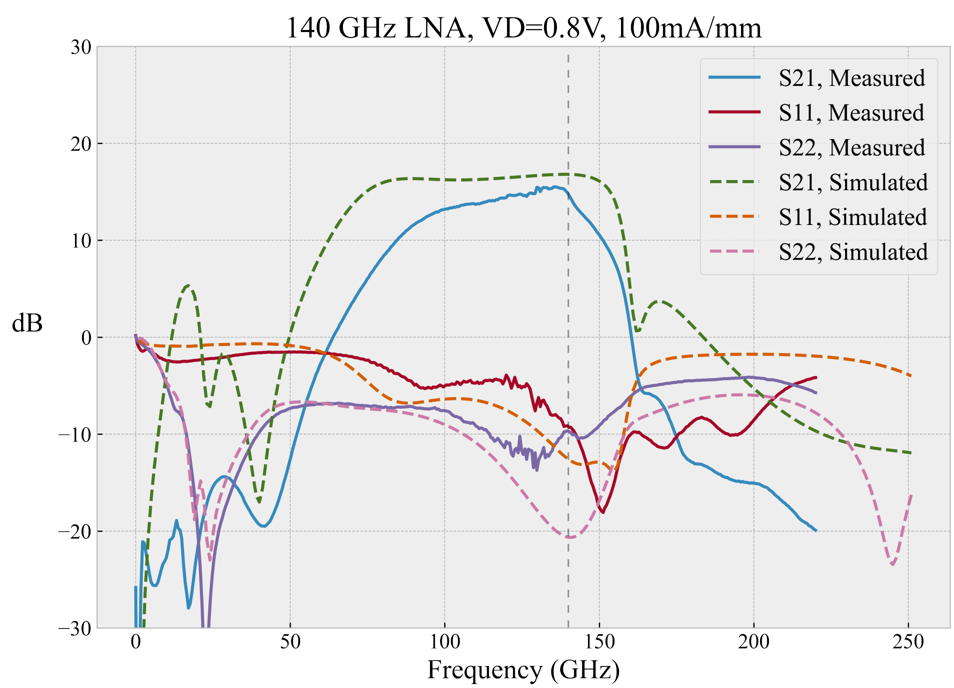

Figure 3.31: Comparison of simulated and measured data for 0.8V, 100mA/mm bias point.

In order to more closely match the measured results, the LNA simulations and device element values were tuned. The high frequency roll-off in gain was achieved by lowering the DC blocking capacitances (about 100fF in series for each capacitor). A significant increase in gate inductance that agrees with the findings from the high-frequency device extractions was required to more closely match the low frequency gain roll-off.

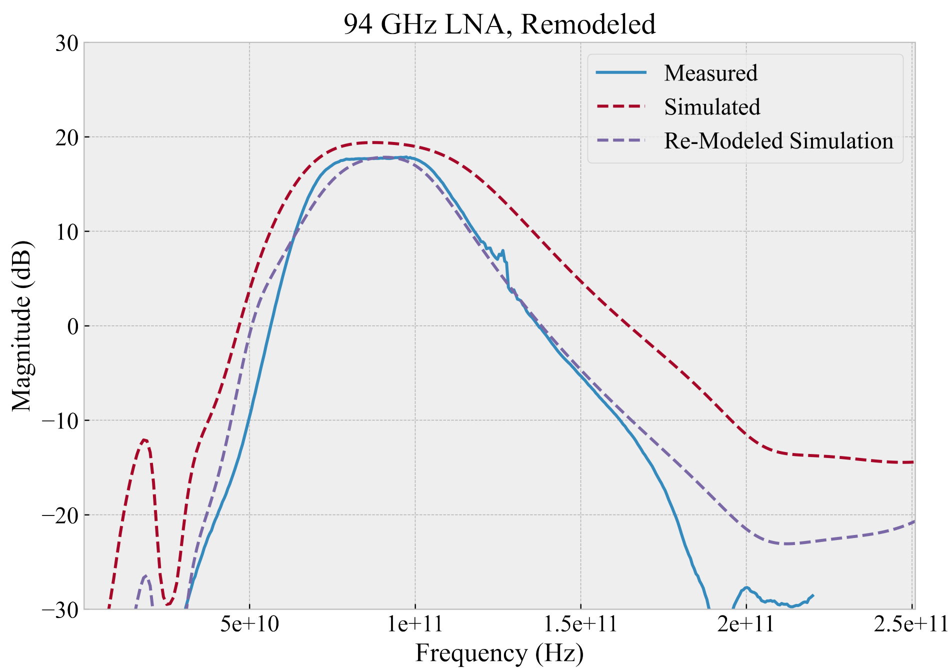

Figure 3.32: Remodeled 94GHz LNA dB(S21) comparison.

Table 3.2: Remodeled Element Values

Element	**Original**	**Re-modeled**
L_g (pH/mm)	0	800
C_{gs} (fF/mm)	537	670
g_m (mS/mm)	1633	1500
$R_g (m\Omega \cdot mm)$	20	41

3.5. Conclusion

This chapter describes the broadband (DC-220GHz) scattering parameter measurements of Northrop Grumman's 35nm InP HEMTs and three MMIC LNAs designed with their PDK. A successful extraction of a small-signal model was demonstrated. The accuracy of this model was improved with high-frequency extraction data. Measured results for three LNA MMICs were shown to have good agreement to the simulations; however, the differences between measured and modeled results highlighted the same parameter extraction insights achieved with the high-frequency extraction data.

Bibliography

[1] J. Michael Golio, Microwave MESFETs and HEMTs. Artech House, Inc., 1991.

[2] W. R. Deal, K. Leong, A. Zamora, V. Radisic, and X. B. Mei, “Recent progress in scaling InP HEMT TMIC technology to 850 GHz,” in 2014 IEEE MTT-S International Microwave Symposium (IMS2014), Jun. 2014, pp. 1–3. doi: 10.1109/MWSYM.2014.6848588.

[3] X. Mei et al., “First Demonstration of Amplification at 1 THz Using 25-nm InP High Electron Mobility Transistor Process,” IEEE Electron Device Lett., vol. 36, no. 4, pp. 327–329, Apr. 2015, doi: 10.1109/LED.2015.2407193.

[4] W. R. Deal et al., “A 670 GHz Low Noise Amplifier with <10 dB Packaged Noise Figure,” IEEE Microw. Wirel. Compon. Lett., vol. 26, no. 10, pp. 837–839, Oct. 2016, doi: 10.1109/LMWC.2016.2605458.

[5] K. M. K. H. Leong et al., “A 0.85 THz Low Noise Amplifier Using InP HEMT Transistors,” IEEE Microw. Wirel. Compon. Lett., vol. 25, no. 6, pp. 397–399, Jun. 2015, doi: 10.1109/LMWC.2015.2421336.

[6] S. Yeon, M. Park, J. Choi, and K. Seo, “610 GHz InAlAs/In0.75GaAs Metamorphic HEMTs with an Ultra-Short 15-nm-Gate,” in 2007 IEEE International Electron Devices Meeting, Dec. 2007, pp. 613–616. doi: 10.1109/IEDM.2007.4419014.

[7] S. Chander, Ajay, D. Nirmal, and M. Gupta, “30 nm Normally off enhancement mode AlGaN/GaN HEMT on SiC substrate for future high speed nanoscale power applications,” in 2017 International Conference on Innovations in Electrical, Electronics, Instrumentation and Media Technology (ICEEIMT), Feb. 2017, pp. 293–296. doi: 10.1109/ICIEEIMT.2017.8116852.

[8] B. Hughes and P. J. Tasker, "Bias dependence of the MODFET intrinsic model elements values at microwave frequencies," in IEEE Transactions on Electron Devices, vol. 36, no. 10, pp. 2267-2273, Oct. 1989, doi: 10.1109/16.40909.

[9] M. W. Pospieszalski, “Extremely low-noise cryogenic amplifiers for radio astronomy: past, present and future,” in 2018 22nd International Microwave and Radar Conference (MIKON), May 2018, pp. 1–6. doi: 10.23919/MIKON.2018.8514558.

[10] A. F. Podell, “A functional GaAs FET noise model,” IEEE Trans. Electron Devices, vol. 28, no. 5, pp. 511–517, May 1981, doi: 10.1109/T-ED.1981.20375.

[11] M. S. Gupta, O. Pitzalis, S. E. Rosenbaum, and P. T. Greiling, “Microwave Noise Characterization of GaAs MESFET’s: Evaluation by On-Wafer Low-Frequency Output Noise Current Measurement,” IEEE Trans. Microw. Theory Tech., vol. 35, no. 12, pp. 1208–1218, Dec. 1987, doi: 10.1109/TMTT.1987.1133839.

[12] H. Fukui, “Design of Microwave GaAs MESFET’s for Broad-Band Low-Noise Amplifiers,” IEEE Trans. Microw. Theory Tech., vol. 27, no. 7, pp. 643–650, Jul. 1979, doi: 10.1109/TMTT.1979.1129694.

[13] H. Fukui, “Optimal noise figure of microwave GaAs MESFET’s,” IEEE Trans. Electron Devices, vol. 26, no. 7, pp. 1032–1037, Jul. 1979, doi: 10.1109/T-ED.1979.19541.

[14] A. Cappy, A. Vanoverschelde, M. Schortgen, C. Versnaeyen, and G. Salmer, “Noise modeling in submicrometer-gate two-dimensional electron-gas field-effect transistors,” IEEE Trans. Electron Devices, vol. 32, no. 12, pp. 2787–2796, Dec. 1985, doi: 10.1109/T-ED.1985.22417.

[15] R. A. Pucel, H. A. Haus, and H. Statz, “Signal and Noise Properties of Gallium Arsenide Microwave Field-Effect Transistors,” in Advances in Electronics and Electron Physics, vol. 38, L. Marton, Ed. Academic Press, 1975, pp. 195–265. doi: 10.1016/S0065-2539(08)61205-6.

[16] M. W. Pospieszalski, “Modeling of noise parameters of MESFETs and MODFETs and their frequency and temperature dependence,” IEEE Trans. Microw. Theory Tech., vol. 37, no. 9, pp. 1340–1350, Sep. 1989, doi: 10.1109/22.32217.

[17] R. Yadav, P. Pathak, and R. Mehra, “Noise modeling and simulation of DCDMG AlGaN/GaN MODFET,” Int. J. Appl. Eng. Res., vol. 12, pp. 2662–2669, Jun. 2017.

[18] T. Mimura, S. Hiyamizu, T. Fujii, and K. Nanbu, “A New Field-Effect Transistor with Selectively Doped GaAs/n-Al x Ga 1- x As Heterojunctions,” Jpn. J. Appl. Phys., vol. 19, no. 5, pp. L225–L227, May 1980, doi: 10.1143/JJAP.19.L225.

[19] A. Fathimulla, J. Abrahams, T. Loughran, and H. Hier, “High-performance InAlAs/InGaAs HEMTs and MESFETs,” IEEE Electron Device Lett., vol. 9, no. 7, pp. 328–330, Jul. 1988, doi: 10.1109/55.733.

[20] K. H. G. Duh et al., “High-performance InP-based HEMT millimeter-wave low-noise amplifiers,” in IEEE MTT-S International Microwave Symposium Digest, Jun. 1989, pp. 805–808 vol.2. doi: 10.1109/MWSYM.1989.38845.

[21] W. R. Deal et al., “Demonstration of a S-MMIC LNA with 16-dB Gain at 340-GHz,” in 2007 IEEE Compound Semiconductor Integrated Circuits Symposium, Oct. 2007, pp. 1–4. doi: 10.1109/CSICS07.2007.19.

[22] W. R. Deal et al., “Low Noise Amplification at 0.67 THz Using 30 nm InP HEMTs,” IEEE Microw. Wirel. Compon. Lett., vol. 21, no. 7, pp. 368–370, Jul. 2011, doi: 10.1109/LMWC.2011.2143701.

[23] W. Deal, X. B. Mei, K. M. K. H. Leong, V. Radisic, S. Sarkozy, and R. Lai, “THz Monolithic Integrated Circuits Using InP High Electron Mobility Transistors,” IEEE Trans. Terahertz Sci. Technol., vol. 1, no. 1, pp. 25–32, Sep. 2011, doi: 10.1109/TTHZ.2011.2159539.

[24] M. W. Pospieszalski, "On the limits of noise performance of field effect transistors," 2017 IEEE MTT-S International Microwave Symposium (IMS), 2017, pp. 1953-1956, doi: 10.1109/MWSYM.2017.8059045.

[25] B. Chen, J. He, Y. Guo, S. Pan, X. Ye and J. Fan, "Multi-Ports (2^n) 2x-Thru De-

Embedding: Theory, Validation, and Mode Conversion Characterization," in IEEE Transactions on Electromagnetic Compatibility, vol. 61, no. 4, pp. 1261-1270, Aug. 2019, doi: 10.1109/TEMC.2019.2908782.

[26] M. Varonen et al., “An MMIC Low-Noise Amplifier Design Technique,” IEEE Trans. Microw. Theory Tech., vol. 64, no. 3, pp. 826–835, Mar. 2016, doi: 10.1109/TMTT.2016.2521650.

[27] H. T. Friis, "Noise Figures of Radio Receivers," in Proceedings of the IRE, vol. 32, no. 7, pp. 419-422, July 1944, doi: 10.1109/JRPROC.1944.232049.

CHAPTER 4

On-Wafer WR-5.1 Cryogenic Scattering Parameter and Noise Measurements of Active Devices

On-wafer measurements allow for efficient characterization and modeling of high-frequency devices while eliminating the need for expensive backside processing and subsequent packaging. Many millimeter and sub-millimeter wave devices are cryogenically cooled to improve their noise performance. Due to the many challenges presented at WR5.1 frequencies and cryogenic temperatures, achieving wafer-level measurements of active devices above W-band is extremely difficult.

Cryogenic on-wafer measurements and modeling of HEMTs has been reported in [41]–[46]; however, to the author's knowledge, this work is the first successful demonstration of cryogenic on-wafer WR5.1 scattering parameter and noise figure measurements of active devices. Single transistors and a three-stage monolithic microwave integrated circuit (MMIC) low-noise amplifier (LNA) from Northrop Grumman's 35nm InP HEMT process were measured. WR5.1 double-sideband and single-sideband noise figure measurement systems are presented.

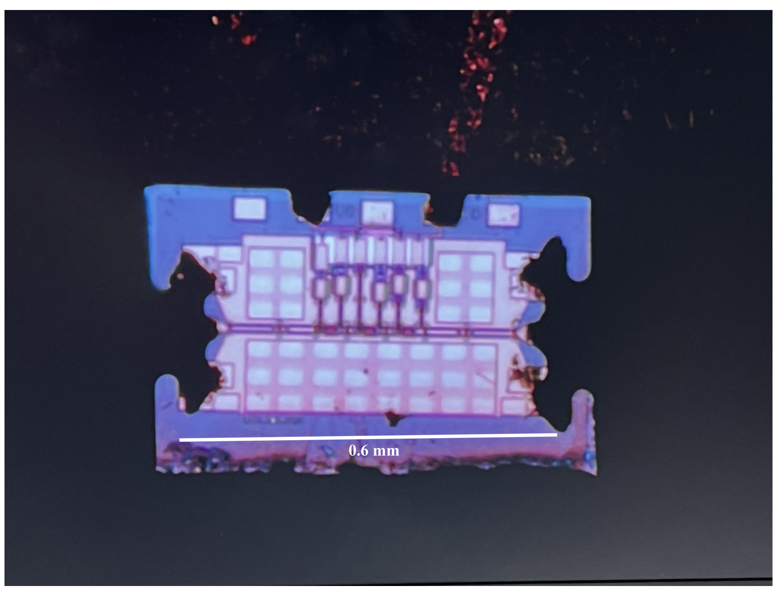

Figure 4.1: Microscope picture of the NGC LNA183 MMIC LNA measured with two DMPi WR5.1 cryoprobes.

4.1. Scattering Parameter Measurements

4.1.1. Experimental Setup

With the same cryogenic probe station described in Chapter 1, custom WR5.1 cryogenic waveguide probe arms were mounted with DMPi WR5.1 on-wafer probes. In [7], an on-wafer calibration and measurement of a passive structure was performed with these probes. Two VDI mini-VNAX (vector network analyzer extender) modules were power-calibrated and mounted onto the custom micro-manipulators. The power calibration was necessary as the InP HEMTs will saturate at an output power of around 1 mW. The incident power was calibrated to -30dBm using a VDI Erickson PM5B power meter and a Keysight PNAX.

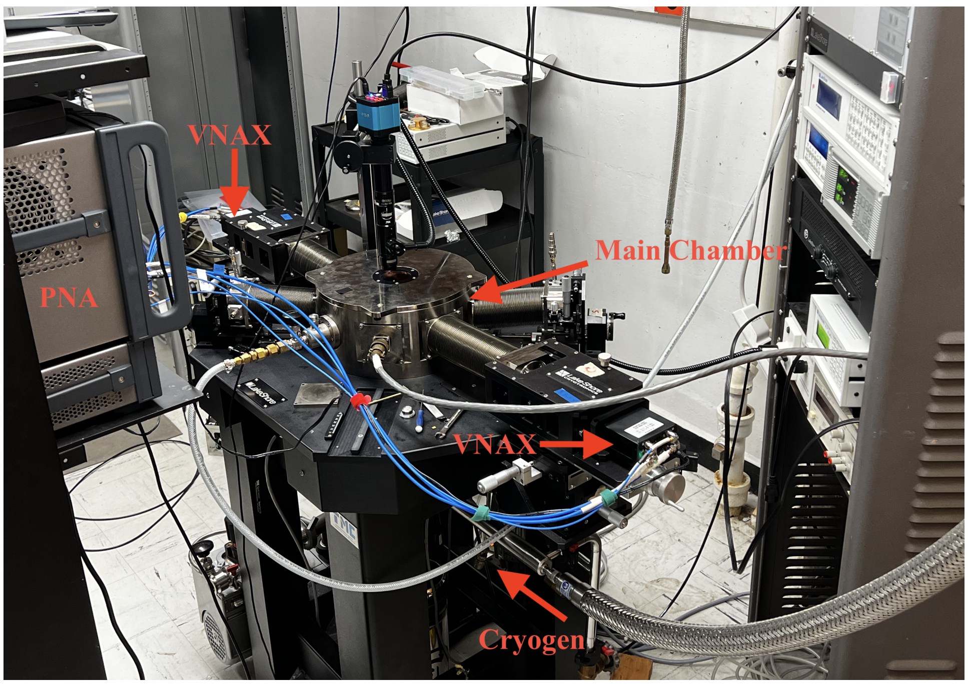

Figure 4.2: Picture of the cryogenic measurment setup. Two VDI WR5.1 mini-VNAX modules were mounted to the chamber with the custom waveguide cryo-probe assemblies.

Figure 4.3 shows the custom waveguide probe arms used in these experiments. There is an internal vacuum and thermal break as well as x, y, and z axis manipulators. There is an inner carriage for mounting a VNA extender that rotates with the entire probe arm for planarity adjustments.

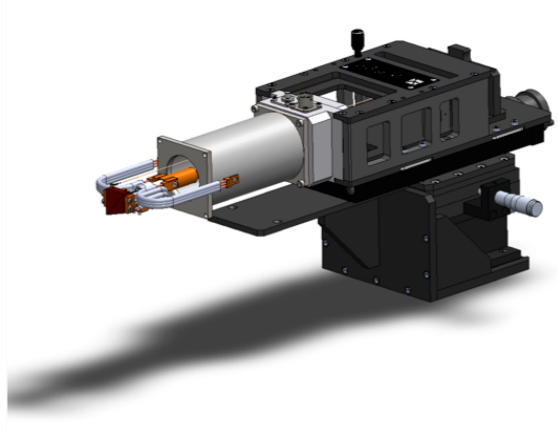

Figure 4.3: Rendering of the WR5.1 cryoprobe waveguide arm with micro-manipulators. This was designed by both Lakeshore and Swissto12.

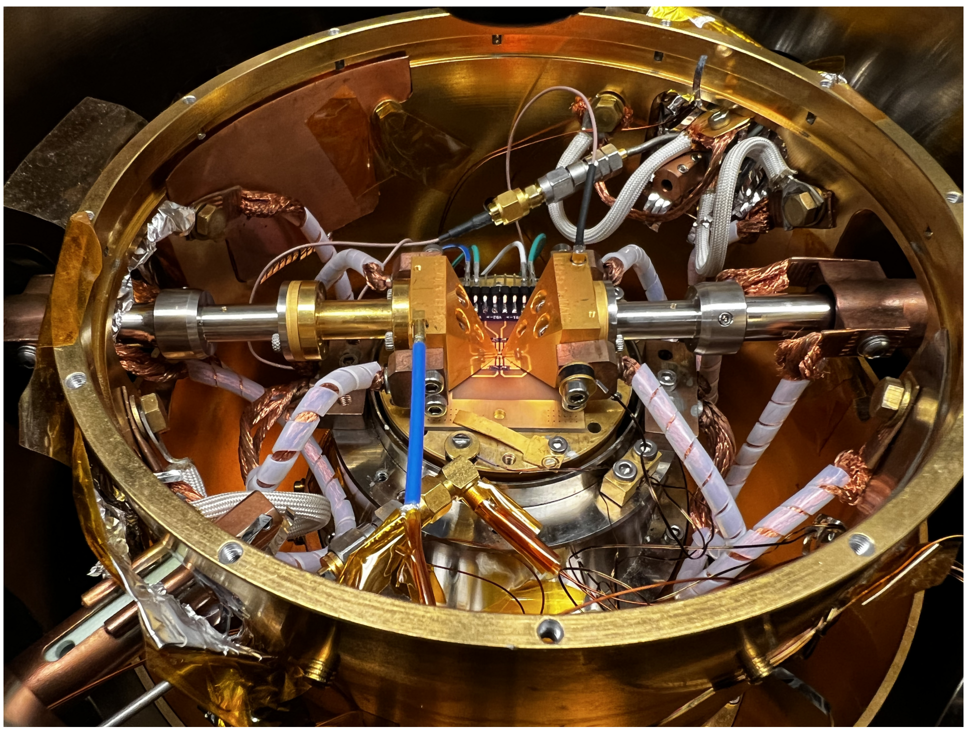

Figure 4.4: On-wafer measurement of the LNA183 InP MMIC in the FIR lab's Lakeshore CPX probestation.

A picture of a room-temperature measurement setup is shown in the figure above. DC bias can be fed through the integrated bias-tees on the probes (for single devices) or through hardwired connections through the main chamber (for integrated amplifiers).

4.1.2. Measurement Results

The scattering parameter measurements of the single devices were extremely difficult. Most of the single devices exhibited significant DC instability with large drain current fluctuations and spikes in transconductance. Similar behavior was reported in [8]. Additionally, the chip resonance detailed in Section 3.3.2 made the data above 180 GHz unreliable.

The scattering parameter measurements of the NGC LNA183 MMIC were far better. The MMIC had no observable stability issues at cryogenic temperatures. Since these measurements were power calibrated to an incident power of -30dBm, the gain of the amplifier significantly improved measurement accuracy.

The measured power gain for the LNA183 is shown in fig. 4.5 for room temperature and around 80K. A substantial increase in gain was observed, which is expected with decreasing temperature.

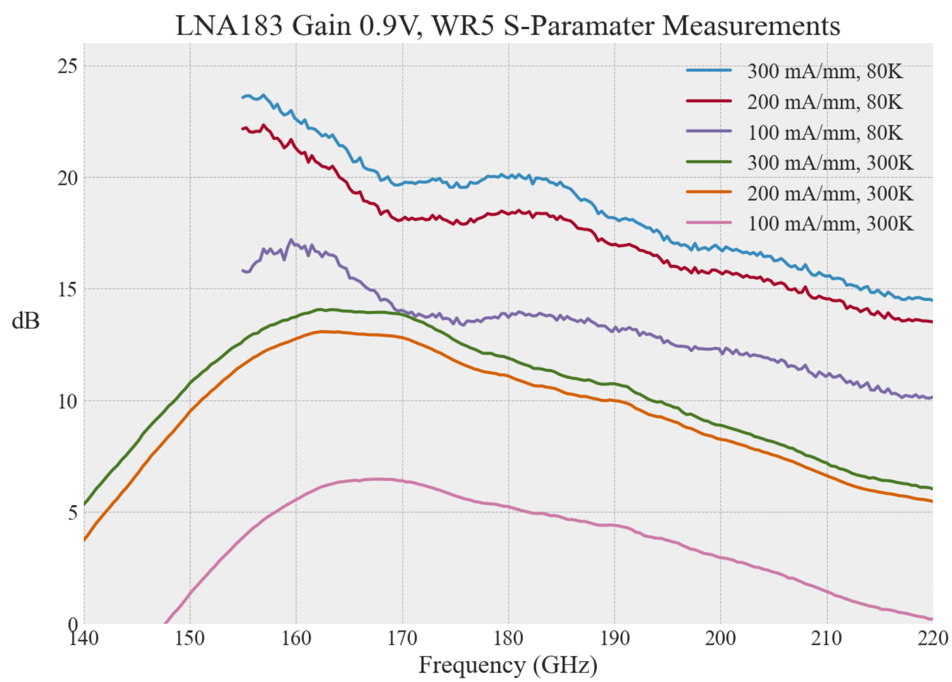

Figure 4.5: Measured power gain of the NGC LNA183 at room temperature and about 80K.

The measured power gain of the two-finger 20μm device and the four-finger 400μm device are given in fig. 4.6 and 4.7 respectively. Again, the overall measurement quality of the single devices suffered due to the observed DC instability. Additionally, these devices are embedded in simple 50Ω transmission lines and not impedance-matched. As a result, these devices exhibit very low power gain and even significant loss at WR-5.1 frequencies.

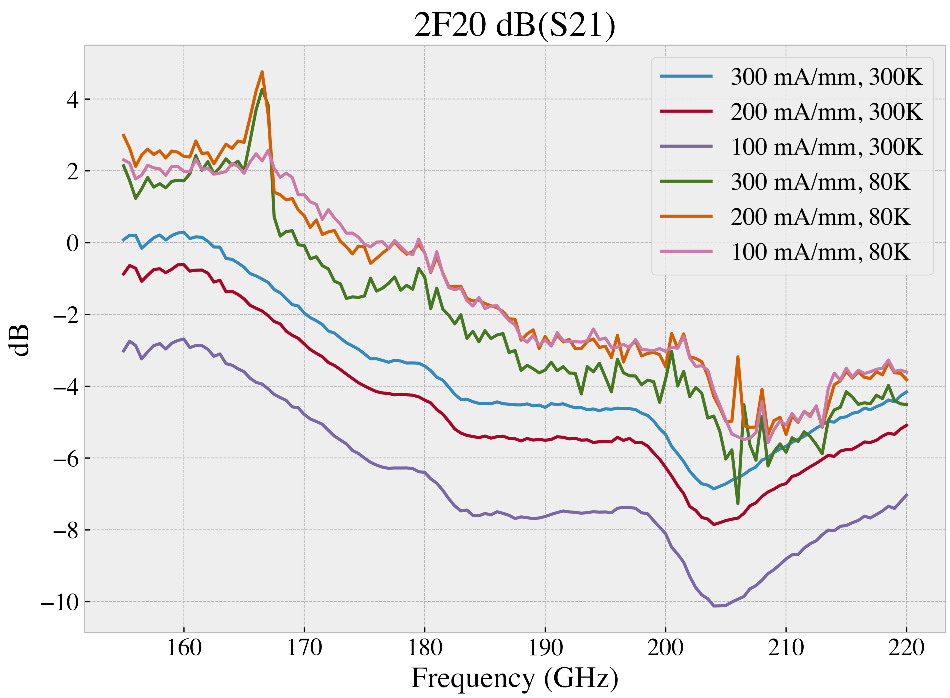

Figure 4.6: Measured power gain of a two-finger 20μm periphery device at room temperature and 80K.

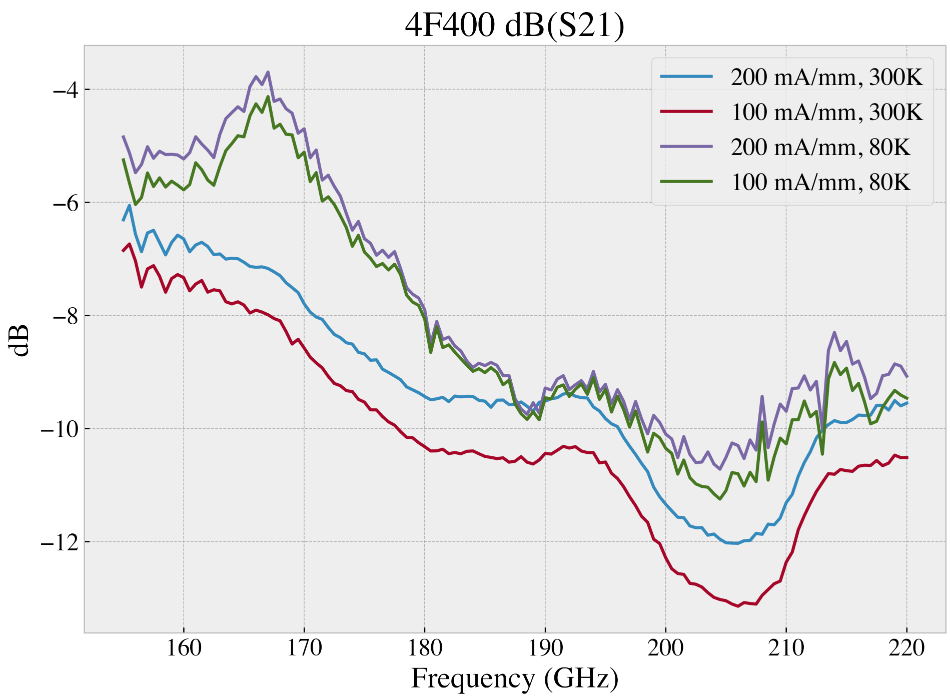

Figure 4.7: Measured power gain of a four-finger 400μm periphery device at room temperature and 80K.

It can be seen from the following figures that the quality of the room-temperature calibration was much better than the cryogenic calibration. This obviously affected the accuracy of the cryogenic measurements. The cryogenic measurements required the use of vacuum pumps that added slight vibrations, which added to the measurement difficulty.

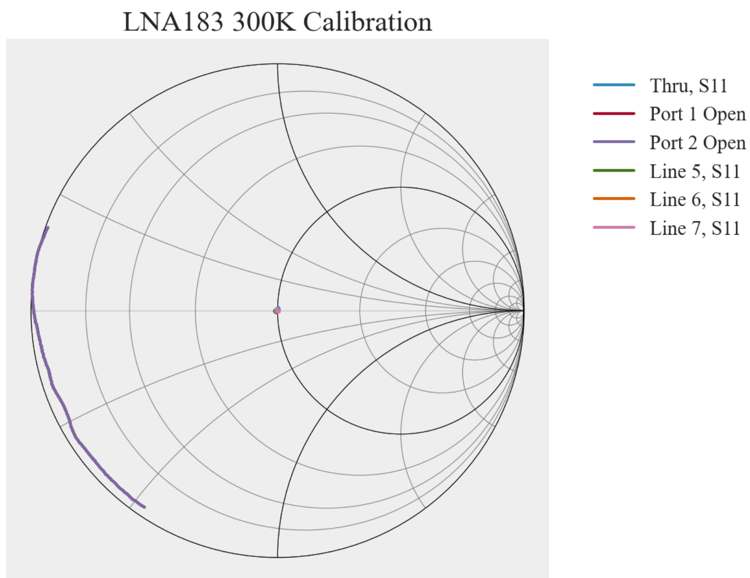

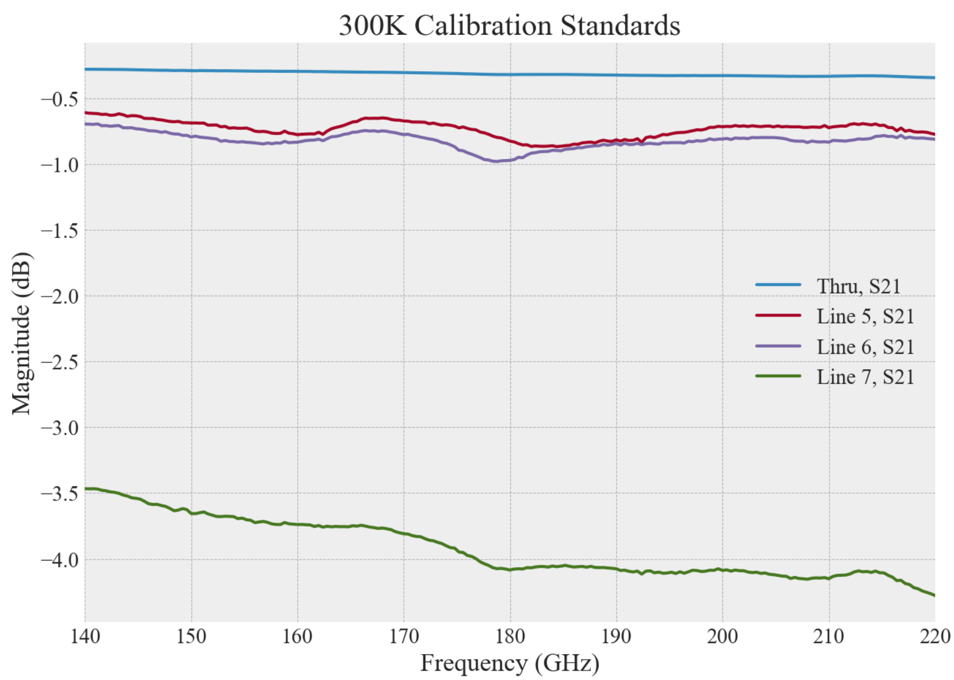

Figure 4.8: Calibration standards for the room-temperature TRL calibration.

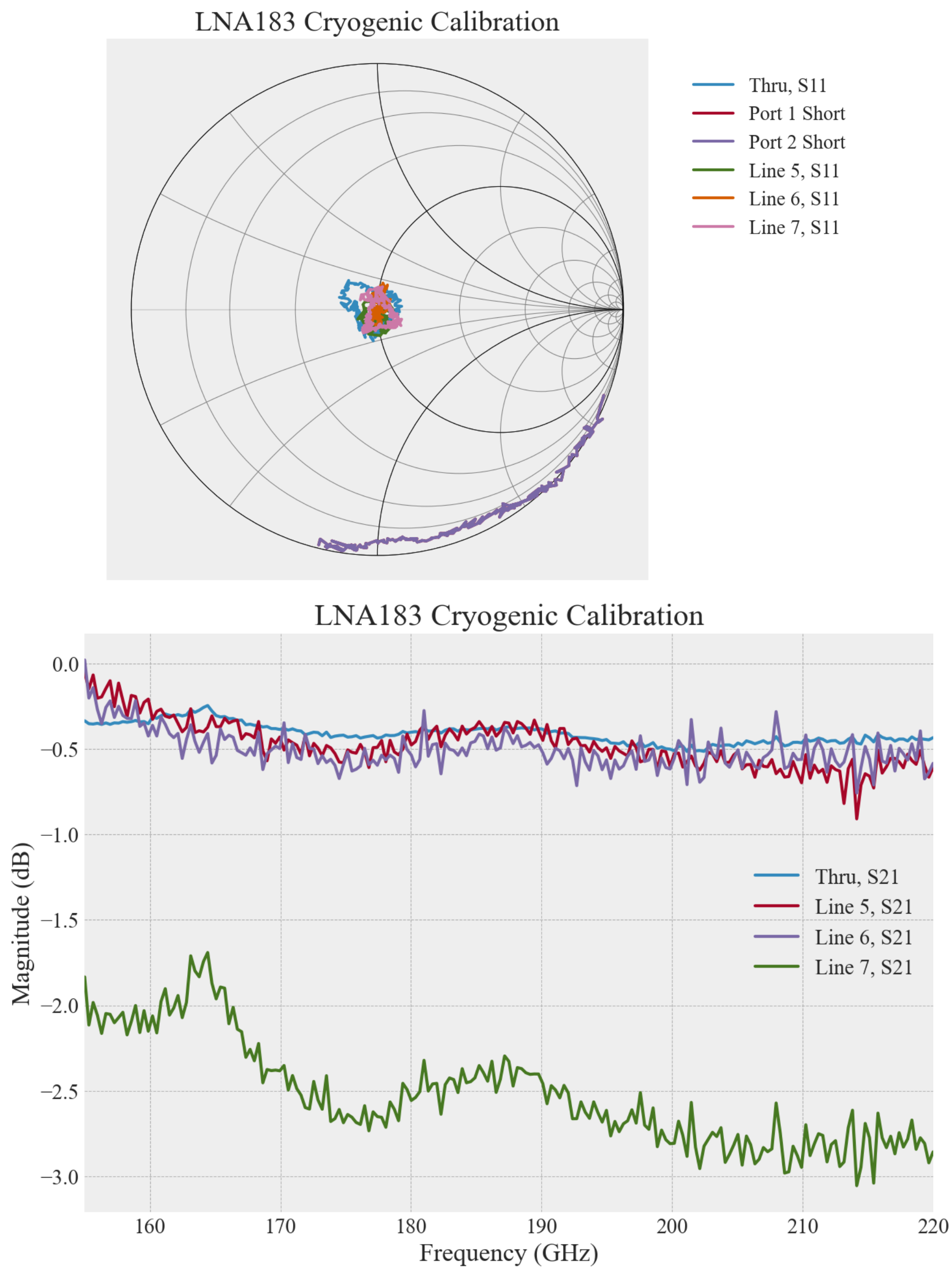

Figure 4.9: Calibration standards for the cryogenic TRL calibration.

4.2. Y-Factor Noise Figure Measurements

The noise figure or noise factor (linear) is a figure of merit that describes the added noise of a particular network. It is defined as the ratio of the signal-to-noise ratio (SNR) at the input and the

SNR at the output.

$$F = \frac{SNR_i}{SNR_o} = \frac{S_i/N_i}{S_o/N_o} \tag{4.1}$$

The output SNR can be rewritten as

$$S_o/N_o = \frac{S_i G}{N_A + N_i G}, \tag{4.2}$$

where G is the network's gain and N_A is the added noise from the network at its output. Therefore,

$$F = \frac{SNR_i}{SNR_o} = 1 + \frac{N_A}{N_i G} \tag{4.3}$$

The Y-factor measurement technique requires a noise source able to output noise of two known power levels or equivalent noise temperatures. By measuring the output noise spectra of the network with two different input noise temperatures, the added noise due to the device can be extracted. This also requires a calibration measurement of the measurement system.

The Y-factor method is summarized in the following equations:

$$F = ENR_{dB} - 10 \log (Y - 1) \tag{4.4}$$

where ENR_{dB} is the excess noise ratio of the noise source and Y is the Y-factor.

$$Y = \frac{P_{hot}}{P_{cold}} \tag{4.5}$$

P_{hot} and P_{cold} are the measured noise powers with the noise source on and off respectively.

4.2.1. Experimental Setup

A block diagram for the RF portion of the Y-factor experimental setup is shown in fig. 4.10. The probe station components together with the device form a noise figure cascade. To calculate the gain and noise figure from the device alone, the noise figures and loss measurements must be known for the other elements.

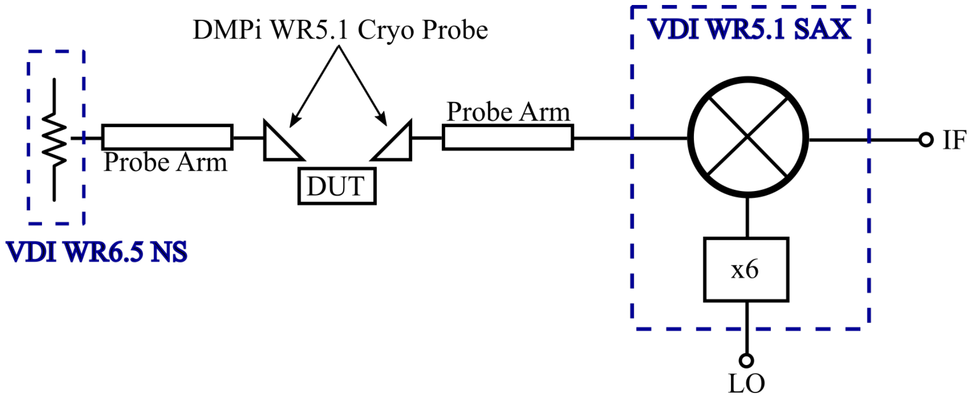

Figure 4.10: Schematic showing the RF setup for the Y-factor noise figure measurements.

The elements in this chain can be measured via the following procedure:

1. Measure the system noise figure:
    - Remove the on-wafer probes.
    - Attach the noise source directly to the second probe arm.
    - Measure the Y-factor noise figure.
2. Measure the first probe arm:
    - Attach the noise source as it is shown in fig. 4.10.
    - Directly connect the waveguide probe arms.
    - Measure the Y-factor noise figure.
3. Measure the probes:
    - Attach the on-wafer probes.
    - Land the probes on a known thru.
    - Measure the Y-factor noise figure.

Assuming that the probe-thru-probe network is reciprocal, the loss and noise figure contributions can be halved. The two half-networks are then placed on either side of the device to mathematically correct for the gain and noise figure of the device alone. This full mathematical cascade is shown in fig. 4.11.

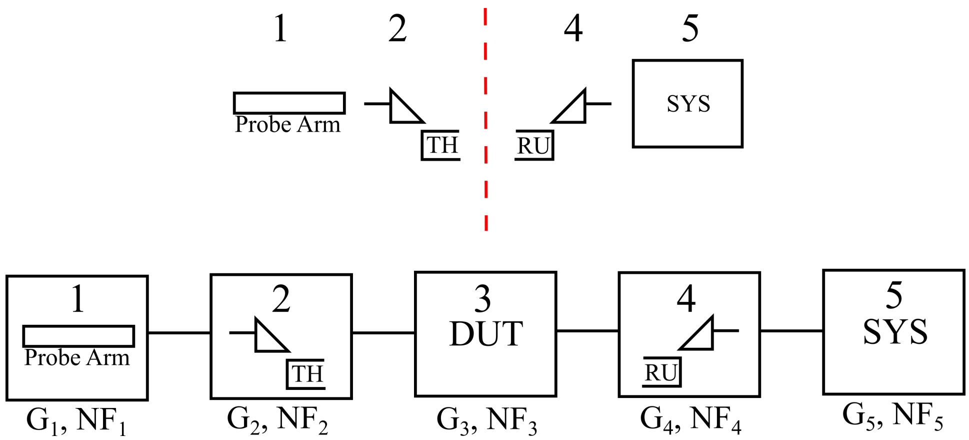

Figure 4.11: Block diagram showing the components in the full noise figure cascade.

The Friis formula for noise [10] is used to perform this calculation:

$$F_{tot} = F_1 + \frac{F_2 - 1}{G_1} + \frac{F_3 - 1}{G_1 G_2} + \cdots + \frac{F_i - 1}{G_1 G_2 \cdots G_{i-1}}, \tag{4.6}$$

where F_3 and G_3 are the noise figure and gain of the DUT. As is common with high-frequency noise measurements, the noise power levels of the DUT and the noise source are much smaller than the system noise floor. The VDI-WR5.1 SAX module has a DANL of -150 dBm/Hz and a conversion loss of about 10 dB. The noise source has an excess noise ratio (ENR) of around 9 dB, and the probe arms have around 3dB of loss. For the measurement of the 10dB attenuator shown in fig. 4.14 and 4.27, the noise power from the noise source (on) is estimated to be about 40 dB below the output noise level of the SAX mixer. For this reason, the IF measurement chain requires the use of a lock-in amplifier (LIA), which is a low-frequency phase-sensitive detector. Two IF measurement chains were assembled for these measurements: one double-sideband system and one single-sideband system.

Both IF systems use a lock-in amplifier as the core measurement tool. Above W-band, noise figure measurement systems often use a quasi-optical approach to inject thermal noise of two different temperatures [**?**]. In this setup, the noise source is 'chopped' optically and the lock-in amplifier locks to the chopper reference. This works very well for measuring packaged receiver noise figures; however, for cryogenic on-wafer measurements, optically injecting noise is extremely difficult. Injecting the noise optically requires the use of antennas or feedhorns with precise alignment. The motion required for on-wafer measurements makes optical injection unrealistic.

A VDI solid-state noise source was used for these measurements. Due to availability, a WR6.5 noise source was used for these measurements. This limited the measurement range to the overlap between WR5.1 and WR6.5: 140 - 170 GHz. The packaged noise source allowed for a direct waveguide connection to the probe arm, which simplified the setup considerably. Another distinct change in this measurement system was the phase-sensitive detection. Normally the noise source DC bias would be modulated with a low-frequency square wave (solid-state equivalent of the optical chopping). The modulation signal is locked-to with the LIA. After power detection, the LIA will output $|P_{hot} - P_{cold}|$; however, to calculate the Y-factor, the individual values of P_{hot} and P_{cold} must be known. This requires the addition of a DC voltmeter to measure the absolute power response of the power detector. In the many configurations of this noise measurement system, the author was unable to get sufficient accuracy from the DC voltmeter reading to obtain an accurate noise figure measurement result.

To eliminate the need for the voltmeter, an RF switch was added before the power detector. In this configuration, the IF chain and a signal generator reference tone is switched at the lock-in modulation frequency. By changing the power of the reference tone, the reading from the lock-in , R, is minimized with the noise source off. The dynamic reserve of the lock-in was more than capable of detecting the power change with the noise source on. The signal generator has fine control over the power level of the reference tone, so the absolute power level is accurately determined in this manner. A 1 second time-constant and 30 second scans at 8 Hz were used for each measurement. One frequency point for the single-sideband measurement took about four minutes.

Double Sideband Measurements

The double sideband IF system is more simple than the single sideband IF system. It consists of two LNAs and bandpass filters. The filters set the measurement frequency and bandwidth. The full chain is shown in fig. 4.12.

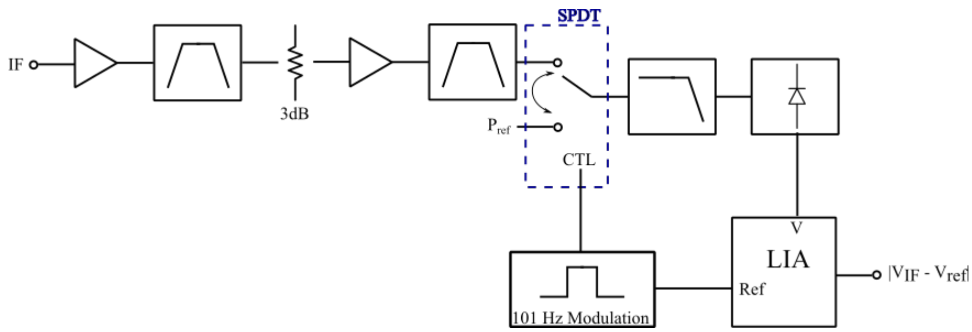

Figure 4.12: IF chain for the double sideband noise measurements.

The power detector was an Herotek DHMA18AB. The RF switch was a Skyworks SKY13286-359LF-EVB. The bandpass filters were Mini-Circuits VBF-2275+. The LNAs were custom balanced Mini-Circuits PMA3-63GLN+. Some specifications for the double sideband system in summarized in Table 4.1. A picture of the IF system and the mounted SAX unit is in Fig. 4.13.

Table 4.1: DSB IF System

Parameter	**Value**
f_c	2275 MHz
Bandwidth	210 MHz
Gain	50 dB
DSB Total Span	4760 MHz

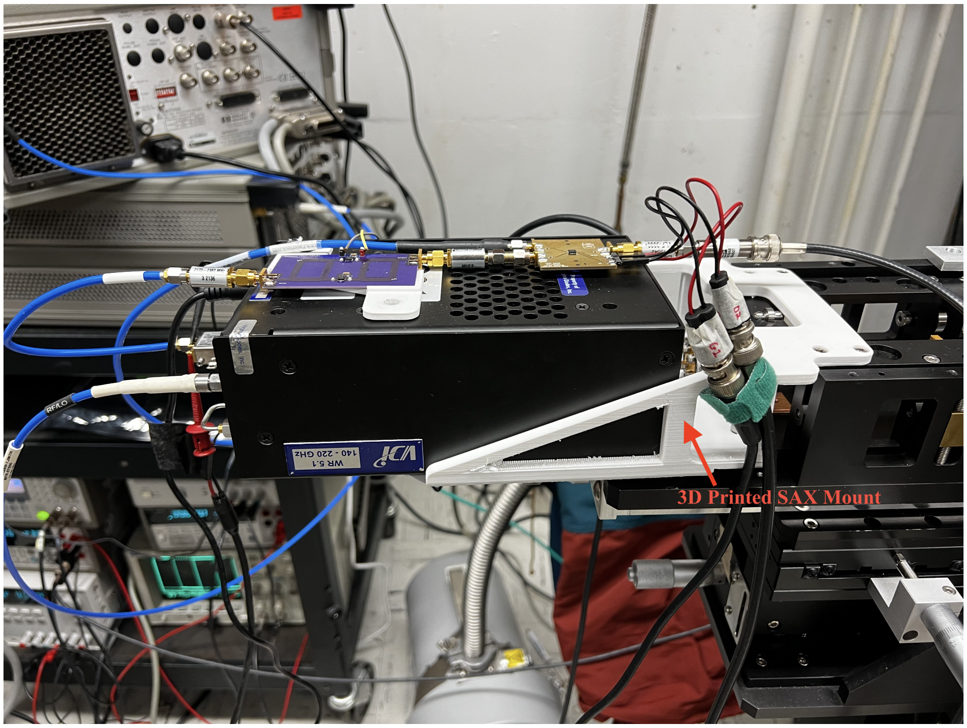

Figure 4.13: Picture showing the custom 3D-printed mount for the large form-factor SAX unit. The IF chain is mounted to the top of the SAX.

A system verification was performed to check the accuracy of the system against a known DUT. Perfectly matched passive networks should have equal noise figure and loss in dB. The verification consisted of measuring the loss and noise figure of one of the probe arms (about 3dB loss) and then a subsequent measurement of a 10 dB WR5.1 attenuator between the two cryoprobe arms. The loss and noise figure were plotted against the power loss from a VNA measurement.

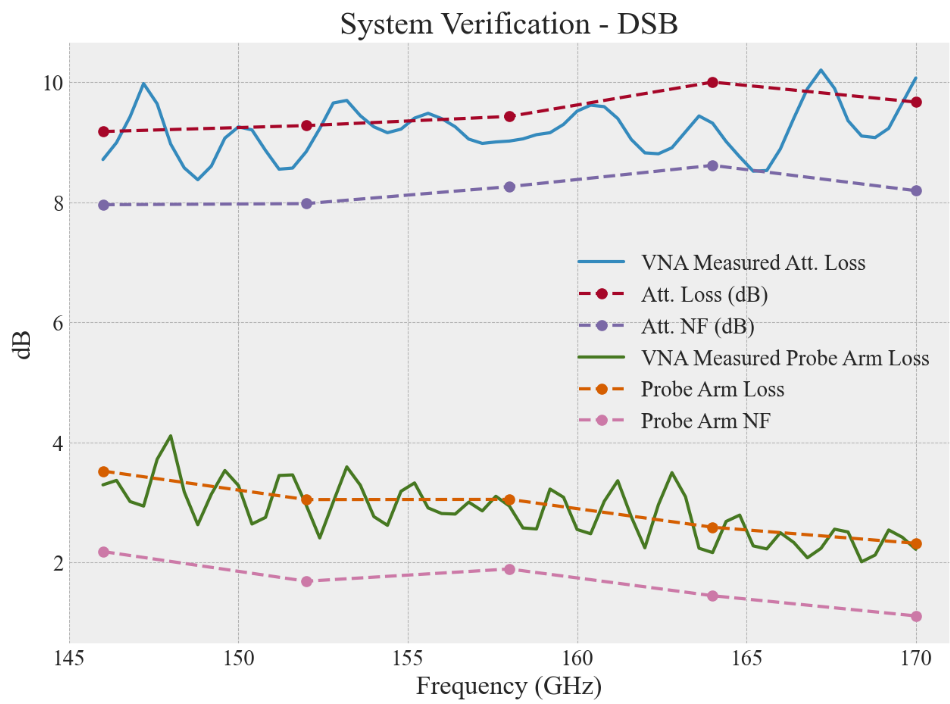

Figure 4.14: A measurement of passives. For a perfectly matched passive network, the loss and noise figure in dB should be equal.

There is some error in the noise figure calculation but is within 1 dB generally.

The noise figure and gain of the NGC LNA183 is plotted for a particular bias point at room temperature and 80K in fig. 4.15. The packaged version of the LNA183 has integrated dipole antennas in place of the CPW probe launcher. It has a NF of about 5 dB. The double sideband data in general has accurate gain measurements; however, the noise figure for the devices is higher than expected. The single-sideband data is more accurate.

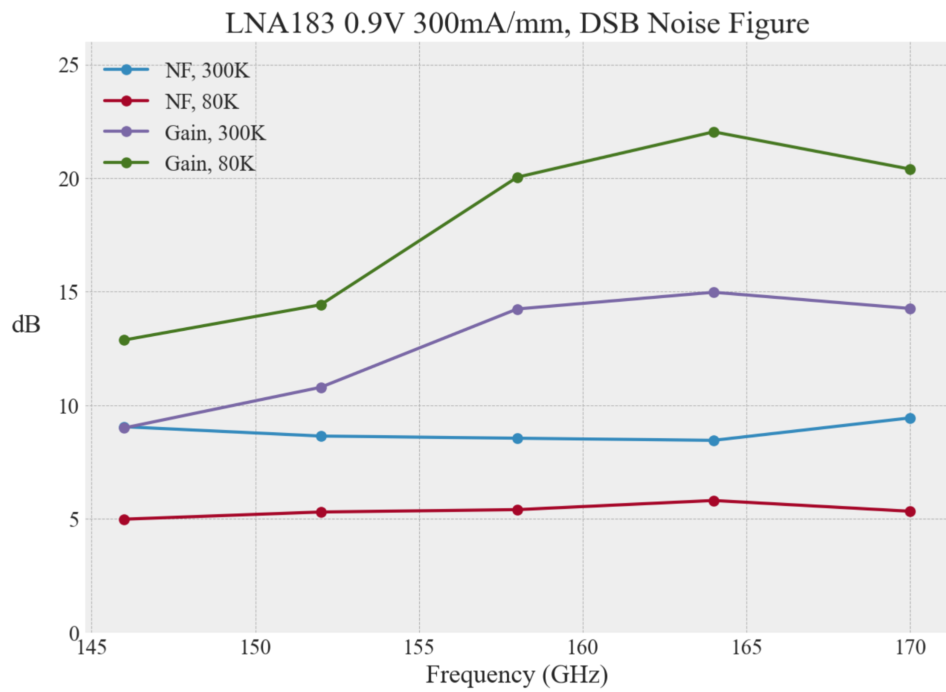

Figure 4.15: Comparison of gain and noise figure for the NGC LNA183 (0.9V, 300mA/mm) at room temperature and 80K.

There is an expected increase in gain and decrease in noise figure with decreasing temperature. This is discussed in depth later. Some selected results for the amplifier measurements are shown in Figures 4.16 and 4.17.

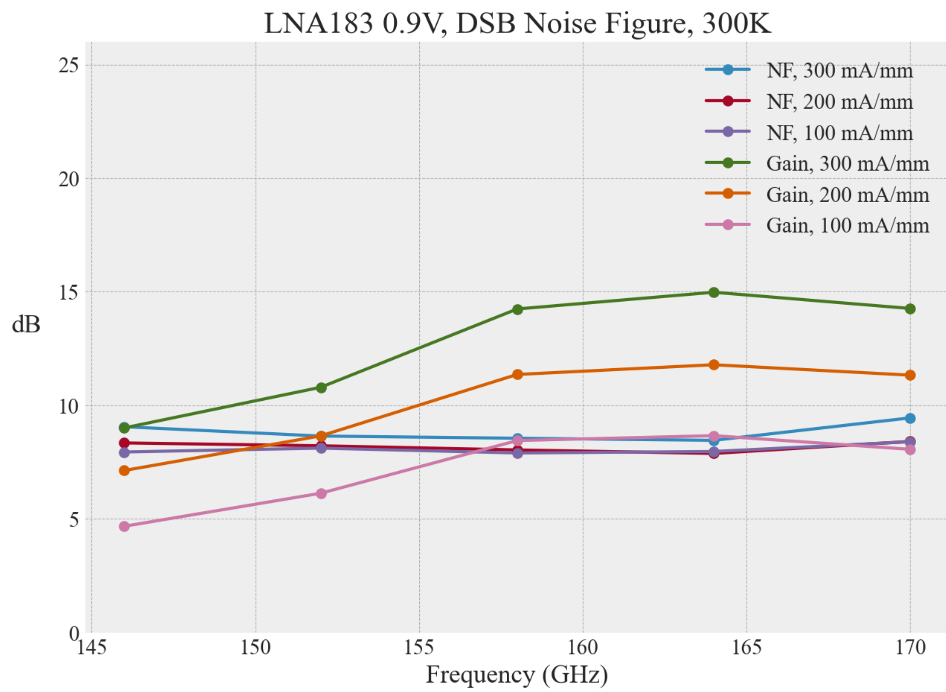

Figure 4.16: Room temperature gain and noise figure results for the NGC LNA183 vs. drain current.

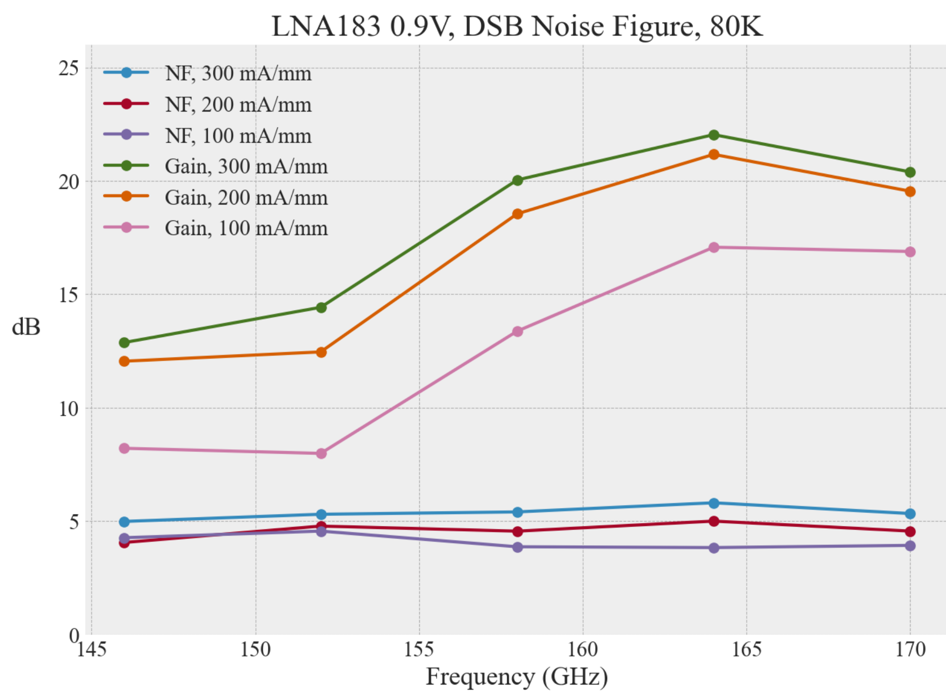

Figure 4.17: Cryogenic gain and noise figure results for the NGC LNA183 vs. drain current.

Similar stability issues with the single devices at cryogenic temperatures was observed. The best results for the two-finger 80μm device and the four-finger 400μm device are shown below. The four-finger 400μm device was very stable at cryogenic temperatures.

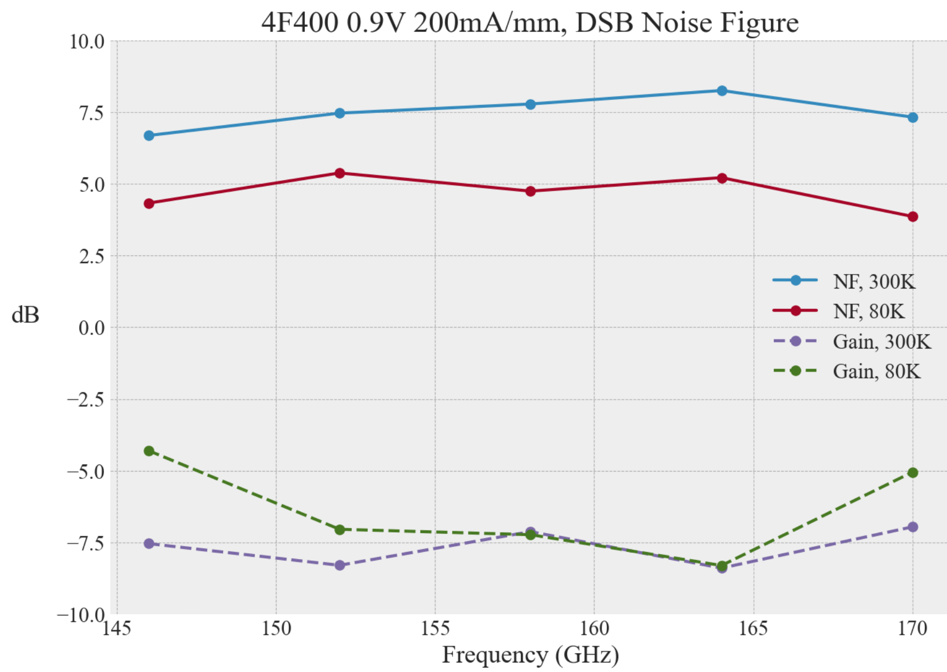

Figure 4.18: Gain and noise figure of the four-finger 400μm device vs. temperature.

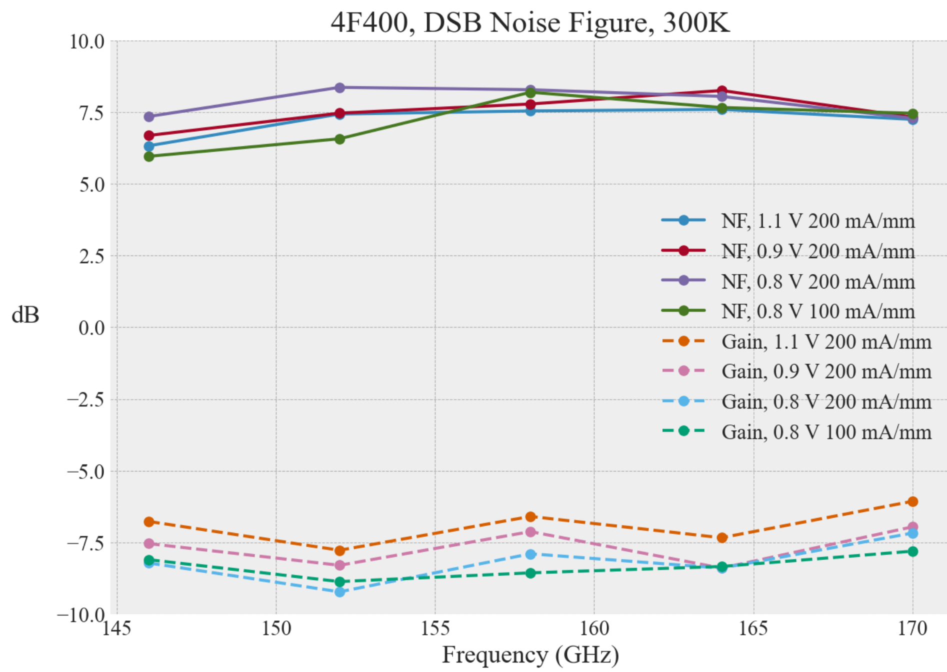

Figure 4.19: Gain and noise figure of the four-finger 400μm at room temperature.

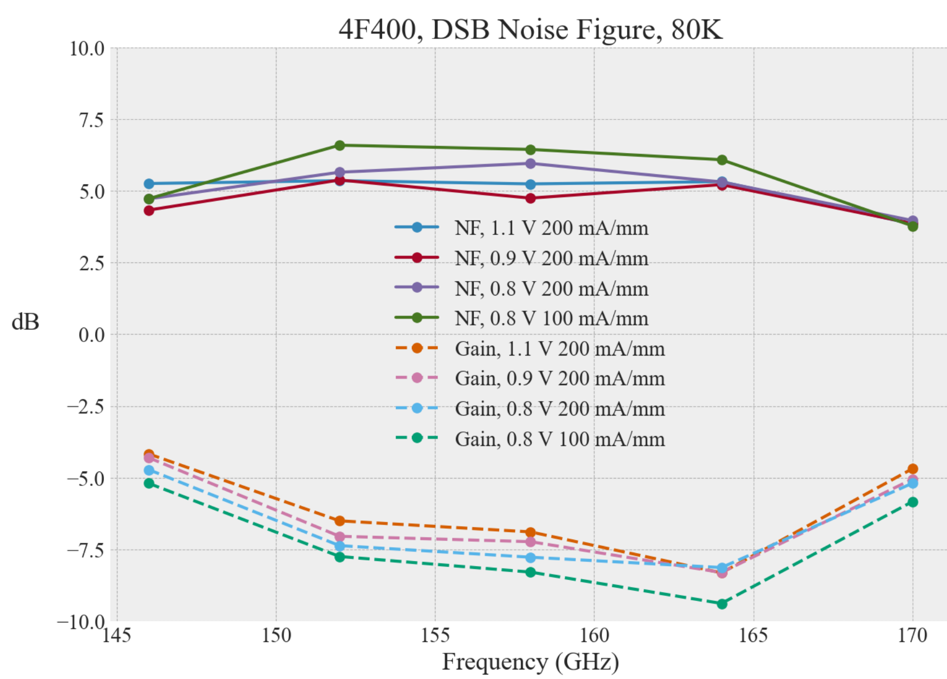

Figure 4.20: Gain and noise figure of the four-finger 400μm at 80K.

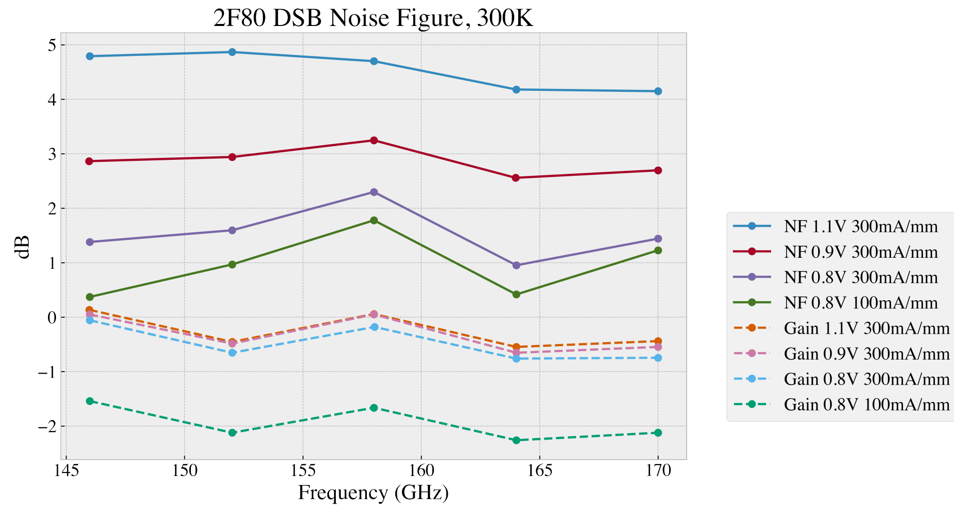

Figure 4.21: Gain and noise figure measurements for the two-finger 80μm device at room temperature vs drain current.

Single Sideband Measurements

Since the VDI SAX unit is essentially a double-sideband down-converting mixer in this configuration, the previous IF chain folded two RF sidebands into the IF measurement bandwidth. This introduced potential measurement error as the gain and noise figure of the devices are heavily frequency dependent. Additionally the provided ENR of the VDI noise source varies up to $\pm$ 1 dB over the measurement frequency range. To remove the unwanted sideband, another IF chain was developed based on [9]. A schematic showing this IF system in shown in fig. 4.22. This IF system has two separate filtering sections controlled by an additional RF switch. The second set of IF filters are centered at twice the frequency of the first. Some specifications for this system are given in Table 4.2.

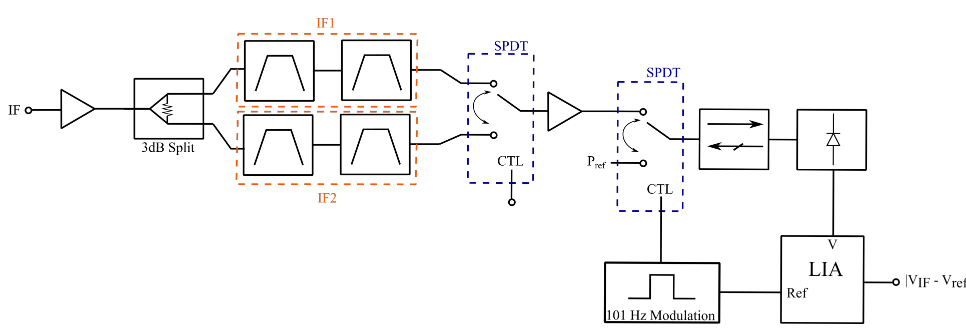

Figure 4.22: IF chain for the double sideband noise measurements.

Table 4.2: SSB IF System

Parameter	Value
IF1 f_c	1100 MHz
IF1 Bandwidth	200 MHz
IF2 f_c	2150 MHz
IF2 Bandwidth	200 MHz

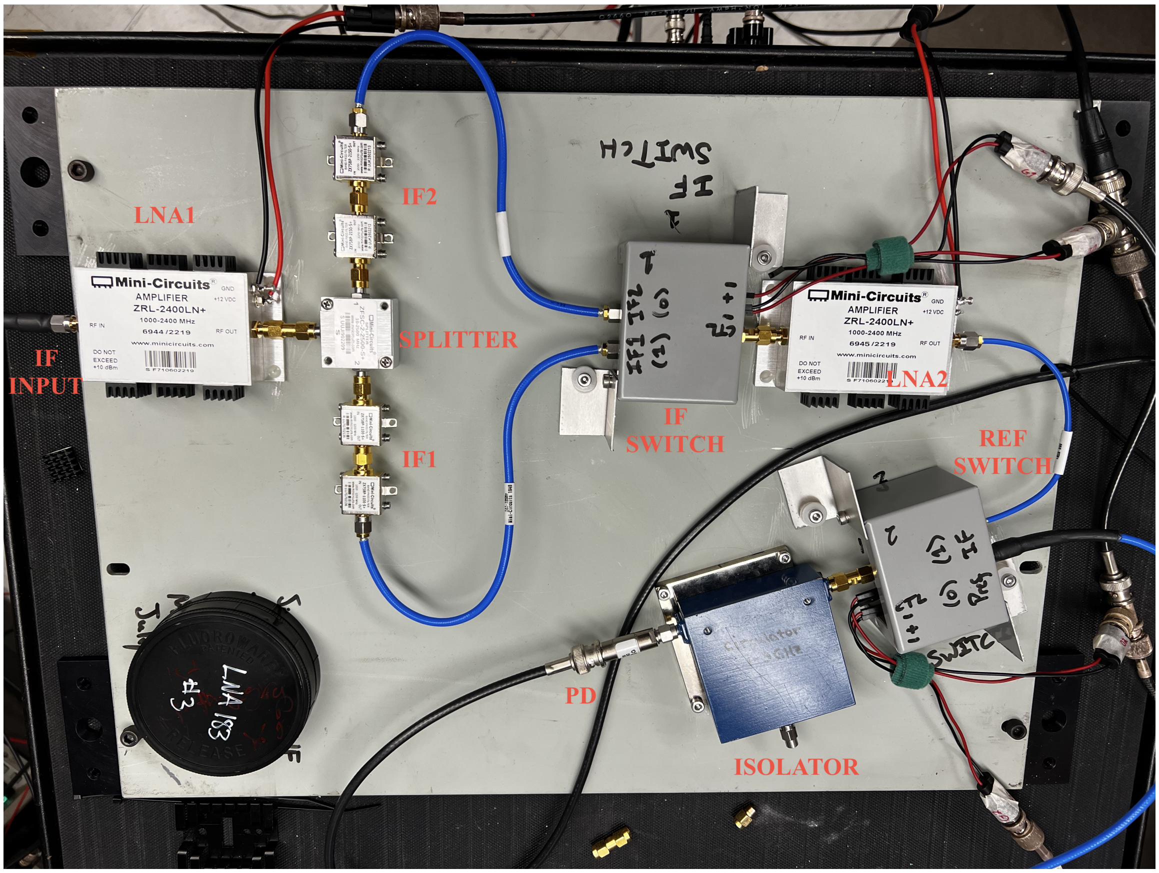

Figure 4.23: Picture of the assembled SSB IF system.

The measurement procedure now requires three measurements per frequency point. The procedure is shown graphically in fig. 4.24. By tuning the LO such that the intended sideband is the lower sideband (spaced by IF1 f_c), an unwanted upper sideband is measured. Similarly by tuning the LO such that the indended sideband is the upper sideband, and unwanted lower sideband is measured. These unwanted sidebands are spaced by 2·IF1; therefore, by tuning the LO to the desired RF frequency and switching to the second set of IF filters, the unwanted sidebands can be measured and subtracted from the other measurements.

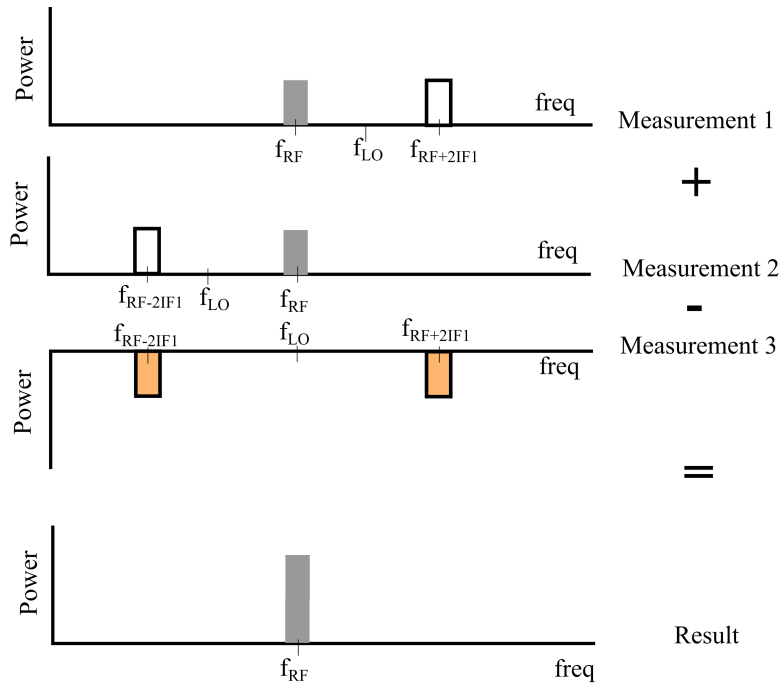

Figure 4.24: Measurement procedure showing the cancellation of unwanted sidebands [9].

Assembling two IF chains with identical bandwidth and gain at two separate frequencies is unrealistic, so a normalization factor was calculated to appropriately scale the power measurements from the second IF chain. This ensures that the power from the unwanted sidebands is subtracted out accurately. The ratio, N, is the ratio of the integrated powers of IF1 and IF2.

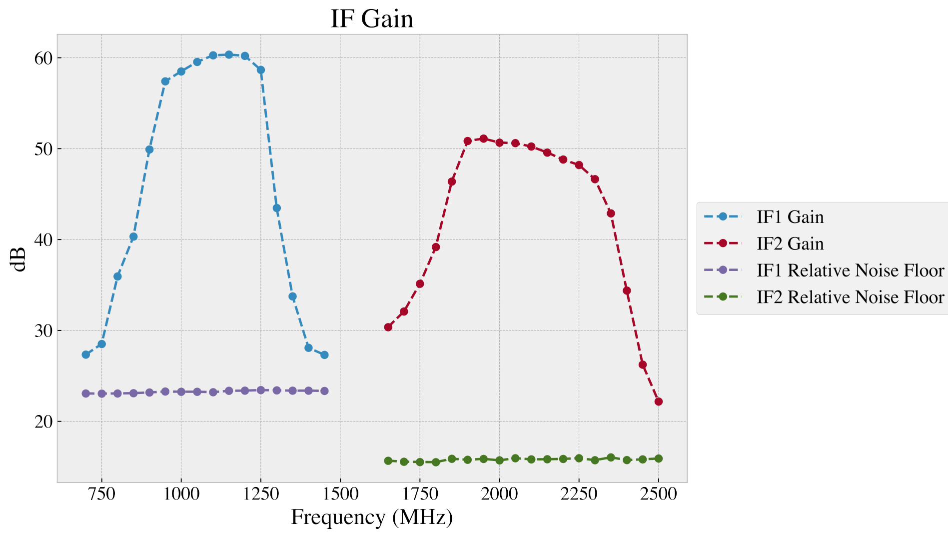

Figure 4.25: Measured gain and relative noise floors of the two IF chains. The normalization factor is the ratio of the integrated power under each curve.

Though unused in the normalization calculation, the isolation between the two chains was measured and is plotted in fig. 4.26.

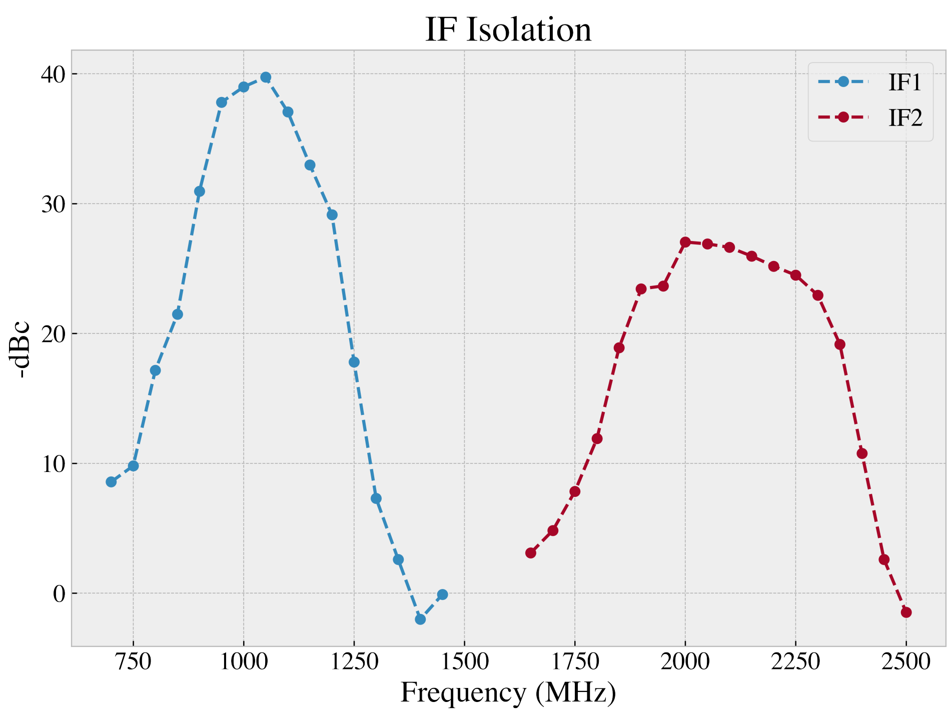

Figure 4.26: The isolation between the two IF bands. This plots the measured power of IF2 frequencies injected into the IF1 system and IF1 frequencies in the IF2 system relative to the power of the injected tone.

The same verification performed for the double sideband system was performed for this system. The agreement between the measured loss and noise figure was much better with this system.

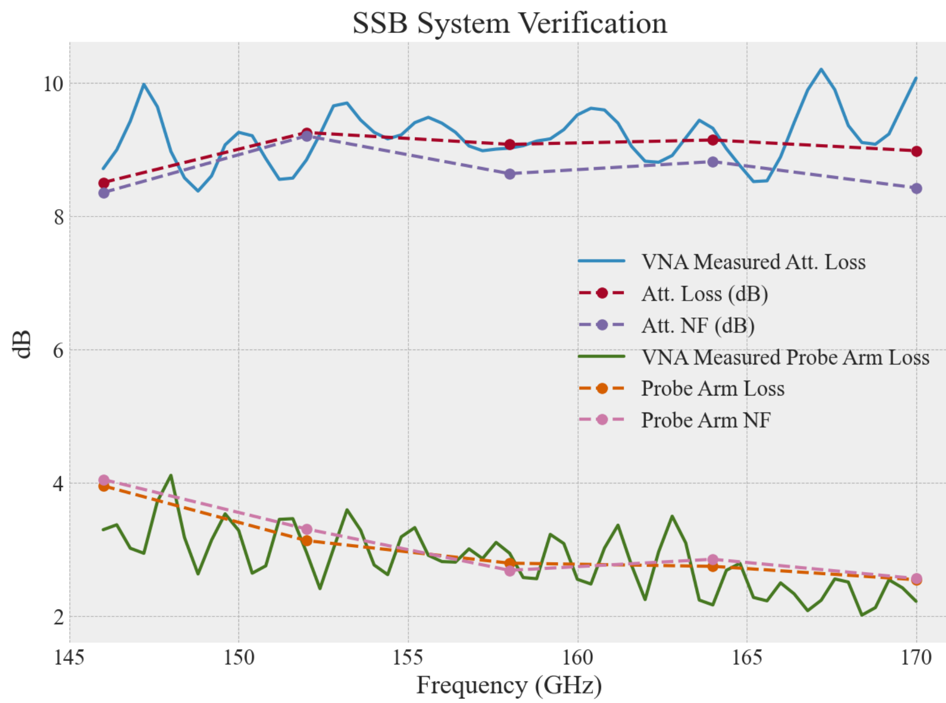

Figure 4.27: A measurement of passive networks to verifiy the accuracy of the noise figure measurement system.

The measured results for the NGC LNA183 (0.8V, 100 mA/mm) is shown in fig. 4.28. Again, there was an expected increase in measured gain and decrease in noise figure with decreasing temperature.

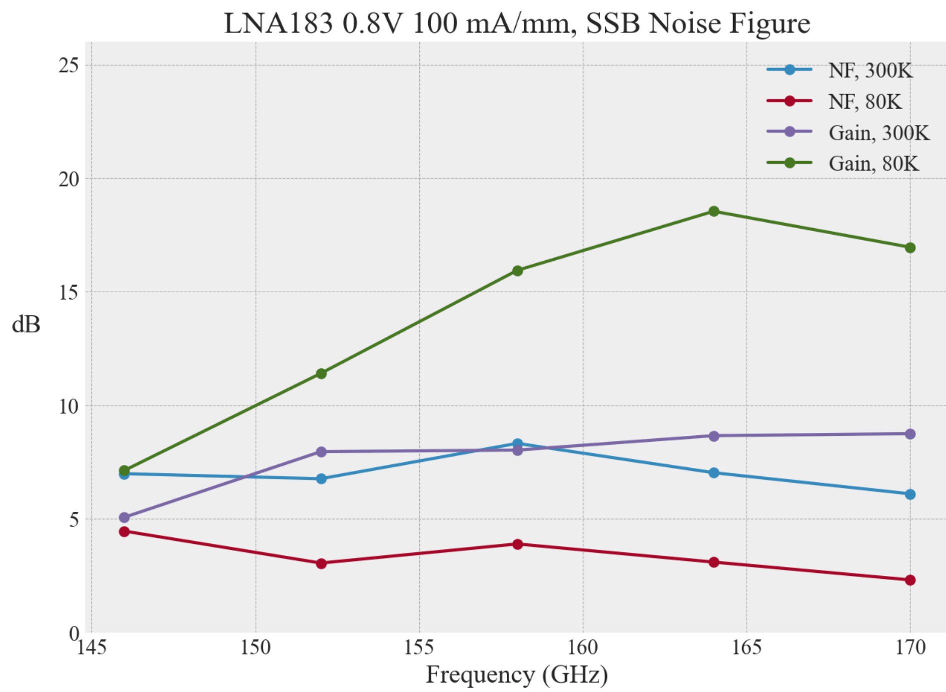

Figure 4.28: Gain and noise figure results for the NGC LNA183.

Selected measurement results from the single sideband measurements are given in fig. 4.29 - 4.32. Figure 4.29 shows the gain and noise figure of the LNA183 vs. drain current at 80K. The packaged LNA183 has about 5 dB noise figure at 170 GHz, 300 K, and 300 mA/mm.

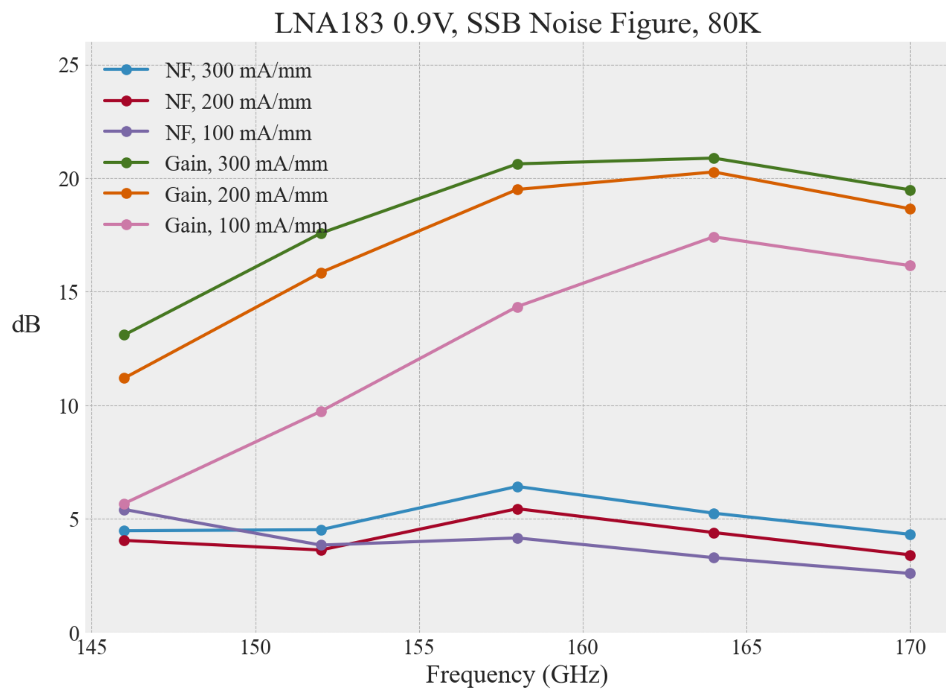

Figure 4.29: Measured gain and noise figure of the NGC LNA183 vs. drain current at 80K.

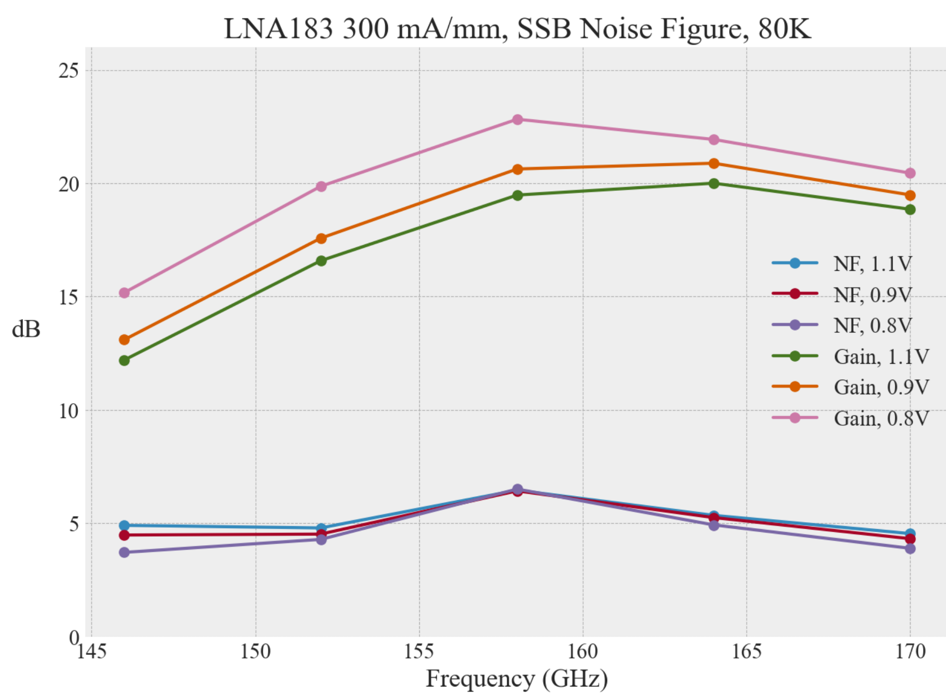

Figure 4.30: Measured gain and noise figure of the NGC LNA183 vs. drain voltage at 80K.

The calculated gain of the LNA183 from the noise figure measurements is plotted against the measured gain from the scattering parameter measurements in fig. 4.31. The noise figure measurement frequency was limited by the noise source (VDI WR6.5), and the low end of the s-parameter measurements were due to hardware as well. VDI was extremely kind and quickly built a set of these extenders for this experiment, for which this author is extremely grateful. However, the low end (140 - 155 GHz) did not work well. The data in fig. 4.31 looks reasonable and is in close agreement.

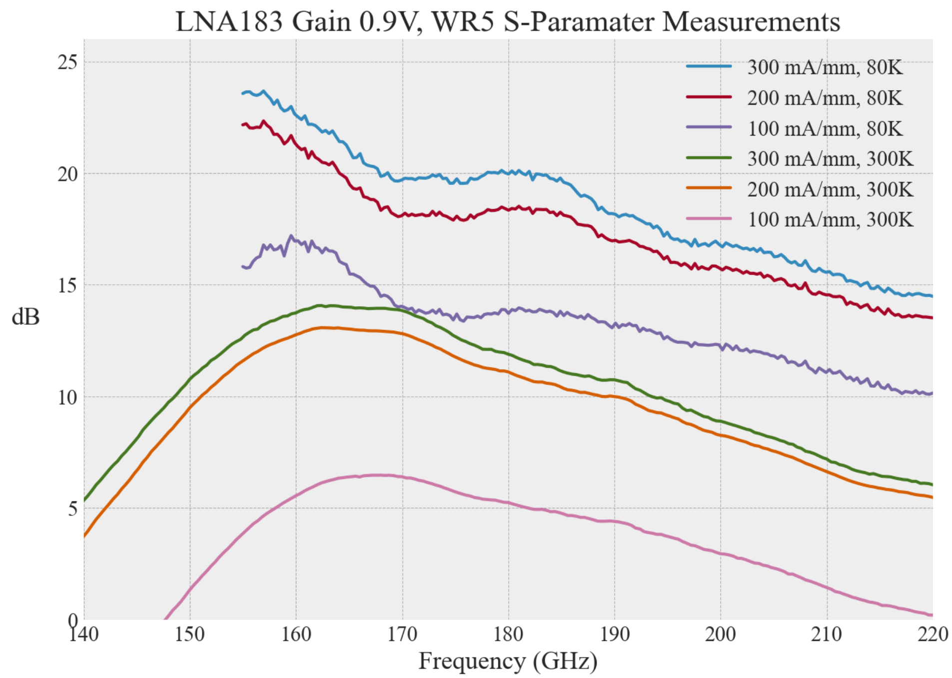

Figure 4.31: A comparison of the cryogenically measured gain from noise figure measurement and s-parameter measurement.

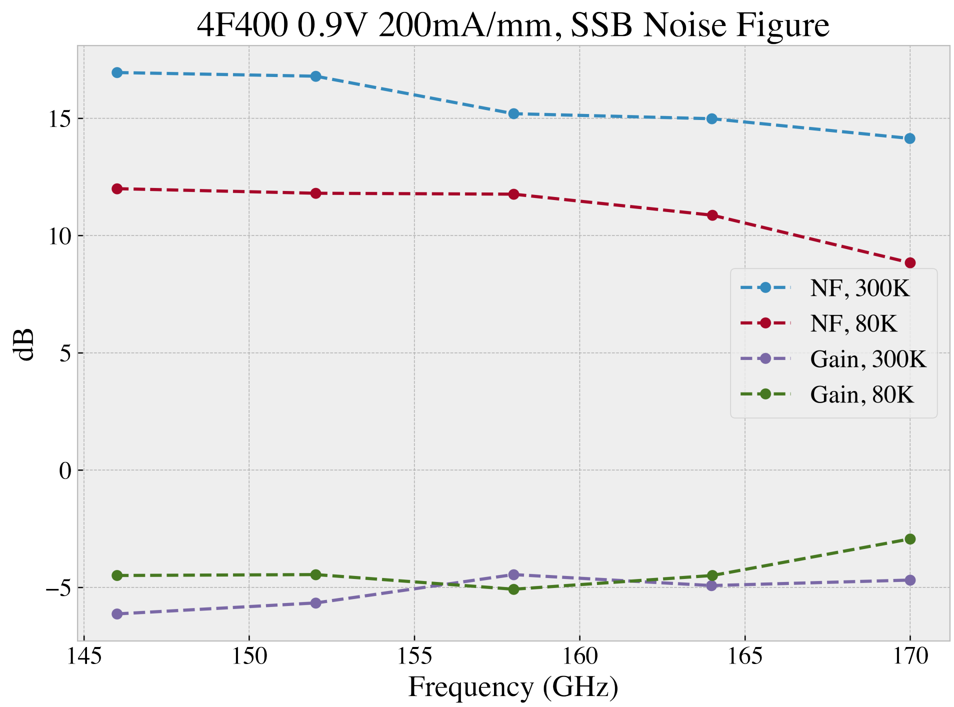

Figure 4.32: Noise figure and gain of the four-finger 400μm device at room temperature and 80K.

The figure below shows the measured noise figure and gain for the two-finger 80μm device. Additionally, the equivalent noise temperature is plotted with the small-signal model's noise temperature. The small-signal model was developed using the extractions shown in Chapter 3, and the drain resistor noise temperature from the NGC model was applied. This noise temperature was assigned using the Pospieszalski method and noise parameter measurements. The downward trend in noise figure and noise temperature is unexpected, the measured noise temperature is on the order of the modeled noise temperature.

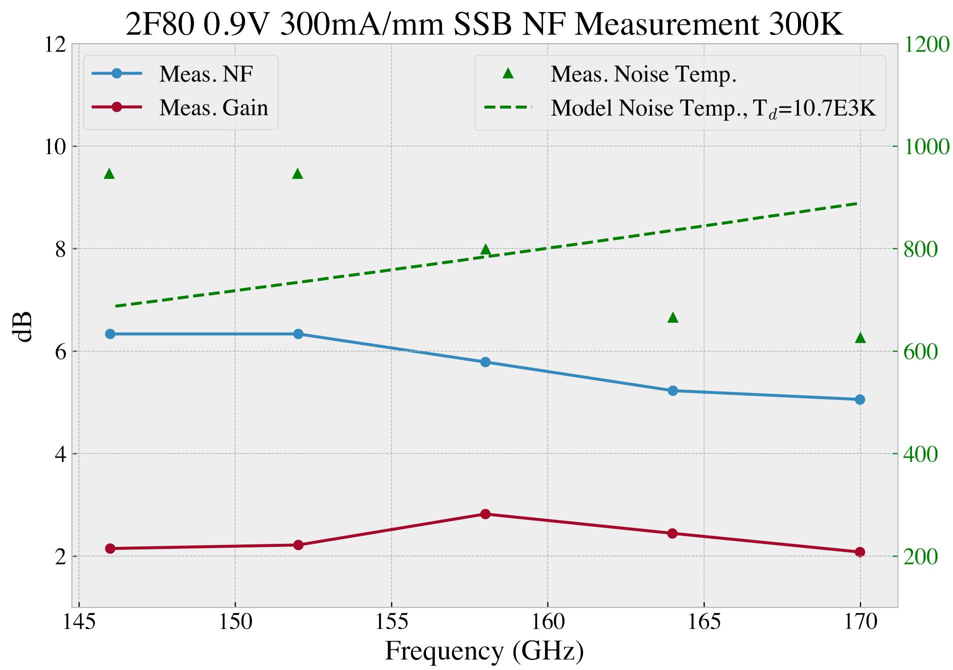

Figure 4.33: Measured gain and noise figure of the two-finger 80μm device at 300K. Additionally the noise equivalent temperature is plotted against the unmodified NGC noise model (right y-axis).

4.2.2. Discussion

The single-sideband IF chain performed better than the double-sideband system for a few reasons. The measurement error from an unaccounted sideband was removed but also the double-sideband system was more vulnerable to EMI. The single-sideband system used fully shielded componenets whereas the LNAs in the double sideband-system used un-shielded PCBs and had a center frequency (2.275 GHz) near WiFi (2.4GHz). The effects from networked devices in close proximity to the measurement chain was noticeable in random fluctuations in the LIA reading. The negative of the single-sideband system is primarily in acquisition time. The sideband cancellation requires three measurements for each frequency point, and low-level noise measurements such as this require long time constants and averaging.

The measurements would be improved with a well-characterized, well-matched LNA directly after the noise source. This would significantly improve the effective ENR of the noise source. Another improvement for the single-sideband system would be another RF switch instead of the initial 3 dB splitter. This would not only remove the 3 dB of loss but also the isolation between the two IF chains.

Modeling of Temperature Dependence

At cryogenic temperatures, several physical parameters change in these devices. Temperature-dependent parameter extractions of HEMTs and modeling at lower frequencies has been an area of interest for many decades now[11] - [17]. With decreasing temperature the resistances of metal contacts will decrease slightly. The substrate leakage will dramatically decrease as any thermally excited carriers in the substrate will fall energetically into the valence band. The permeability and permittivity of the substrate will not change significantly (however dielectric absorption and loss tangent will decrease), so the inductances and bias-independent capacitances will not change [18], [19].

Decreasing temperature will positively shift the threshold voltage, so C_{gd} and C_{gs} are temperature dependent. The most important change is an increase in electron mobility, which means a higher saturation velocity and higher transconductance as a result [20]. The increase in gain at lower temperature is a result of this phenomenon.

A rough temperature-dependent model was developed with the data reported in this chapter. Simple temperature scaling factors were applied to all resistance values and a cryogenic drain resistor noise temperature was extracted. The room-temperature model had a drain temperature of 11.73e3 K and the cryogenic model had a drain temperature of 5.27e3 K. The drain noise temperature did not scale with the ambient temperature as the gate equivalent temperature did, which agrees with the Pospieszalski model [21]. The noise in the drain includes thermal noise and current shot noise. This current shot noise does not scale with ambient temperature like thermal noise. The plotted noise figures of the model are shown below.

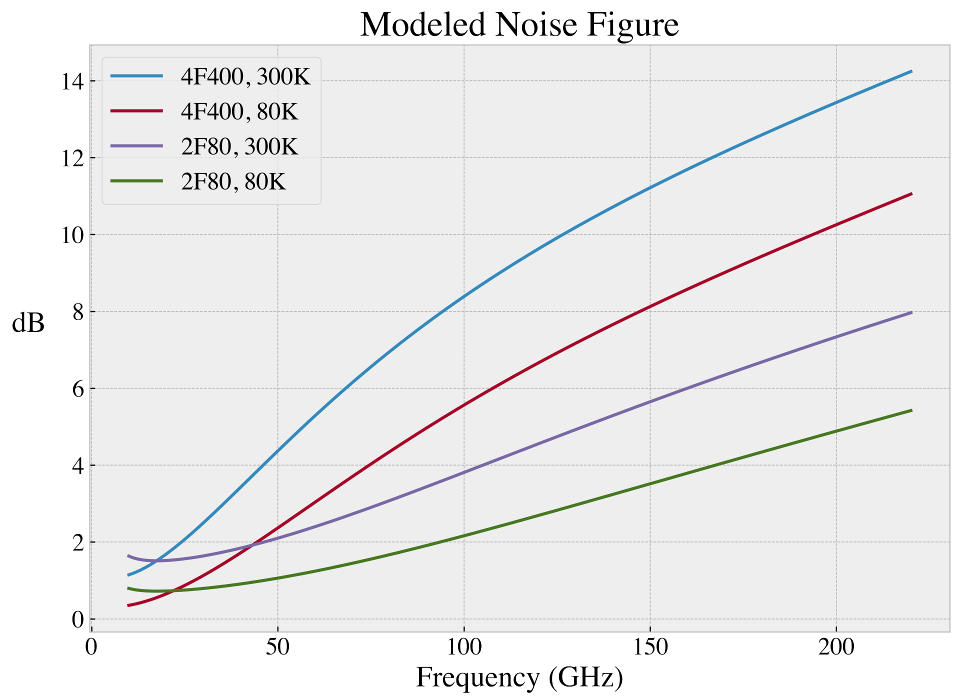

Figure 4.34: Noise figure of temperature-dependent model. Generated using simple temperature scaling rules and drain temperature extraction from noise figure measurements.

Bibliography

[1] J. Laskar, J. J. Bautista, M. Nishimoto, M. Hamai, and R. Lai, “Development of accurate on-wafer, cryogenic characterization techniques,” IEEE Trans. Microw. Theory Tech., vol. 44, no. 7, pp. 1178–1183, Jul. 1996, doi: 10.1109/22.508659.

[2] H. Meschede et al., “On-wafer microwave measurement setup for investigations on HEMTs and high-T/sub c/ superconductors at cryogenic temperatures down to 20 K,” IEEE Trans. Microw. Theory Tech., vol. 40, no. 12, pp. 2325–2331, Dec. 1992, doi: 10.1109/22.179897.

[3] M. R. Murti et al., “Temperature-dependent small-signal and noise parameter measurements and modeling on InP HEMTs,” IEEE Trans. Microw. Theory Tech., vol. 48, no. 12, pp. 2579–2587, Dec. 2000, doi: 10.1109/22.899016.

[4] T. Vaha-Heikkila, M. Lahdes, M. Kantanen, and J. Tuovinen, “On-wafer noise-parameter measurements at W-band,” IEEE Trans. Microw. Theory Tech., vol. 51, no. 6, pp. 1621–1628, Jun. 2003, doi: 10.1109/TMTT.2003.812554.

[5] R. Hu and S. Weinreb, “A novel wide-band noise-parameter measurement method and its cryogenic application,” IEEE Trans. Microw. Theory Tech., vol. 52, no. 5, pp. 1498–1507, May 2004, doi: 10.1109/TMTT.2004.827029.

[6] T. Vaha-Heikkila, J. Varis, H. Hakojarvi, and J. Tuovinen, “Wideband cryogenic on-wafer measurements at 20-295 K and 50-110 GHz,” in 33rd European Microwave Conference Proceedings (IEEE Cat. No.03EX723C), Oct. 2003, vol. 3, pp. 1167-1170 Vol.3. doi: 10.1109/EUMC.2003.177692.

[7] D. R. Daughton et al., "Cryogenic temperature, 2-port, on-wafer characterization at WR-5.1 frequencies," 2016 IEEE MTT-S International Microwave Symposium (IMS), 2016, pp. 1-4, doi: 10.1109/MWSYM.2016.7540118.

[8] E. Cha et al., "Two-Finger InP HEMT Design for Stable Cryogenic Operation of Ultra-Low-

Noise Ka- and Q-Band LNAs," in IEEE Transactions on Microwave Theory and Techniques, vol. 65, no. 12, pp. 5171-5180, Dec. 2017, doi: 10.1109/TMTT.2017.2765318.

[9] C. E. Collins, R. D. Pollard, R. E. Miles and R. G. Dildine, "On the measurement of SSB noise figure using sideband cancellation," in IEEE Transactions on Instrumentation and Measurement, vol. 45, no. 3, pp. 721-727, June 1996, doi: 10.1109/19.494588.

[10] H. T. Friis, "Noise Figures of Radio Receivers," in Proceedings of the IRE, vol. 32, no. 7, pp. 419-422, July 1944, doi: 10.1109/JRPROC.1944.232049.

[11] J. Schleeh, H. Rodilla, N. Wadefalk, P. -Å. Nilsson and J. Grahn, "Characterization and Modeling of Cryogenic Ultralow-Noise InP HEMTs," in IEEE Transactions on Electron Devices, vol. 60, no. 1, pp. 206-212, Jan. 2013, doi: 10.1109/TED.2012.2227485.

[12] A. Caddemi, G. Crupi and N. Donato, "Microwave characterization and modeling of packaged HEMTs by a direct extraction procedure down to 30 K," in IEEE Transactions on Instrumentation and Measurement, vol. 55, no. 2, pp. 465-470, April 2006, doi: 10.1109/TIM.2006.864248.

[13] M. W. Pospieszalski, S. Weinreb, R. D. Norrod and R. Harris, "FETs and HEMTs at cryogenic temperatures-their properties and use in low-noise amplifiers," in IEEE Transactions on Microwave Theory and Techniques, vol. 36, no. 3, pp. 552-560, March 1988, doi: 10.1109/22.3548.

[14] M. R. Murti et al., "Temperature-dependent small-signal and noise parameter measurements and modeling on InP HEMTs," in IEEE Transactions on Microwave Theory and Techniques, vol. 48, no. 12, pp. 2579-2587, Dec. 2000, doi: 10.1109/22.899016.

[15] J. J. Bautista et al., "Cryogenic, X-band and Ka-band InP HEMT based LNAs for the Deep Space Network," 2001 IEEE Aerospace Conference Proceedings (Cat. No.01TH8542), 2001, pp. 2/829-2/842 vol.2, doi: 10.1109/AERO.2001.931264.

[16] M. R. Murti et al., "Temperature-dependent noise parameters and modeling of

InP/InAlAs/InGaAs HEMTs," 2000 IEEE MTT-S International Microwave Symposium Digest (Cat. No.00CH37017), 2000, pp. 1241-1244 vol.2, doi: 10.1109/MWSYM.2000.863584.

[17] A. R. Alt and C. R. Bolognesi, "(InP) HEMT Small-Signal Equivalent-Circuit Extraction as a Function of Temperature," in IEEE Transactions on Microwave Theory and Techniques, vol. 63, no. 9, pp. 2751-2755, Sept. 2015, doi: 10.1109/TMTT.2015.2448539.

[18] K. Zhou, S. Caroopen, Y. Delorme, M. Batrung, M. Gheudin and S. Shi, "Dielectric Constant and Loss Tangent of Silicon at 700–900 GHz at Cryogenic Temperatures," in IEEE Microwave and Wireless Components Letters, vol. 29, no. 7, pp. 501-503, July 2019, doi: 10.1109/LMWC.2019.2920532.

[19] P. Riess and P. Baumgartner, "Temperature Dependent Dielectric Absorption of MIM Capacitors: RF Characterization and Modeling," 2006 European Solid-State Device Research Conference, 2006, pp. 459-462, doi: 10.1109/ESSDER.2006.307737.

[20] Sze, “JFETs, MESFETs, and MODFETs,” in Physics of Semiconductor Devices, pp. 374–413.

[21] M. W. Pospieszalski, “Modeling of noise parameters of MESFETs and MODFETs and their frequency and temperature dependence,” IEEE Trans. Microw. Theory Tech., vol. 37, no. 9, pp. 1340–1350, Sep. 1989, doi: 10.1109/22.32217.